



**FACULDADE DE CIÊNCIAS E TECNOLOGIA**  
**UNIVERSIDADE NOVA DE LISBOA**

DEPARTAMENTO DE FÍSICA

**FUNCTIONAL BRAIN PERFUSION EVALUATION WITH**  
**ARTERIAL SPIN LABELING AT 3 TESLA**

by

Marco André Figueiredo Pimentel

Dissertation submitted in *Faculdade de Ciências e Tecnologia* of  
*Universidade Nova de Lisboa* for the degree of Master of Biomedical  
Engineering

Supervisors: Doctor Pedro Vilela  
Professor Patrícia Figueiredo

**Lisboa**  
**2009**



THIS THESIS IS DEDICATED TO MY GRANDPARENTS

MARIA AND MANUEL FIGUEIREDO AND

CRISTIANA AND GILBERTO PIMENTEL



## Acknowledgements

This work has been done in FCT and in the Imaging Department of *Hospital da Luz* and, besides the long list of people, I would like to thank all of them for their help. The order is not important, only the presence really matters.

Sincere thanks are expressed to my supervisor Doctor Pedro Vilela, who has proposed this fascinating theme. Your regular and prompt feedback, enthusiasm and guidance have been professional and your support for my endeavors over the period of this study has been much appreciated. Thanks also to my other supervisor, Professor Patrícia Figueiredo, without whose knowledge, guidance, assistance, advice and suggestions, this study would not have been successful. It was a privilege working with you both.

I also gratefully acknowledge the assistance of Inês Sousa in the early, middle and final stages of this study. Thanks for all your support, encouragement, patience and teachings. I really enjoyed our regular reunions, our fine conversations and your good advice. Your participation had a great importance for this study.

I acknowledge the whole technical staff of the Imaging Department of *Hospital da Luz* and all volunteers for your collaboration and availability since the very beginning of this study until its conclusion. Namely, I wish to express my gratitude to Rúben, Cristina, Fernando and Cidália, who made this work possible by providing the essential assistance for the examinations. I really appreciate your patience to perform all scans, including the pilot scans, the (long) hours at night even in the weekends that you spent and dedicated to this project and the good conversations that we had. Thanks for making the time that I spent in *Hospital da Luz* a very enjoyable one.

I also wish to thank Professor Mário Secca, who has always expressed interest in this work, and has provided the support and guidance in the early stages. Thank you for your advice, suggestions and for our valuable conversations.

One other special thanks goes to Henrique, whose teachings and suggestions had a relevant part for the development of this work.

To all my friends and colleagues in FCT, thanks for your moral support and encouragement, not only during this work, but also during these five short years. Thank you Nídia, Miguel, João, Patrícia, Milton, Cátia, Hugo, Rui and Cláudio. Special thanks go to Ana, Miguel and Joana, who have encouraged me and provided fine moments with good conversations and discussions during lunches and snacks at FCT and FCUL. Thanks for your friendship; I could always count with you during these five years. Also, I would like to thank my colleagues from the Biomedical Engineering laboratory, Mariana, Iolanda, Patrão, and Sara, for your company, for our many talks and discussions, for the

long nights and weekends that we spent working together in our tasks, for the coffee-breaks, and, in general, for making the past eight months very pleasant.

I also appreciate all the support given by my parents, brother and future sister in law that in different ways made this work possible. I know that I can always count with you anywhere, for everything.

And finally, I really don't know what to say to you. A simple "thanks" seems to be too little to demonstrate all my gratitude for all your support. Maybe a big "THANKS" is better. THANKS for your company, friendship, encouragement, help, advice and talks. THANKS for the fine moments that you provided me during these last months. THANKS for everything!

To all of you that made this work possible, **THANK YOU!**

Lisbon, October 2009

Marco André Figueiredo Pimentel

## Abstract

**Title:** Functional brain perfusion evaluation with Arterial Spin Labeling at 3 Tesla

**Background:** The new clinically available arterial spin labelling (ASL) sequences present some advantages relatively to the commonly used blood oxygenation level dependent (BOLD) method for functional brain studies using magnetic resonance imaging (MRI), namely the fact of being potentially quantitative and more reproducible.

**Purpose:** The main aim of this work was to evaluate the functional use of a commercial ASL sequence implemented on a 3 Tesla MRI system (Siemens, Verio) in the Imaging Department of *Hospital da Luz*. The first aim was to obtain a functional validation of this technique by comparison with the BOLD contrast, using a number of different approaches. The second aim was to accomplish perfusion quantification, by resolving some important quantification issues.

**Materials and Methods:** Fifteen adult volunteers participated in a single functional imaging session using three different protocols: one using BOLD and two using ASL. The subjects performed a motor finger tapping task and the data analysis was performed using Siemens Neuro3D and FSL (FMRIB's Software Library). The location and variability of the activated areas were analysed in MNI (Montreal Neurological Institute) standard space.

**Results:** Topographic agreement between the activated regions obtained by BOLD and ASL was found. However, the results show that inter-subject variability and distance to the hand motor cortex were smaller when measured with ASL as compared with BOLD fMRI. Quantitative studies revealed that ASL allows the calculation of cerebral blood flow (CBF), both at baseline and upon functional activation.

**Conclusion:** The results suggest that the functional imaging protocols using ASL produce comparable results to a conventional BOLD protocol, with the additional advantages of reduced inter-subject variability, better spatial specificity and quantification possibilities.

**Key-words:** fMRI (functional magnetic resonance imaging); ASL (arterial spin labeling), BOLD (blood oxygen level dependent); CBF (cerebral blood perfusion).





## Resumo

**Título:** Técnica de *Arterial Spin Labeling* em equipamento 3 Tesla na avaliação funcional da perfusão encefálica

**Introdução:** As sequências ASL (*arterial spin labeling*) recentemente disponíveis para a prática clínica, apresentam algumas vantagens relativamente ao contraste BOLD (*blood oxygen level dependent*) convencionalmente usado em estudos funcionais do cérebro com ressonância magnética (RM), nomeadamente, o facto de potencialmente permitirem a quantificação do fluxo sanguíneo cerebral (FSC), e de serem mais reprodutíveis.

**Objectivo:** O objectivo principal deste trabalho foi a realização do primeiro estudo funcional de uma sequência comercial de ASL da Siemens implementada no Hospital da Luz. Este estudo contém a avaliação comparativa da activação cerebral na função motora pelas técnicas BOLD e ASL. Algumas abordagens de quantificação do FSC foram também efectuadas.

**Materiais e Métodos:** Num equipamento 3 Tesla (Siemens, Verio) 15 voluntários saudáveis foram submetidos a um protocolo funcional usando o contraste BOLD e dois protocolos funcionais usando ASL, nos quais realizaram a tarefa motora da mão direita. Os dados foram processados no *software* Neuro3D (Siemens) e no FSL (FMRIB's Software Library). A localização e variabilidade das áreas de activação foram analisadas no espaço MNI (Montreal Neurological institute).

**Resultados:** Apesar de ter havido uma concordância topográfica entre as áreas de activação detectadas pelas duas técnicas, a região de activação detectada pela técnica ASL apresentou uma menor variabilidade entre os indivíduos e mostrou-se significativamente mais próxima do córtex motor da mão. Estudos quantitativos revelaram que a técnica ASL permite quantificar o FSC em estados de repouso e activação.

**Conclusão:** No contexto da RM funcional foi demonstrado que a técnica ASL produz resultados comparáveis com o convencional contraste BOLD, com as vantagens adicionais de reduzida variabilidade entre indivíduos, maior especificidade espacial e de permitir quantificar o FSC.

**Palavras-chave:** IRMf (imagem de ressonância magnética funcional); ASL (*arterial spin labeling*); BOLD (*blood oxygen level dependent*); FSC (fluxo sanguíneo cerebral).



## Abbreviations and Acronyms

ADP	Adenosine Diphosphate
AIF	Arterial Input Function
ANOVA	Analysis of Variance
ASL	Arterial Spin Labeling
ATP	Adenosine Triphosphate
BBB	Blood-Brain Barrier
BET	Brain Extraction Tool
BOLD	Blood Oxygen Level Dependent
CASL	Continuous Arterial Spin Labeling
(r)CBF	(regional) Cerebral Blood Flow
(r)CBV	(regional) Cerebral Blood Volume
(r)CMRO <sub>2</sub>	(regional) Cerebral Metabolic Rate of Oxygen
COG	Centre of Gravity
CSF	Cerebrospinal Fluid
CT	Computer Tomography
DSC	Dynamic Susceptibility Contrast
EPI	Echo-Planar Imaging
EPISTAR	Echo Planar Imaging and Signal Targeting with Alternating Radiofrequency
EV	Explanatory Variable
FAIR	Flow Alternating Inversion Recovery
FAST	FMRIB's Automated Segmentation Tool
FEAT	fMRI Expert Analysis Tool
FID	Free Induction Decay
FILM	FMRIB's Improved Linear Model
FLIRT	FMRIB's Linear Image Registration Tool
fMRI	Functional Magnetic Resonance Imaging
FOCI	Frequency Offset Corrected Inversion
FOV	Field of View
FSL	FMRIB's Software Library
FUGUE	FMRIB's Utility for Geometrically Unwarping EPIs
FWHM	Full Width at Half Maximum
GE	Gradient-Echo

GLM	General Linear Model
GM	Grey Matter
HMC	Hand Motor Cortex
HRF	Hemodynamic Response Function
MNI	Montreal Neurological Institute
MR	Magnetic Resonance
MRI	Magnetic Resonance Imaging
MT	Magnetization Transfer
MTT	Mean Transit Time
PASL	Pulsed Arterial Spin Labeling
PCT	Perfusion Computed Tomography
PET	Positron Emission Tomography
(r)OER	(regional) Oxygen Extraction Ratio
PICORE	Proximal Inversion with a Control for Off-Resonance Effects
PRECLUDE	Phase Region Expanding Labeller for Unwrapping Discrete Estimates
PVE	Partial Volume Effect
QUIPSS (II)	Quantitative Imaging of Perfusion using a Single Subtraction (version II)
Q2TIPS	QUIPSS II with Thin-slice $TI_1$ Periodic Saturation
RF	Radio Frequency
ROI	Region of Interest
SNR	Signal to Noise Ratio
SPECT	Single Photon Emission Computed Tomography
TCA	Trans-Carboxylic Acid
TE	Time to Echo
TI	Time to Inversion
TILT	Transfer Insensitive Labeling Technique
TR	Time to Repetition
$T_1$	Longitudinal relaxation time
$T_2$	Apparent transverse relaxation time
$T_2^*$	Transverse relaxation time
VASO	Vascular Space Occupancy
XeCT	Xenon-enhanced Computer Tomography

$B_0$	External magnetic field	$T_{1b}$	$T_1$ of arterial blood
$\gamma$	Gyromagnetic constant	$T_{1t}$	$T_1$ of tissue
$\Delta M$	Magnetisation difference	$\lambda$	Blood-brain partition coefficient
$M_0$	Equilibrium magnetisation	$f$	CBF in $s^{-1}$
$\delta t$	Arterial transit time		

# Contents

<b>Acknowledgements</b>	<b>v</b>
<b>Abstract</b>	<b>vii</b>
<b>Resumo</b>	<b>ix</b>
<b>Abbreviations and Acronyms</b>	<b>xi</b>
<b>Contents</b>	<b>xiii</b>
<b>List of Figures</b>	<b>xvii</b>
<b>List of Tables</b>	<b>xxi</b>
<b>Chapter 1 - Introduction</b>	<b>1</b>
1.1. Objective of the thesis.....	1
1.2. Previous work.....	1
1.3. Structure of the thesis.....	3
<b>Chapter 2 – Functional Neuroimaging</b>	<b>5</b>
2.1. Brain structure.....	5
2.1.1. Cerebral cortex.....	6
2.2. Brain functional anatomy: the hand motor cortex .....	7
2.3. Energy metabolism in the brain .....	8
2.4. Cerebral blood flow.....	9
2.4.1. The Meaning of Perfusion .....	10
2.4.2. Measuring CBF.....	11
2.4.2.1. Diffusible vs. Intravascular tracers.....	11
2.4.2.2. Techniques to measure CBF.....	12
2.5. Brain Activation .....	13

<b>Chapter 3 – Functional Magnetic Resonance Imaging</b>	<b>15</b>
3.1. Physics principles of MRI .....	15
3.2. Image acquisition.....	17
3.3. BOLD functional MRI .....	18
3.4. Perfusion functional MRI – ASL .....	19
3.4.1. Spin labelling methods: CASL and PASL.....	20
3.4.2. Quantification .....	21
3.4.2.1. The role of arterial transit time .....	24
3.4.2.2. Vascular artefacts.....	24
3.4.2.3. Inversion pulse shape and efficiency .....	25
3.4.2.4. Magnetisation transfer effects.....	26
3.4.2.5. Signal to noise issues.....	26
3.4.2.6. The role of blood equilibrium magnetisation .....	26
3.4.3. Clinical and Research applications.....	26
3.5. Comparison between BOLD and ASL measurements.....	27
<b>Chapter 4 – Materials and Methods</b>	<b>29</b>
4.1. Subjects.....	29
4.2. MR scanning .....	29
4.2.1. BOLD fMRI .....	29
4.2.2. ASL fMRI.....	30
4.2.2.1. ASL protocol #1 .....	31
4.2.2.2. ASL protocol #2 .....	32
4.3. Image analysis.....	32
4.3.1. Field map-based EPI distortion correction .....	33
4.3.2. Functional data .....	35
4.3.3. Segmentation of structural data .....	37
4.4. Data analysis.....	37
4.4.1. Variability and Localisation of motor activation.....	37
4.4.2. CBF quantification methods .....	39
4.4.3. CBF quantification in Rest and Activation conditions.....	40
4.4.4. SNR of perfusion-weighted images .....	41
4.4.5. CBF quantification: effect of anterior and posterior circulation .....	42
4.4.6. CBF quantification in GM and WM.....	42
4.4.6.1. Partial volume effect .....	42

<b>Chapter 5 – Results and Discussion</b>	<b>43</b>
5.1. EPI distortion correction .....	43
5.2. Comparing three functional protocols .....	46
5.3. Variability of extent and localisation of motor activation .....	51
5.4. CBF quantification: comparing the three methods.....	57
5.4.1. Inter-slices effect.....	59
5.5. CBF quantification in Rest and Activation conditions .....	62
5.5.1. Comparing ASL protocols .....	62
5.5.2. SNR of perfusion-weighted images .....	66
5.6. CBF quantification: effect of anterior and posterior circulation.....	68
5.7. CBF quantification in GM and WM.....	70
5.7.1. Partial volume effect correction .....	71
<b>Chapter 6 - Conclusions</b>	<b>75</b>
6.1. Discussion.....	75
6.2. Future prospects .....	76
<b>Bibliography</b>	<b>77</b>
<b>Appendix A - Appendix</b>	<b>81</b>
A.1. BOLD-ASL fusion in Neuro3D.....	81
A.2. Quantification maps Shell Script routine .....	84
A.3. Functional images for all subjects .....	88
A.4. Distance to the hand motor cortex.....	95
<b>Appendix B – Publications: Oral Communications</b>	<b>97</b>





## List of Figures

Figure 2.1: Relationship between an ideal map of brain activity and a metabolic and vascular map that generate functional images .....	5
Figure 2.2: Brain anatomic structure .....	6
Figure 2.3: Representation of the principal areas of the motor cortex .....	7
Figure 2.4: Representation of a dissected brain showing the precentral knob .....	8
Figure 2.5: Schematic diagram of the main steps of cerebral energetic metabolism .....	9
Figure 2.6: Vascular system of the brain .....	9
Figure 2.7: The meaning of perfusion .....	10
Figure 2.8: Physiological changes that accompanying brain activation.....	14
Figure 3.1: Different image contrasts .....	16
Figure 3.2: (a) EPI sequence diagram and (b) EPI k-space coverage order during one TR .....	17
Figure 3.3: Schematic illustration of hemodynamic changes during neuronal activity .....	18
Figure 3.4: The typical hemodynamic response function (HRF) .....	19
Figure 3.5: Schematic description of a perfusion weighted image ( $\Delta M$ ) obtained by subtraction of the labelled images from the control images, using the FAIR scheme.....	19
Figure 3.6: Continuous arterial spin labelling experiment.....	20
Figure 3.7: Pulsed arterial spin labelling experiment.....	21
Figure 3.8: A schematic of the idealized magnetisation difference curve with time .....	22
Figure 3.9: Vascular architecture showing the different vessel types that could pass through a typical tissue volume.....	25
Figure 3.10: A comparison of inversion profiles a hyperbolic secant (HS) pulse, a frequency offset corrected inversion (FOCI) pulse, and the rectangular ideal pulse .....	25
Figure 4.1: Motor task performed by all volunteers.....	30
Figure 4.2: Illustration of a typical prescription of the imaging slab positions for a) BOLD and b) ASL experiments, from sagittal scout scan.....	30
Figure 4.3: Pulse sequence used for Q2TIPS ASL imaging.....	31
Figure 4.4: Layout of GUI interface for FUGUE (part of FEAT), for applying EPI distortion correction. ....	34
Figure 4.5: Design matrixes for the three functional protocols performed with FEAT .....	36
Figure 4.6: Localisation of the hand primary motor cortex .....	38
Figure 4.7: Manually prescribed example ROIs for GM and WM SNR estimation.....	41

Figure 5.1: Field map image given by Neuro 3D from subject 4 .....	43
Figure 5.2: Phase difference image given by the scanner from subject 4.....	44
Figure 5.3: Field map obtained with FSL .....	44
Figure 5.4: 3D representation of one slice of the unwrapped field map .....	45
Figure 5.5: Distorted and undistorted EPI images of functional data .....	45
Figure 5.6: BOLD statistical map obtained with FSL from Subject 2 .....	46
Figure 5.7: Perfusion maps obtained with Neuro 3D, for 16 axial slices in one subject .....	47
Figure 5.8: Fusion between BOLD t statistical map and the ASL difference map between <i>relCBFactivation</i> and <i>relCBFrest</i> maps.....	48
Figure 5.9: Activation Z maps superimposed on an example EPI image obtained for each experiment of each protocol from subject 2.....	49
Figure 5.10: Activation Z maps (scale indicated in colorbar) obtained for each experiment of each protocol superimposed on the structural anatomic image from subject 2.....	50
Figure 5.11: Orthogonal views (coronal, sagittal and axial) of inter-subject activation maps for BOLD (red), BOLD <sub>ASL</sub> (green) and CBF (blue) in the MNI standard brain .....	53
Figure 5.12: 3D views of inter-subject activation clusters for BOLD (red), BOLD <sub>ASL</sub> (green) and CBF (blue).....	53
Figure 5.13: Localisation of the hand primary motor cortex.....	54
Figure 5.14: A plot of the group mean Euclidean distance (in mm) from HMC points to CBF, BOLD <sub>ASL</sub> and BOLD activation COGs.....	55
Figure 5.15: Representation of BOLD and CBF activations in coronal slices of subject 12 (presented from anterior to posterior, from left to right and from top to bottom in the figure), showing apparent activation over draining veins for BOLD experiment, but not for ASL.....	56
Figure 5.16: A typical perfusion-weighted image from a 25 years old female subject.....	57
Figure 5.17: A plot of perfusion values (in ml/100g/min) computed using the 3 methods for each subject and group mean .....	58
Figure 5.18: Illustration of the positions of the 9 axial slices acquired.....	59
Figure 5.19: A plot of perfusion values (in ml/100g/min) across the 15 subjects calculated with the 3 methods for the firsts 7 slices.....	60
Figure 5.20: Relation between arterial blood transit time in arbitrary units (a. u.) and the distance travelled in z-axis (in a. u.) .....	61
Figure 5.21: Theoretical curves of PASL signal versus time calculated from Equation 3.3 .....	61
Figure 5.22: A plot of perfusion change (%) between the conditions of rest and activation .....	63
Figure 5.23: Quantitative perfusion maps (8 axial slices) provided by ASL protocols from subject 9 ..	65
Figure 5.24: A plot of the group mean SNR of grey matter (GM) and white matter (WM) calculated for both protocols.....	66
Figure 5.25: A schematic diagram for the assessment of the perfusion maps of each functional protocol.....	67
Figure 5.26: Position of ROI 1 and ROI 2 .....	68
Figure 5.27: A plot of the group mean CBF values (in ml/100g/min) for each slice .....	69

Figure 5.28: Representation of the grey matter (GM) and white matter (WM), automatically segmented, binary masks.....	70
Figure 5.29: A plot of CBF values (ml/100g/min) in automatically segmented grey and white matter masks for each subject. ....	70
Figure 5.30: Representation of the grey matter (GM) and white matter (WM) partial volume maps. ....	72
Figure 5.31: A plot of CBF values (in ml/100g/min) of grey and white matters for each subject with and without partial volume effects correction.....	72
Figure 5.32: A plot of the mean ratios of grey to white matter perfusion in each of 7 slices calculated with (right) and without (left) partial volume effects correction.....	73
Figure A.1: Functional images from Subject 1.....	88
Figure A.2: Functional images from Subject 3.....	88
Figure A.3: Functional images from Subject 4.....	89
Figure A.4: Functional images from Subject 5.....	89
Figure A.5: Functional images from Subject 6.....	90
Figure A.6: Functional images from Subject 7.....	90
Figure A.7: Functional images from Subject 8.....	91
Figure A.8: Functional images from Subject 9.....	91
Figure A.9: Functional images from Subject 10. ....	92
Figure A.10: Functional images from Subject 11. ....	92
Figure A.11: Functional images from Subject 12. ....	93
Figure A.12: Functional images from Subject 13. ....	93
Figure A.13: Functional images from Subject 14. ....	94
Figure A.14: Functional images from Subject 15. ....	94



## List of Tables

Table 3.1 - $T_1$ and $T_2$ values of CSF, grey and white matters for a magnetic field of 3 Tesla .....	16
Table 4.1 – Functional data acquisition parameters.....	32
Table 4.2 - Perfusion quantification parameters used to calculate CBF .....	39
Table 5.1 - Results for the analysis of the location of activation measured by the centre of gravity (COG) and number of activated voxels for BOLD, BOLD <sub>ASL</sub> and CBF .....	52
Table 5.2 – Results for the calculation of variance of MNI COGs for CBF, BOLD <sub>ASL</sub> and BOLD activations across $N = 15$ subjects .....	52
Table 5.3 – Group mean Euclidean distance between modalities (BOLD, BOLD <sub>ASL</sub> and CBF) .....	56
Table 5.4 – CBF values in $ml/100g/min$ in the GM mask for each subject calculated using the three methods .....	58
Table 5.5 – CBF values provided by each protocol for both conditions of rest and activation for the 15 subjects .....	63
Table 5.6 – Mean CBF values in $ml/100g/min$ in GM and WM with and without partial volume effects (PVE) correction.....	73
Table A.1 – Group mean Euclidean distance (in mm) from HMC points (M3, M2, M1, CM and CC) to CBF, BOLD <sub>ASL</sub> and BOLD activation COGs for all subjects .....	95
Table A.2 - Group mean Euclidean distance (in mm) from HMC points (CL, L1, L2, L3, C1 and C2) to CBF, BOLDASL and BOLD activation COGs for all subjects .....	96



# Chapter 1

## Introduction

*In research one scientist's artefact is another scientist's science.*

*Richard B. Buxton*

### 1.1. Objective of the thesis

Cognitive neuroscience has obtained a powerful tool to study human brain function with the advent of functional magnetic resonance imaging (fMRI). Most notably, imaging sequences based on the blood oxygen level dependent (BOLD) contrast are currently the predominant method used for activation studies. However, the complex nature of the BOLD signal complicates the interpretation of its changes [1]. Perfusion fMRI, based on arterial spin labelling (ASL) methods, offers a useful alternative to BOLD fMRI. The ASL methods can provide quantitative measures of perfusion, or regional cerebral blood flow (CBF), without the need for contrast agents. Because it is widely accepted that CBF is a physiological correlate of brain activity, ASL methods can be used to measure not only baseline perfusion but also its functional changes. Importantly, changes in CBF are believed to be more directly linked to neuronal activity than the BOLD signal, so that perfusion fMRI also has the potential to offer more accurate measures of the spatial location and magnitude of neural function [1, 2].

The work presented in this thesis is the first study of the recently commercially available ASL sequence from Siemens at the 3 Tesla scanner of *Hospital da Luz* Imaging Department. It contains not only a series of approaches for functional validation of this technique in healthy volunteers, by comparison with BOLD contrast, but it also accomplishes some important quantification issues. The main objective was to provide the first results and comparative analyses between these two alternative and complementary fMRI techniques for clinical applications.

This thesis comprises the analysis and optimisation of the ASL sequence for functional studies, as well as the evaluation of its potential to provide quantitative values of CBF. Also, it presents some of the benefits and possible limitations of this technique by giving a small summary of its physical principles and assumptions.

### 1.2. Previous work

Within the last decade, the field of magnetic resonance imaging (MRI) has expanded to include studies of tissue function in addition to anatomy. Clinically, the pre-surgical mapping of eloquent

tissue can now be performed using fMRI techniques. Although the BOLD effect is most often used in brain activation studies, a drawback of this technique is that it only provides indirect information on the change in activity between one state and another, and does not provide a quantitative measure of cerebral activity. It provides no information, for example, on the resting or chronic perfusion state [1]. Moreover, when longitudinal experimental designs are employed in order to investigate processes taking place over long periods of time, BOLD information may not be valid.

There are two classes of MRI techniques that do provide measures of the resting perfusion state [2]. The first class is based on the use of an extrinsic tracer, namely intravascular contrast agents that alter the magnetic susceptibility of blood. The second is ASL, which uses magnetic labelling of inflowing arterial blood as a free-diffusible tracer, to obtain perfusion images. This technique is potentially quantitative and allows the extraction of absolute values for CBF. The main advantages of ASL over the first class technique, and over the majority of perfusion techniques, are improved spatial resolution and complete non-invasiveness requiring no potentially harmful contrasts injection. For that reason, it can be repeated without limit, and can be used to study normal physiology and its variations with time. It also has the potential to provide quantitative functional activation maps, which cannot be accomplished with BOLD fMRI studies [1].

The main ASL drawbacks are related to its intrinsically low signal-to-noise ratio (SNR) and the short life time of the label. The introduction of higher field scanners (like the 3 Tesla scanner) greatly benefited this technique, by improving the SNR of perfusion-weighted maps. Furthermore, in the last decade a number of improvements of the labelling strategies were introduced, which aimed to solve some of the problematic technical issues such as magnetisation transfer effects, and others [3].

Both BOLD and ASL methods are able to provide functional information of the brain, but they are quite different, and measure different aspects of brain hemodynamics. Previously, a number of fMRI studies made comparisons between ASL and BOLD contrast. Most of these studies were performed using BOLD acquired simultaneously with the ASL technique. Some of them suggest that perfusion changes have greater spatial resolution than BOLD changes during functional activation. Indeed, standard BOLD fMRI studies show apparent activation over relatively distant draining veins, which is not observed using perfusion contrast, suggesting that ASL may more accurately localise the region of neuronal activity [4]. Moreover, between-subject variability has been found to be smaller when measured with perfusion fMRI as compared with BOLD fMRI [5, 6], which implies that blood flow changes may be more consistent across subjects than changes in BOLD contrast. Another interesting result is that, as long as the same procedure and parameters are consistently used, more reproducible results have been achieved with ASL than BOLD [6] (see the review paper [7] for further comparisons between these two techniques).

Despite the remarkable progress over the last decade, ASL has not yet overtaken the traditional invasive methods of perfusion imaging in the clinics. However, with improved techniques and hardware available, in particular, the move toward 3 Tesla high-field scanners in the standard clinical environments, this method is now being pushed from the research and development stage headed for clinical applications.



### **1.3. Structure of the thesis**

This thesis begins by providing some background theory in Chapter 2, describing the basic biological and physiological aspects of brain function. Also, some of the most important neuroimaging techniques are mentioned, with particular emphasis on those that measure perfusion changes.

In Chapter 3, functional MRI techniques are introduced, including the theoretical background and main implementations of ASL. In particular, the perfusion quantification methods, and some of the problems and pitfalls involved, are thoroughly discussed.

The materials and methods used for this study are described in Chapter 4. It includes the methodology applied for the acquisition and processing of the images, as well as for the analyses and evaluation of the results. The subsequent approaches developed for the statistical analysis are also explained in this chapter.

Chapter 5 shows the experiments and results obtained in this work. The results are discussed in this chapter too. Finally, the conclusions drawn from this work are reported in Chapter 6.



## Chapter 2

### Functional Neuroimaging

The purpose of understanding the functional organisation of the human brain has inspired many neuroscientists for well over 100 years [1], but the experimental tools to measure and map brain activity have been slow to develop.

Neuronal activity is too difficult to localise without placing electrodes directly in the brain [1, 2]. Electric and magnetic fields measured at the scalp provide information on electric events within the brain, which allow the estimation of the location of a few sources of activity. However, precise localisation of the metabolic activity that follows neural activity is much more feasible and allows to produce a detailed map of the pattern of activation [1]. This is the basis of most of the functional neuroimaging techniques used today, including positron emission tomography (PET) and functional magnetic resonance imaging (fMRI). In fact, the physiological basis of these methods is the fact that brain cell activity is associated with local changes in metabolism [2], namely with glucose and oxygen consumption, and consequently also with haemodynamics, namely blood oxygenation, cerebral blood flow (CBF) and cerebral blood volume (CBV). Somehow nature performs a functional convolution of brain cell activity,  $f(x, t)$ , at a given location  $x$  and time  $t$  with the function “ $g$ ” which produces a certain change in metabolism and in haemodynamics [2]. The result is a map of metabolic and vascular events,  $g(f(x, t))$ , associated with changes in brain activity (see Figure 2.1).

So, in order to understand the functional images obtained with these methods, it is important to understand the relationship between local brain activity and the physiological parameters which are measured, and also the relationship between these physiological parameters and the obtained functional image (Figure 2.1). In this chapter these issues are discussed.

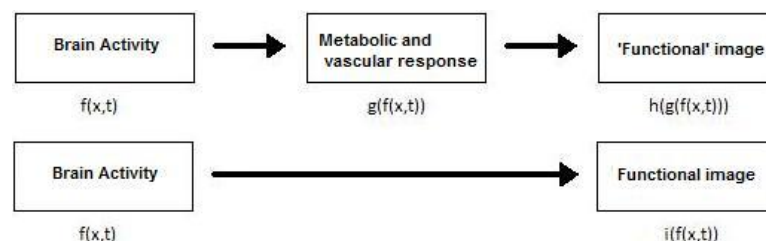


Figure 2.1: Relationship between an ideal map of brain activity and a metabolic and vascular map that generate functional images (adapted from [1]).

#### 2.1. Brain structure

Since early stages of human history, the brain has been one of the most studied parts of the human anatomy. Recent techniques have allowed increasing the knowledge about the brain structures and its functioning [8].

The normal adult human brain typically weighs between 1 and 1.5 kg and has an average volume of 1600 cm<sup>3</sup> [9], but receives 25% of all body blood flow. The basic anatomical brain structure can be seen in Figure 2.2 (a).

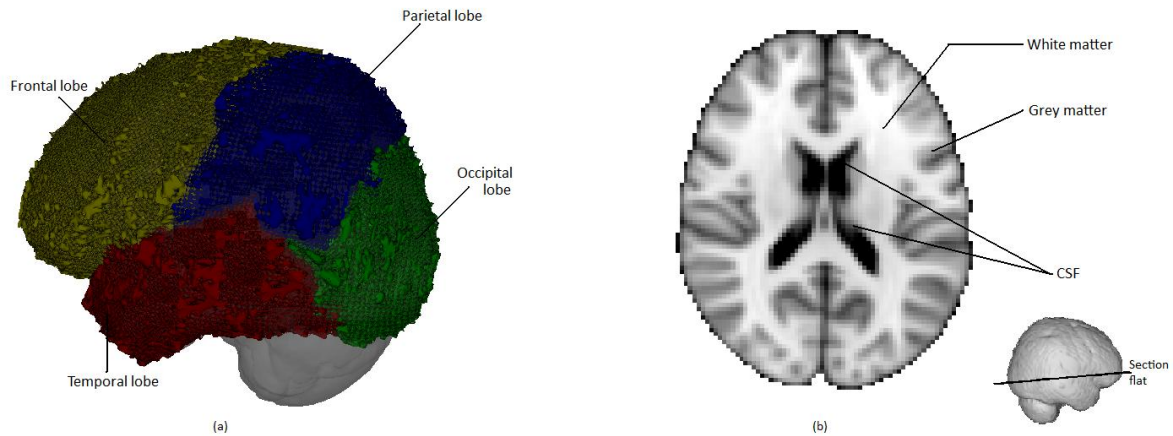


Figure 2.2: Brain anatomic structure. (a) Representation of temporal, parietal, frontal and occipital lobes. (b) Some of the different types of tissues in the brain.

This organ is composed of three main parts: the forebrain, midbrain and hindbrain [9]. The cerebellum, that is visible at the back of the brain (Figure 2.2 (a)), together with the pons and the medulla, compose the hindbrain. The medulla, pons and midbrain are often referred collectively as the brain stem. These structures are almost completely enveloped by the cerebellum and telencephalon, with only the medulla visible as it merges with the spinal cord [9]. As for the forebrain, it is composed by the cerebrum, thalamus and hypothalamus. The cerebrum is the largest part of the human brain and is divided into sections called “lobes” (Figure 2.2 (a)): the frontal, parietal, occipital and temporal and insular lobes [9].

In the next subsection, a more thorough review of the cerebrum is shown, as this work is mainly focused in tissue detection in this particular area of the brain.

### 2.1.1. Cerebral cortex

The cerebrum is composed of an outer layer of grey matter, internally supported by deep brain white matter. It is responsible for the so called “higher functions”, such as thinking and cognition [8].

Grey matter consists of cell bodies of neurons, while white matter consists of axons that connect neurons. These are often surrounded by a fatty insulating cover called myelin, which gives the white matter its distinctive colouration (see Figure 2.2 (b)). The function of this fatty sheath is to insulate nerve endings, enable smoothly movements of brain signals and to accelerate the transmission of the nerve signals [9].

The brain is surrounded by the meninges and the subarachnoid space, which separates the soft brain tissues and spinal cord from the hard surrounding bones like skull and vertebrae. This space and the cavities located inside the brain, the ventricular system, are filled with cerebrospinal fluid (CSF), which is believed to be produced by the choroid plexus [9] (Figure 2.2 (b)). The CSF is very similar to blood plasma and is the other supplier of nutrients to the brain.

These are the main tissue types that are of interest in this study.

## 2.2. Brain functional anatomy: the hand motor cortex

The cortical anatomy of cerebral gyri is complex and presents tremendous intra- and inter-subject variability [9]. Therefore, the identification of specific cortical regions based only on morphologic features can be challenging. The presence of space-occupying lesions in the brain, such as tumors or vascular malformations, can further complicate this procedure by distorting normal anatomy, thereby making the identification of specific cortical regions difficult or impossible.

Previous studies have demonstrated that the motor function is controlled by four major regions in the frontal lobe: the primary motor cortex (M1), which lies just anterior to the central sulcus on the precentral gyrus, the supplementary motor area (SMA), the premotor area and the cingulate motor area which lie just anterior to M1 (shown in Figure 2.3). The motor cortex located on the left side of the brain controls movement on the right side of the body [9].

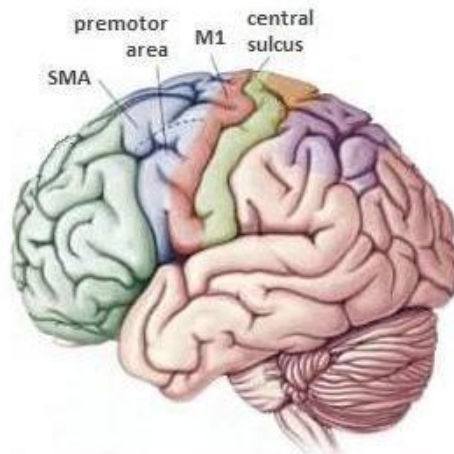


Figure 2.3: Representation of the principal areas of the motor cortex (adapted from [9]).

The cortical representation of motor hand function, which allowed the development of the concept of “homunculus”, is known to be located in the superior aspect of the precentral gyrus [10]. Even though functional techniques have recently permitted the identification of anatomic regions based on the correspondence with regions of activation, the knowledge of pure anatomic landmarks of the cerebral cortex remains of fundamental importance in research and everyday clinical practice.

Yousry et al. [10] described the hand motor cortex (HMC) in dissected brains or computed tomography and MR imaging as having the shape of a typical hook on the sagittal plane and a structure like an inverted omega ( $\Omega$ ) or epsilon ( $\epsilon$ ) on the axial plane (see Figure 2.4). They also localized blood oxygen level dependent (BOLD) activation, obtained during hand movement exactly on the omega region of the precentral gyrus.

In summary, the most reliable landmark for the identification of HMC is the inverted omega or horizontal epsilon shape of the precentral gyrus in axial scans, or the shape of a posteriorly directed hook in the sagittal plane.

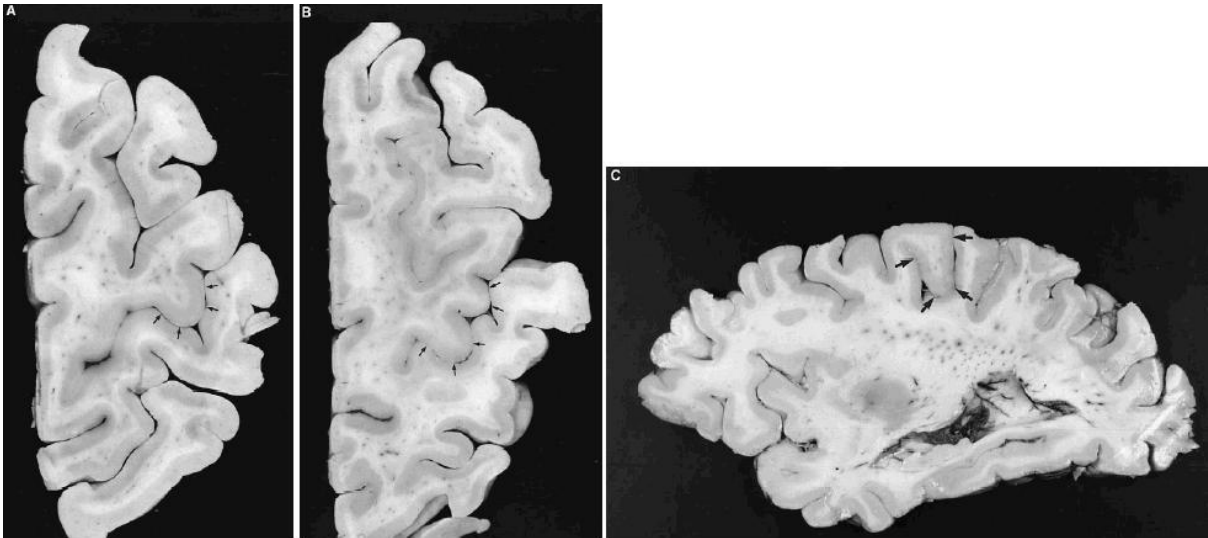


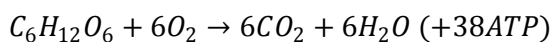
Figure 2.4: Representation of a dissected brain showing the precentral knob (indicated by arrows), which can look like an inverted omega (A) or a horizontal epsilon (B) when cut axially, and like a hook when cut sagittaly (C) [10].

### 2.3. Energy metabolism in the brain

Like in all organs, energy metabolism in the brain is necessary for the basic processes of cellular work, such as chemical synthesis and chemical transport [1]. Still, the particular work done by the brain, which is the generation of electrical activity required for neuronal signalling, such as the generation of an action potential and the release of neurotransmitter at a synapse, requires a high level of energy metabolism [11].

In biologic systems the free energy necessary for these tasks is primarily stored in relative proportions of three nucleotides: adenosine triphosphate (ATP), adenosine diphosphate (ADP) and adenosine monophosphate (AMP), being ATP the main source of energy for cells [11]. ATP production is dependent on the combination of glucose and oxygen. The metabolism occurs in two stages: glycolysis and the trans-carboxylic acid (TCA) cycle (also known as the citric acid cycle or the Krebs cycle) [11, 12]. Glycolysis does not require oxygen but the further metabolism of glucose through the TCA cycle requires oxygen and produces much more ATP (see Figure 2.5).

Oxidative glucose metabolism involves many steps and different reactions which are catalyzed by different enzymes within the cell. At the end of the process, carbon dioxide and water are produced, and an additional 38 ATP molecules are created. The overall metabolism of glucose is then



As we know, regional energy requirements are different across the brain, so the delivery of oxygen and glucose is also distinct in different regions of the brain. 90% of the glucose metabolized requires oxygen [1], therefore neuronal metabolic activity can be directly associated to oxygen consumption. Furthermore, we know that blood flow is the responsible for delivering glucose and oxygen to the brain tissues. According to this, neuronal activation induces an increase of the oxygen consumption, which is accomplished with an increase of blood flow [1].

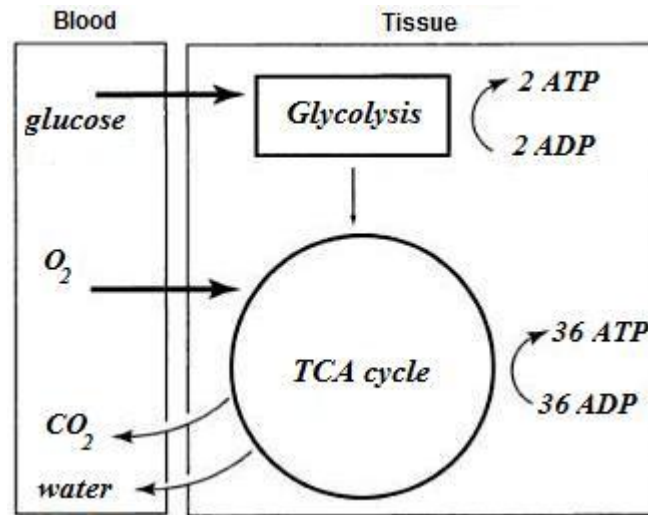


Figure 2.5: Schematic diagram of the main steps of cerebral energetic metabolism (adapted from [1]).

## 2.4. Cerebral blood flow

The vascular system that supplies blood to the brain is organised on a spatial scale that spans a range of four orders of magnitude, from the diameter of a capillary (about  $10\ \mu\text{m}$ ) to the size of a major artery (about  $3\ \text{cm}$ ) [1]. The complexity of the vascular system of the brain can be appreciated from images in Figure 2.6. In short, the architecture of the vascular tree shows distinct organisation on a spatial scale as small as a few hundred micrometers.

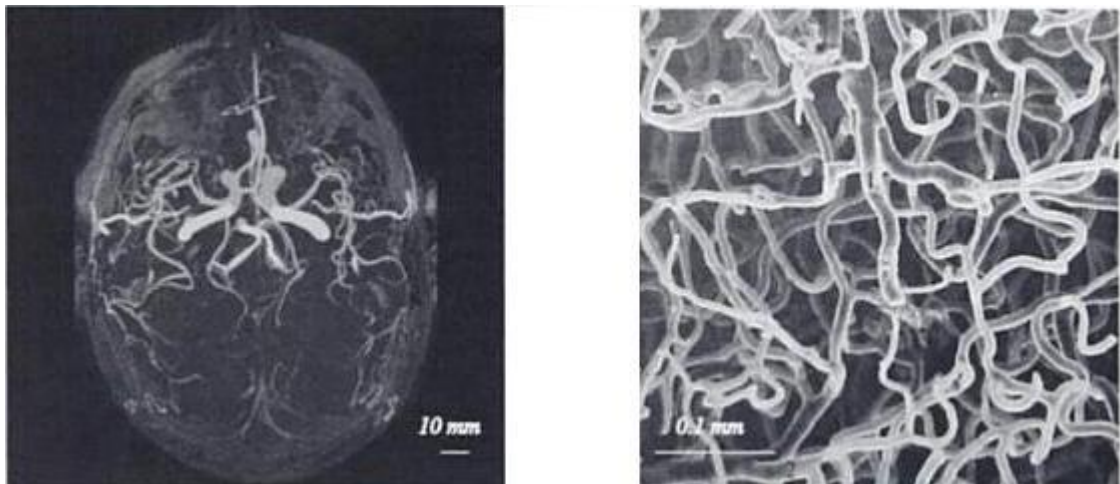


Figure 2.6: Vascular system of the brain [1]. In the left image there's an MR angiogram showing the main arteries supplying blood to brain tissues, and the veins which drain that tissues. In the right image a microscopic view is presented, showing the complex geometry of small vessels: arterioles, capillaries and venules.

As suggested earlier, cerebral blood flow (CBF) delivers glucose and oxygen to the brain, so it is obvious to assume that local CBF varies with neural activity. The measurement of CBF changes with activation assumes a vital importance in the understanding of basic physiological processes and pathologies. Different functional imaging techniques, including fMRI, rely on CBF changes, so is important to understand what it is and how it can be measured.

### 2.4.1. The Meaning of Perfusion

The term *perfusion* is generally used to describe the process of nutritive delivery of arterial blood to a capillary bed in the tissue and cells. Since cerebral haemodynamics is one of the key aspects in functional neuroimaging, it is important to describe it in terms of a number of clearly defined variables. One of these variables is the *cerebral blood flow*, defined as the rate of delivery of arterial blood to the capillary beds of a particular mass of tissue [1], as illustrated in Figure 2.7 (a). In this idealized tissue vasculature, the flow rates through both capillary beds are designated  $F_1$  and  $F_2$  (expressed in millilitres per minute), and if these vessels feed a volume of tissue  $V$ , then CBF is simply  $(F_1 + F_2)/V$ . For convenience, a common unit for CBF is millilitres of blood per 100 grams of tissue per minute, and a typical average value in the human brain is  $60 \text{ ml}/100\text{g}/\text{min}$  [1]. However, in some circumstances it is convenient to express CBF as flow delivered to a unit volume of tissue rather than a unit of mass of tissue. For instance, in imaging applications a signal is measured from a particular volume in the brain, and the actual mass of tissue within that volume is not known. Because the density of brain is close to  $1 \text{ g}/\text{ml}$  [1], CBF values expressed in these units are similar (it means that  $60 \text{ ml}/100\text{g}/\text{min}$  is equivalent to  $0.01 \text{ s}^{-1}$ ).

The cerebral blood volume (CBV) is the fraction of the tissue volume occupied by blood vessels, and a typical value for the brain CBV is 4% ( $\text{CBV} = 0.04$ ) [1]. The CBV is a dimensionless number (millilitres of blood vessel per millilitre of tissue), and generally refers to the entire vascular volume within the tissue. However, in some occasions it's important to subdivide total CBV into arterial, capillary and venous volumes, where typical estimate numbers are 5% for the arterial volume and 95% equally divided for capillaries and veins [1].

The velocity of blood in the vessels is also an important physiological parameter, which varies from tens of centimetres per second in large arteries to as slow as one millimetre per second in the capillaries [1].

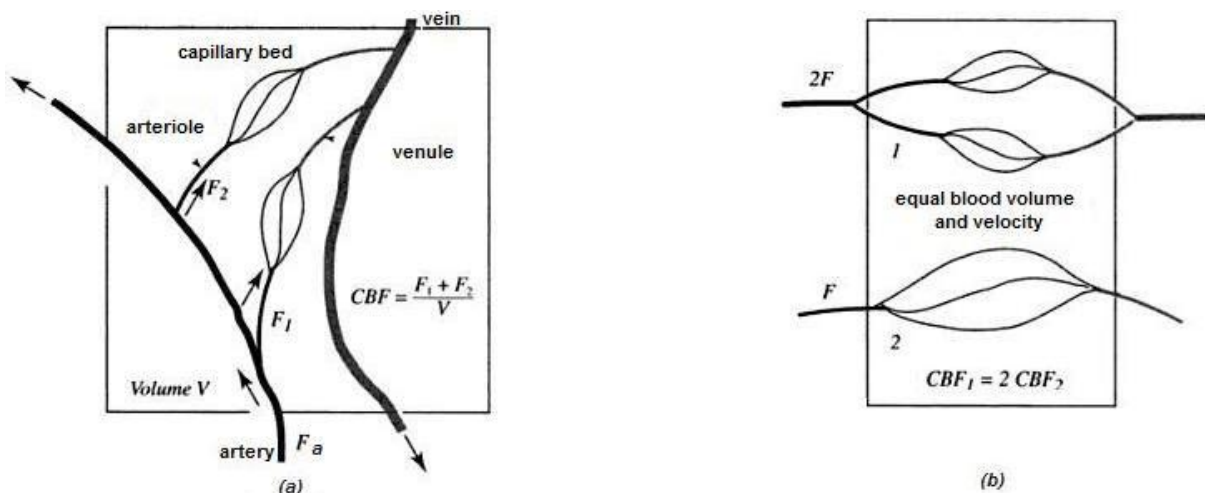


Figure 2.7: The meaning of perfusion (adapted from [1]). (a) Illustration of blood vessels within a small element tissue for cerebral blood flow definition. (b) Demonstration of the incapacity to calculate CBF with blood volume and velocity.

Although CBF, CBV and blood velocity are all important aspects of the perfusion state of tissue, they are distinct physiological quantities [13]. From the preceding definitions, it can be noticed that



CBF does not explicitly depend on either blood volume or the velocity of blood in the vessels, i.e., an increase in CBF with brain activation could occur through a number of different changes in blood volume or blood velocity. In Figure 2.7 (b) two idealized capillary beds are shown, one with two sets of shorter capillaries, and one with a single set of capillaries twice as long. Both beds show the same blood velocity and CBV. However, CBF is twice as large in the top bed with two sets of shorter capillaries. The missing piece that does differ between the two scenarios and is responsible for this difference is the capillary transit time [13]. In the bottom bed the capillary transit time is twice as long. And it is transit time, rather than blood velocity, that is directly connected to CBV and CBF. The relation between CBV, CBF and the mean transit time ( $MTT$ ) through the volume CBV is known as the central volume principle, and is defined as:

$$MTT = CBV / CBF$$

For a CBF of  $60 \text{ ml}/100\text{g}/\text{min}$  ( $0.01 \text{ s}^{-1}$ ) and a typical CBV of 4%, from this equation  $MTT$  is 4 s.

In summary, the definition of CBF involves some subtleties that have to be considered when we want to measure it. Some of these subtleties consist in particular properties of the measuring technique that we use. For this reason an accurate approach is necessary to properly measure CBF.

## 2.4.2. Measuring CBF

Numerous imaging techniques have been developed and applied to evaluate brain hemodynamics [14]. Most of those techniques rely on mathematical models developed at the beginning of the century, giving similar information about brain hemodynamics in the form of different parameters such as CBF or CBV. For that purpose, they use different tracers to mimic perfusion and have different physical principles and different technical requirements.

### 2.4.2.1. Diffusible vs. Intravascular tracers

The various tracers used in brain studies usually fall into one of two basic classes, diffusible tracers and intravascular tracers, which differ in their volume of distribution [1, 2]. Nitrous oxide, for example, freely diffuses out the capillary bed and fills the entire tissue space, so its volume of distribution is essentially the whole brain volume. On the other hand, an agent that remains in the blood has a volume of distribution that is much smaller, only about 4% of the total brain volume [1]. For an intravascular agent the time constant for the venous blood to equilibrate with the arterial blood is corresponding shorter, or in other words, for the same flow, the volume of distribution of an intravascular agent is quickly filled because the blood volume is only a small fraction of the total tissue volume [1].

This difference in the equilibrium times directly affects what can be measured with diffusible and intravascular tracers [1]. Considering that the tissue concentration of an agent (which is injected into

blood) is measured over time, once the agent has reached equilibrium within its volume of distribution, the tissue concentration of the agent is independent of flow but provides a robust measure of the volume of distribution. Therefore, an intravascular agent provides a robust measurement of CBV, because that is its volume of distribution, but a poor measurement of flow, because it equilibrates too quickly. In contrast, a diffusible tracer provides a robust measurement of flow because the time for equilibrium is much longer.

These basic ideas suggest that the perfusion techniques applied to measure local CBF use diffusible tracers.

#### 2.4.2.2. Techniques to measure CBF

The main imaging techniques dedicated to brain hemodynamics are positron emission tomography (PET), single photon emission computed tomography (SPECT), Xenon-enhanced computed tomography (XeCT), dynamic perfusion computed tomography (PCT), Doppler ultrasound, MRI dynamic susceptibility contrast (DSC) and arterial spin labelling (ASL).

PET is a powerful diagnostic tool, considered in early times the gold standard technique for brain perfusion evaluation [14], that provides tomographic images of quantitative parameters describing regional CBF (rCBF), regional CBV (rCBV), regional oxygen extraction fraction (rOEF), regional cerebral metabolic rate of oxygen (rCMRO<sub>2</sub>) or glucose, neurotransmission processes, etc. These images result from the use of different substances of biological interest labelled with positron emitting radioisotopes. The most commonly used tracer to measure CBF is H<sub>2</sub><sup>15</sup>O [15], which is administered directly by intravenous injection. A few minutes scan is performed and its results combined with an arterial blood sampling measurement, performed in order to obtain the input function, leads to quantitative CBF maps.

SPECT was introduced soon after PET. Besides some technical aspects, like the equipment involved, the main difference between SPECT and PET is that the first one uses radioisotopes which emit gamma photons, such as <sup>99m</sup>Tc [15]. Perfusion PET and SPECT methods afford whole brain coverage and provide valuable information, giving quantitative CBF maps [14, 15]. However, the spatial resolution of these nuclear imaging studies ranges from  $\approx 4$  to  $6$  mm [14]. Its clinical applications are still limited due to their high price and specific technical requirements. In addition to the access to radiopharmaceuticals, PET requires the access to a cyclotron near the administration local. Furthermore, in PET or SPECT examinations, the whole body is exposed to radiation.

After the introduction of computed tomography (CT) two methods for evaluating CBF were developed, both based on administration of a contrast agent. Dynamic PCT uses first-pass tracer methodology after bolus infusion of an intravenous iodinated contrast material, and provides CBF, CBV, MTT and blood brain barrier (BBB) permeability [14]. The other CT method uses stable xenon gas (Xe). When inhaled, this gas dissolves into the blood, freely crosses the BBB and enters the brain, and then its concentration in the brain can be directly measured with a CT scanner [14]. Unlike most methods of imaging CBF, XeCT is truly quantitative and has been found to be accurate even at very low and very high flow rates. A spatial resolution  $2$  mm is routinely available [14]. An additional

advantage is its rapid elimination, which makes repeated scanning under different conditions possible. Nonetheless, Xe is a narcotic gas, and even if it was used in low doses, some side effects can be seen, like euphoria, raising the need of permanent medical assistance during the imaging procedure. Moreover, dynamic PCT and XeCT use ionizing radiation, and as PET and SPTEC methods, they are not completely non-invasive techniques [15].

Although different in nature from other imaging techniques described hereby and accordingly limited in spatial resolution, Doppler ultrasound offers the advantage of being non-invasive and repeatable as often as clinically indicated at the patient's bedside [14]. It doesn't involve radiation, doesn't require any contrast medium, and is free of any known adverse effect. Considering these facts, ultrasound Doppler technology may represent a convenient tool for the measurement of blood flow volume in the internal carotid artery as a correlate for CBF in the corresponding hemisphere [14].

MRI also provides two approaches to measuring CBF. Like first-pass PCT, the first of these approaches, DSC, implies the administration of a contrast agent [14, 15] that remains intravascular. In addition, MR contrast agents alter image intensity indirectly affecting the surrounding tissues. The other MRI method for imaging CBF, ASL, does not require administration of a contrast agent, and provides direct measures of CBF changes [15]. Most importantly, this MR method requires neither exposure to form of radiation (as XeCT), nor administration of a contrast agent (as MR DSC), and measures can be repeated as often as required. A more detailed discussion of this last technique will be given in Chapter 3.

## 2.5. Brain Activation

The real nature of the coupling between CBF and  $CMRO_2$  during activation is still debated. However, the tomographic techniques have provided experimental data for the generation of some theories that explain the energetic metabolism of the brain.

The primary finding is that CBF increases substantially during brain activation [16]. The increase is localised and is a graded response in the sense that the magnitude of the flow change is often correlated with other measures of the degree of neural activity. The second finding is that  $CMRO_2$  increases much less than CBF [16]. The main reason for that or at least the most accepted one nowadays, is that this unclear disconnection between CBF and  $CMRO_2$  is due to a large and disproportional essential increase on CBF to supply a small increase of the oxygen consumption during activation [17]. This oxygen limitation model is based on two assumptions: the first one is that the supply of oxygen to the tissue is limited by BBB, which means that only a small rate of the supplied oxygen is available for metabolism. The second one is that CBF increasing is accompanied by an increase of blood velocity in the capillaries rather than the capillary recruitment [17]. In summary, the result of this imbalance in the changes of CBF and  $CMRO_2$  is a substantial drop in oxygen extraction like is shown in Figure 2.8.

The scheme of Figure 2.8 implies that CBF and metabolism are linked under physiological conditions but can be uncoupled by selective manipulations or under particular pathophysiological

conditions [17]. With the introduction of techniques such as fMRI, it was possible to piece together an empirical picture of the physiological changes that accompany brain activation and form the basis for functional neuroimaging.

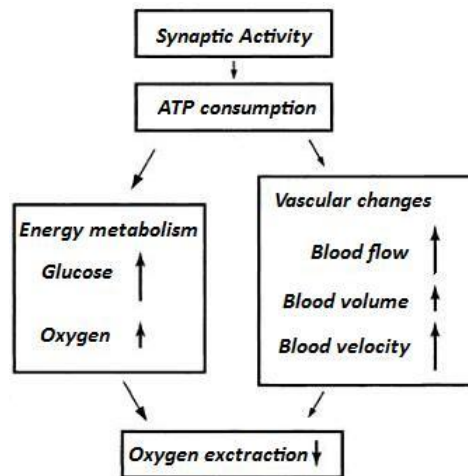


Figure 2.8: Physiological changes that accompanying brain activation (adapted from [1]).

## Chapter 3

### Functional Magnetic Resonance Imaging

Functional magnetic resonance imaging (fMRI) provides a sensitive, non-invasive tool for mapping patterns of activation in the working human brain. However, how this tool works is far from obvious, and to understand the strengths and limitations of fMRI it is necessary to delve into the nature of the magnetic resonance (MR) signal and how it can be measured and affected by brain activation.

#### 3.1. Physics principles of MRI

Magnetic Resonance Imaging (MRI) is a non-invasive imaging technique that allows to produce high quality images of living organisms [1]. This technique is also known as magnetic resonance tomography or nuclear magnetic resonance.

MRI is based on the principles of nuclear magnetic resonance. It measures spatial variations in the phase and frequency of the radio-frequency energy being absorbed and emitted by the imaged object [18].

There is a huge amount of atoms in the human body. The ones with nuclei with an odd number of protons and neutrons possess a property called spin, which is its intrinsic angular momentum and can attain any value multiple of  $1/2$ . When these spins are placed in a strong external magnetic field ( $B_0$ ) they precess around an axis along the direction of the field, aligning in two energy “eigenstates” (analogous to the *Zeeman Effect*): one low-energy and one high-energy, which are separated by a very small splitting energy [18]. This precession frequency  $\nu$  is called the Larmor frequency and is obtained (with the gyromagnetic ratio of nucleus,  $\gamma$ ) from the Larmor equation:

$$\gamma B_0 = \nu \quad \text{Equation 3.1}$$

After exposing the object of study to a magnetic field, a transient radio frequency (RF) pulse at the characteristic Larmor frequency is briefly applied, in a plane perpendicular to  $B_0$ . This RF pulse excites some of the spins in the lower energy state at their resonant frequency, disturbing the aligned hydrogen nuclei, thus causing a disruption of the equilibrium. From this disturbance of equilibrium, two effects arise: longitudinal and transverse magnetisation [18]. So, the RF pulse causes an oscillatory effect on the component of the magnetisation vector ( $M$ ) parallel to the z axis, and a small component of the magnetisation will be in the x-y axis, which can be detected. The angle that the net magnetisation vector rotates is commonly called the flip angle [19].

When the RF pulse is turned off, the transverse vector component produces an oscillating magnetic field which induces a small current in a receiver coil. This signal is called free induction

decay (FID) [19]. In an idealized MR experiment, the FID decays approximately with a time constant called  $T_2$ , which is the time that takes transverse magnetisation to decrease 63% of its value when the RF pulse is turned off. However, in practical MRI small differences in the static magnetic field at different spatial locations (inhomogeneities) cause the Larmor frequency to vary across the body creating destructive interference which shortens the FID. The time constant for the observed decay of the FD is called the  $T_2^*$  relaxation time, and is always shorter than  $T_2$ . Also, when the RF pulse is turned off, the longitudinal magnetisation starts to recover exponentially with a time constant  $T_1$ , which is the time for the magnetisation to return to 63% of its original length [19].

In MRI, the static magnetic field is caused to vary across the body (by applying field gradients using appropriate coils), so that different spatial locations become associated to different precession frequencies. Usually these field gradients are pulsed, and it is the almost infinite variety of RF and gradient pulse sequences that gives MRI its versatility. The application of a field gradient destroys the FID signal, but this can be recovered and measured by a refocusing gradient (to create a so-called *gradient echo*), or by a RF pulse (to create a so-called *spin echo*). The whole process can be repeated when some longitudinal relaxation has occurred and the thermal equilibrium of the spins has been more or less restored [19].

Typically in soft tissues  $T_1$  is around one second while  $T_2$  and  $T_2^*$  are a few tens of milliseconds, but these values vary widely between different tissues (and different  $B_0$ ), giving MRI its tremendous soft tissue contrast (see Table 3.1) [19].

Table 3.1  
 $T_1$  and  $T_2$  values of CSF, grey and white matters for a magnetic field of 3 Tesla [20]

Tissue	$T_1$ (ms)	$T_2$ (ms)
White matter	832	110
Grey matter	1331	80
CSF	2500	250

Thus, image contrast is created by differences in the strength of the MR signal recovered from different locations within the sample, which depends upon the relative density of excited nuclei (usually water protons), on differences in relaxation times of those nuclei after the pulse sequence [18]. Furthermore, image contrast relies on other parameters (controlled by users): the echo time (TE) which is the time between the centre of the initial RF pulse (in a pulse sequence) and the centre of the signal echo formed by that pulse, and the repetition time (TR) which is the amount time that exists between successive excitation pulse sequences (see Figure 3.1) [19].



Figure 3.1: Different image contrasts [19]. From left to right:  $T_1$ -weighted, proton density-weighted and  $T_2$ -weighted images.

### 3.2. Image acquisition

The quality and contrast of the image acquired with MRI can be manipulated by the use of different image acquisition techniques. The main steps usually consist on slice selective excitations, frequency encoding and phase encoding, which result in data being collected in a spatial frequency space – the k-space<sup>1</sup>. Image reconstruction is then accomplished by performing a 2D inverse Fourier transform of the raw data. The exact timings and characteristics of the acquisition determine the resolution and contrast of the image [19]. Many methods of image acquisition have been developed in order to reduce the image acquisition time, which is very useful for functional studies.

Gradient-echo (GE) - echo-planar imaging (EPI) sequences are the commonly used in such applications. This acquisition module is based on the collection of the data necessary to reconstruct an image using one set of echoes after a single RF excitation and a short phase encoding gradient between each echo [14]. The EPI sequence diagram is showed in Figure 3.2 (a).

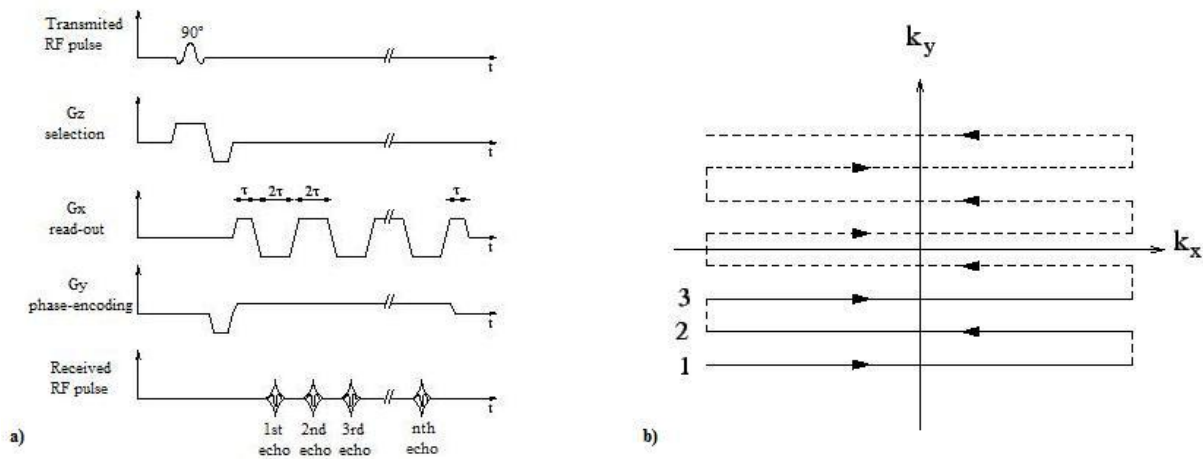


Figure 3.2: (a) EPI sequence diagram and (b) EPI k-space coverage order during one TR (adapted from [14, 19]).

Figure 3.2 (b) shows the k-space sampling trajectory determined by the EPI sequence. All k-space lines are acquired in only one shot and each line is acquired in the opposite direction relatively to the previous one. This effect results in the phase accumulation (N) in different directions in odd and even lines of the k-space. After image reconstruction it leads to an N/2 shift of the object representation, which can lead to the Nyquist ghosting effect. The main advantages of EPI readout are the short acquisition time, efficiency, regular k-space coverage and acceptable signal to noise ratio (SNR), and it can be combined with many spin preparation methods. However, the EPI acquisition is very sensitive to susceptibility induced field changes and inhomogeneities which may be useful for fMRI studies [21]. However, this property can also lead to signal drop-out and image distortions. In fact, image distortion occurs frequently near the sinuses, due to the magnetic field differences between the air (in the sinuses) and the brain tissues [14]. The readout, x, direction of the k-space is acquired with a high bandwidth (fast acquisition), while the phase-encoding direction, y, is acquired more slowly. The image quality depends on the echo spacing for a given resolution and phase errors, and consequently geometric distortions, appear predominantly in the phase encoding direction.

<sup>1</sup> K-space is a temporary virtual space enclosing the phase and frequency of imaging data and it functions to simplify their conceptualization.

### 3.3. BOLD functional MRI

Although susceptibility effects can produce artefacts when imaging the brain (as mentioned in the previous section), they are the basis of the generation of the blood oxygen level dependent (BOLD) contrast that is the basis of most functional MRI studies [22].

The magnetic susceptibility effect at the basis of BOLD experiments arises from the biophysics of the haemoglobin molecule, which provides oxygen required for aerobic energy metabolism [23]. As blood leaves the lungs, oxygen becomes loosely and reversibly bonded to an iron atom that lies at the center of the heme molecule within the haemoglobin complex. When delivered to tissue, oxygen separates from the heme molecule exposing electrons from the iron atom. The unpaired iron electrons alter the lines of the magnetic field near the deoxyhemoglobin molecule, which causes slight dephasing of the spins of the hydrogen nuclei in proximal water molecules of both blood vessels and adjacent tissues [23, 24]. These effects occur because haemoglobin is diamagnetic when oxygenated but paramagnetic when deoxygenated. The MR signal of blood is therefore slightly different depending on the level of oxygenation. Higher BOLD signal intensities arise from increases in the concentration of oxygenated haemoglobin since the blood magnetic susceptibility now more closely matches the tissue magnetic susceptibility [23].

Chapter 2 laid the foundation for understanding how fMRI based on BOLD effect works. Brain activation is characterized by a drop in the local oxygen extraction fraction (OEF) and a corresponding drop in the local concentration of deoxyhemoglobin, which produces a small increase in the MR signal (see Figure 3.3) [24]. Thus, using deoxyhemoglobin as an endogenous tracer, regional brain activation can be mapped with  $T_2^*$  sensitive pulse sequences, such as the GE sequence.

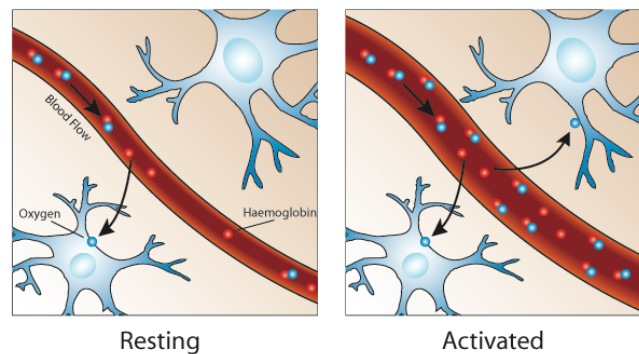


Figure 3.3: Schematic illustration of hemodynamic changes during neuronal activity [25]. From the basal state (resting) to activated state a decrease of deoxyhemoglobin concentration occurs in the capillaries and venules, resulting in an increase in the BOLD signal intensity.

In summary, BOLD contrast does not reflect a single physiological process, but rather represents the combine effects of cerebral blood flow (CBF), cerebral blood volume (CBV) and cerebral metabolic rate of oxygen ( $CMRO_2$ ) [24]. Furthermore, the sluggish response of the vascular system to neural events delays, disperses and smooths over time the underlying neural signal [22]. This implies that the observed BOLD signal is generally a composition of signals produced by separate neural events. The MR signal plots in Figure 3.4 show an idealization of the BOLD signal due to brief stimulation. This signal, also called hemodynamic response function (HRF), is complex, with an initial



drop followed by the rise to a single maximum, a decline, and an undershoot before returning to baseline [21]. The HRF characteristics vary between different regions of the brain and depend on the stimulus and its duration [26]. A detailed biophysical explanation of the complex shape of the BOLD signal is a current area of research.

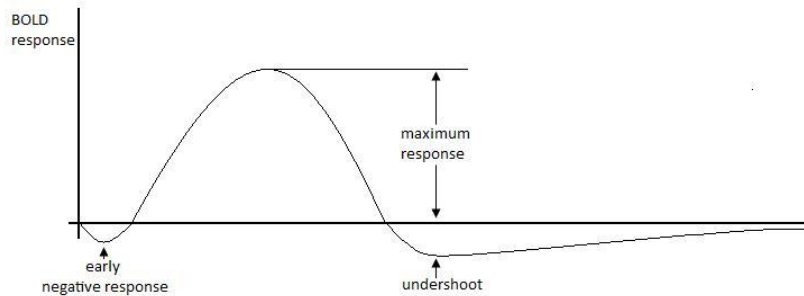


Figure 3.4: The typical hemodynamic response function (HRF): BOLD response to a brief stimulus (adapted from [18]).

### 3.4. Perfusion functional MRI – ASL

Arterial spin labeling (ASL), also called arterial spin tagging, is a non-invasive MRI method to measure brain perfusion.

The overall goal of all existing ASL techniques is to produce a flow-sensitized image or labelled image and a control image in which the static tissue signals are identical, but where the magnetisation of the inflowing blood differs [27]. The subtraction control-label ( $M_{control} - M_{tag}$ ) yields a signal difference  $\Delta M$  that directly reflects local perfusion, because the signal from stationary tissue is completely eliminated (Figure 3.5). The label is usually performed by inverting or saturating the spins of water molecules of the blood supplying the imaged region [27, 28]. Once the labelled blood spins are allowed to reach the capillary bed, which is accomplished with a delay between the labelling and image acquisition, they exchange with tissue water and thereby give rise to the perfusion signal. The signal difference, which is only 0.5 – 1.5% of the full signal, depends on many parameters such as the flow itself, the  $T_1$  of blood and tissue, as well as the time it takes blood to travel from the labelling slab to the imaging region [27]. Multiple repetitions are needed for ensuring sufficient SNR, and a model of the perfusion signal is usually used in order to quantify CBF.

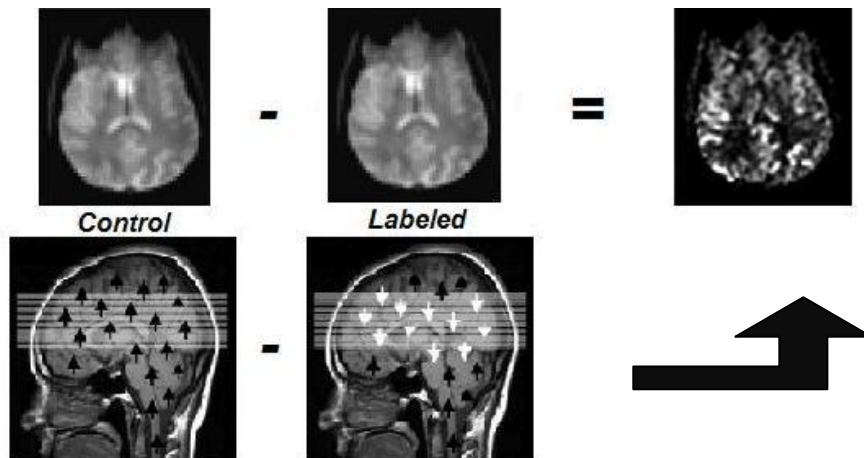


Figure 3.5: Schematic description of a perfusion weighted image ( $\Delta M$ ) obtained by subtraction of the labelled images from the control images, using the FAIR scheme (adapted from [27, 28]).

### 3.4.1. Spin labelling methods: CASL and PASL

There are two main classes of ASL techniques: continuous ASL (CASL) and pulsed ASL (PASL). Although both approaches share a similar basis, they present different benefits and limitations that affect their abilities to quantify perfusion [27].

In CASL, arterial blood water is continuously and selectively labelled as it passes through a labelling plane, typically applied at the base of the brain. The first perfusion method using ASL was introduced by Detre et al. in 1992 [29]. It employs a combination of repeated saturation in the neck region and imaging in a brain slice. This approach had been used earlier by Williams et al. [30], but for MR angiographic applications. This type of adiabatic inversion of the arterial magnetisation is realized using a 3 *secs* continuous RF pulse while applying a magnetic field gradient in the flow direction. The moving arterial spins will then experience a slow variation of the resonance frequency, which will result in their inversion [29]. Typically the thin inversion slab is selected at the level of the common carotid, and the spins in blood that flows through this plane will be inverted. When they reach the region of interest (imaging slab), the longitudinal magnetisation has decreased due to  $T_1$  relaxation, but it's still different from the relaxed tissue magnetisation [31]. So, the arterial blood reduces the total longitudinal magnetisation of the imaging slab. For the control experiment, two closely spaced inversion planes (double adiabatic inversion) are used: the magnetisation gets inverted while crossing the first plane and returns theoretically to its original state during the passage through the second plane [31]. This experiment is shown in Figure 3.6.

The PASL approach labels a thick slab (10 – 15 *cm*) of arterial blood at a single instance in time, and the imaging is performed after a time long enough for that spatially labelled blood to reach the tissue and exchange at the region of interest [27]. In 1994, Edelman et al. [32] proposed the first pulsed ASL scheme, known as echo planar imaging and signal targeting with alternating radiofrequency, EPISTAR. For the labelled image a single  $180^\circ$  RF pulse is applied in the presence of a field gradient to invert the longitudinal magnetisation of the protons in a slab inferior to the image slice (see Figure 3.7).

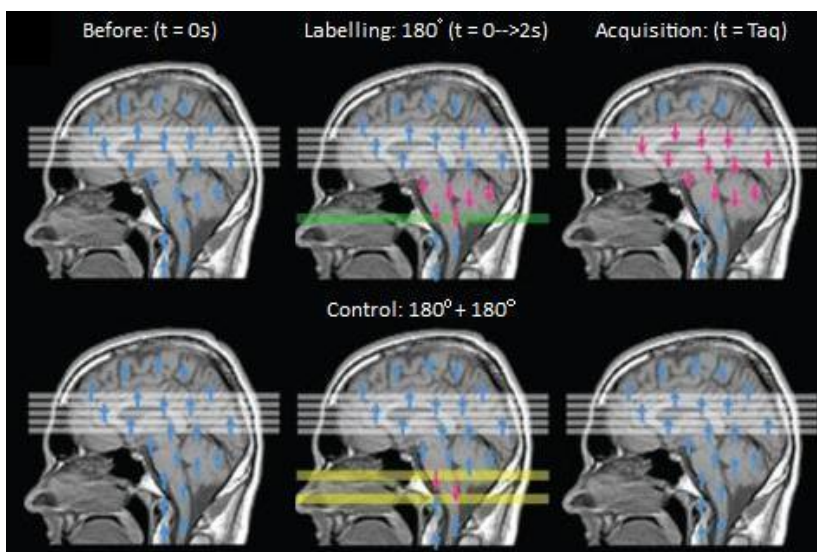


Figure 3.6: Continuous arterial spin labelling experiment (adapted from [7]).

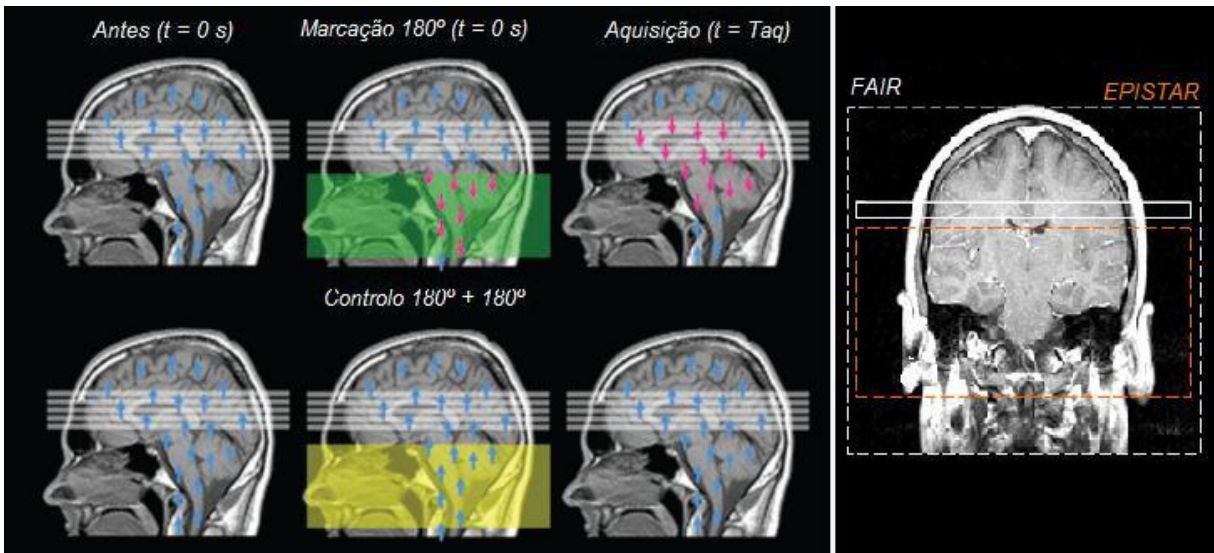


Figure 3.7: Pulsed arterial spin labelling experiment: (on the left) EPISTAR experiment and (on the right) localisation of labelling pulses used in EPISTAR and FAIR experiments (adapted from [7]).

For the control image two  $180^\circ + 180^\circ$  pulses of half the power are applied at the same proximal location [32]. Shortly afterwards, an alternative to this asymmetric method of labelling was proposed by Kwong et al. and Kim [33], who named it flow alternating inversion recovery (FAIR). In this approach, the label is symmetrically applied using a non-selective inversion pulse (Figure 3.7), while the control employs a concomitant slice selective gradient pulse. One third technique, named proximal inversion with a control for off-resonance effects (PICORE) was developed by Wong et al. [34], and uses a labelling scheme similar to EPISTAR. The only difference is that the inversion slab in the control acquisition was replaced by an RF pulse applied at the same frequency as in the label experiment but in the absence of a magnetic field gradient [34]. Furthermore, there's a wide range of labelling sequences available today, which are variants of these three principal techniques.

Comparing both spin labelling schemes, although CASL provides stronger perfusion contrast, it is more difficult to implement than PASL because of its hardware demands, and it deposits a higher level of RF power into the subject. The long labelling pulses in CASL also partially excite the imaging slices through an effect termed magnetisation transfer [27]. This has to be balanced during the control acquisitions, in order to accurately quantify CBF. PASL methods, on the other hand, require a gap between the image slice and the inversion slab to avoid imperfect slice profile effects [27].

### 3.4.2. Quantification

Accurate perfusion measurements require careful consideration of both data collection and analysis. To obtain a quantitative perfusion map from the difference image ( $\Delta M$ ), an accurate model of the system is required. The difference signal is dependent on a number of factors, including: inversion efficiency, blood  $T_1$ , tissue  $T_1$ , capillary permeability, arrival time and perfusion [17].

Figure 3.8 shows the tissue magnetisation  $\Delta M$  with time after the start of labelling at  $t = 0$ . As we can see, there are three parts of this curve: part 1 has no signal since the labelled protons have yet to reach the tissue volume; in part 2 the signal increases as labelled protons enter the volume; and in

part 3 the signal decreases due to longitudinal relaxation and outflow after the end of incoming arterial (labelled) blood [6].

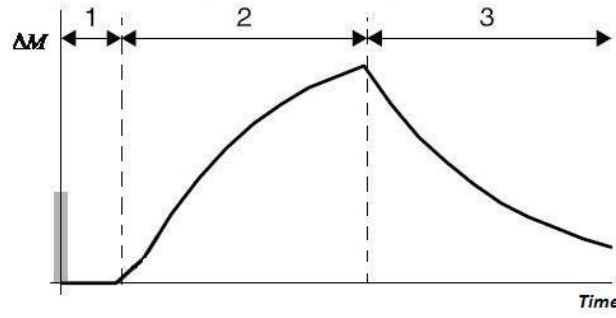


Figure 3.8: A schematic of the idealized magnetisation difference curve with time (adapted from [6]).

The perfusion curve describes the passage of the labelled spins through the vasculature into the tissues. Mathematically, it is possible to model the dynamics of the ASL signal considering that this signal comes from a bolus of labelled spins travelling through the vasculature, convolved with a tissue residue function [35]. CBF is then calculated using the deconvolution of the tissue curve  $C(t)$  by the measured arterial input function (AIF)  $C_a(t)$ :

$$C(t) = CBF C_a(t) \otimes R(t) = CBF \int_0^t C_a(t-\tau) R(\tau) d\tau \quad \text{Equation 3.2}$$

where  $R(t)$  is the residue function that describes the fraction of contrast that remains in the system after a given time  $t$ .

Buxton et al. [36] described a General Kinetic Model for the magnetisation difference between labelled and control measurements using the convolution integral from Equation 3.3:

$$\Delta M(t) = 2M_{0B} f \int_0^t c(\tau) r(t-\tau) m(t-\tau) d\tau \quad \text{Equation 3.3}$$

where  $M_{0B}$  is the equilibrium magnetisation of arterial blood,  $c(t)$  is the delivery function, and  $r(t-\tau)m(t-\tau)$  is the fraction of that magnetisation that remains at time  $t$ . Applying single-compartment kinetics in which each voxel is considered a single well mixed compartment, i.e., assuming instantaneous mixing between arterial blood and tissue [36], Equation 3.3 can be rewritten as Equation 3.4 for all PASL methods:

$$\Delta M(t) = \begin{cases} 0 & 0 < t < \delta t \\ 2M_{0B} f (t - \delta t) \alpha e^{-t/T_{1b}} q_p(T_{1b}, T_{1t}, T_{ex}, f, \lambda, t) & \delta t < t < \tau + \delta t \\ 2M_{0B} f \tau \alpha e^{-t/T_{1b}} q_p(T_{1b}, T_{1t}, T_{ex}, f, \lambda, t) & \tau + \delta t < t \end{cases} \quad \text{Equation 3.4}$$

with

$$q_p = \begin{cases} \frac{e^{kt} (e^{-k\delta t} - e^{-kt})}{k(t - \delta t)} & \delta t < t < \tau + \delta t \\ \frac{e^{kt} (e^{-k\delta t} - e^{-k(\tau + \delta t)})}{k(t - \delta t)} & \tau + \delta t < t \end{cases}$$

and

$$k = \frac{1}{T_{1b}} - \frac{1}{T_1} \quad \text{and} \quad \frac{1}{T_1'} = \frac{1}{T_1} + \frac{f}{\lambda}$$

where  $f$  is the CBF in ml-blood/ml-tissue/sec,  $T_{1b}$  and  $T_{1t}$  are the  $T_1$  of arterial blood and tissue, respectively,  $T_{ex}$  is the transit time from the distal edge of the tag region to the capillary bed where tagged blood water exchanges into brain parenchyma,  $\alpha$  is the inversion efficiency,  $\lambda$  is the blood-brain partition coefficient of water,  $\delta t$  is the arterial transit time and  $\tau$  is the time width of the label.  $q_p$  is a correction factor for the fact that the rate of decay of the tag switches from that of blood to that of tissue after exchanging into tissue, and for clearance of the tag by flow. Under most conditions  $q_p$  is close to unity [36].

As we can see, the raw difference signal  $\Delta M$ , although proportional to  $f$ , does not provide sufficient data to construct a perfusion map, primarily because  $\delta t$  and  $\tau$  are not known.  $M_{0B}$  and  $T_{1B}$  are spatially invariant constants that can be estimated either from imaging measurements or assumed from literature values and simply scale the perfusion measurement. The parameters  $\delta t$  and  $\tau$  are both dependent on vessel geometry and distribution of flow velocities [34]. Then, two modifications of the basic pulsed ASL experiment were introduced by Wong et al. [37] in order to eliminate the dependence of  $\Delta M$  on  $\delta t$  and  $\tau$ : QUIPSS (quantitative imaging of perfusion using a single subtraction) and QUIPSS II (second version of QUIPSS). Although they seem nearly identical in implementation, these modifications have very different properties, and can be combined with different labelling techniques [37].

The basic principle of these techniques is the application of a saturation pulse at time  $TI_1$  after the application of the tag to produce a well defined bolus of contrast. QUIPSS II is identical to QUIPSS, except that the saturation pulse is applied to the tagging region rather than the imaging slice [37]. In QUIPSS II, at time  $TI_1$  after the application of the tag, a saturation pulse is applied to the tagging region in both tag and control experiments, thus effectively cutting off the tail end of the inflowing tag. This delivers a bolus of tagged blood of time width  $TI_1$  to the imaging slice. After an additional delay, an image is acquired at time  $TI_2$ . Afterwards, Wen-Ming Luh et al. [38] developed a new approach called Q2TIPS (QUIPSS II with thin-slice  $TI_1$  periodic saturation), which improved the accuracy of perfusion measurements. In Q2TIPS, the QUIPSS II saturation pulse is replaced by a periodic train of thin-slice saturation pulses at the distal end of the tagged blood, which not only has sharper edges as also has a greater field homogeneity over the slice thickness than a thick-slice pulse [38].

According to this theory, if

$$TI_1 \leq \tau \quad \text{Equation 3.5}$$

$$TI_2 \geq TI_1 + \delta t \quad \text{Equation 3.6}$$

then the signal is independent of both  $\delta t$  and  $\tau$ , and is given by [37, 38]

$$\Delta M(TI_2) = 2M_{0B}fTI_1e^{-TI_2/T_{1b}}q(T_{1b}, T_{1t}, T_{ex}, f, \lambda, TI_2) \quad \text{Equation 3.7}$$

The condition on  $TI_1$  (Equation 3.5) is that it is shorter than the natural time width of the tagged bolus. If this is satisfied then the time width of the bolus is known to be  $TI_1$ . The condition on  $TI_2$  (Equation 3.6) is required to allow for the delivery of the entire bolus to the imaging slice [37]. If this is satisfied, then the CBF can be calculated from [39]

$$CBF = \frac{\lambda \Delta M}{2\alpha M_0 TI_1 e^{-TI_2/T_1 b}} \quad \text{Equation 3.8}$$

where  $M_0$  is the tissue magnetisation.

Nevertheless, there are several parameters that, if not accounted, can lead to significant errors in perfusion quantification.

### 3.4.2.1. The role of arterial transit time

Buxton et al. [36] demonstrated theoretically that one of the most important parameters needed for quantification of the ASL signal is the arterial transit time, which even in healthy subjects differs across the brain, being longest in distal branches. In most PASL approaches, information on perfusion is assessed at a single inversion time point  $TI_2$ , and therefore without information about the transit time. Sequences like QUIPSS II and Q2TIPS were developed to render ASL more transit-time insensitive. The usage of these modifications is really an advantage in volunteers and patients without vascular diseases where the difference in transit time is small, as well for quantitative functional studies where it is known that the transit time changes are small between baseline and activation conditions [37].

However, these methods will fail in patients with cerebrovascular diseases, where the transit time can be long in affected areas due to low perfusion velocity and, in some cases, extensive collateral perfusion. In these cases, the problem can be solved by acquiring images at multiple inversion times and therefore measuring the entire  $\Delta M$  curve (Figure 3.8) [5]. The standard sequences, in which a single time point is acquired at a time, are generally too lengthy to be suitable for clinical examinations. Günther et al. [40] introduced an elegant solution to this problem using a *Look-Locker-like* readout to measure the ASL signal at multiple  $TI_2$  in a single scan. A similar scheme was also implemented using the transfer insensitive labelling technique (TILT) by Hendrikse et al. [41].

### 3.4.2.2. Vascular artefacts

Vascular artefacts, associated with the inflow of labelled arterial blood into the arteries, can introduce important errors in CBF quantification. In a typical tissue voxel a range of many vessel sizes can be found (Figure 3.9), not all of which contain blood that will perfuse this tissue. The blood in the larger vessels is destined to perfuse tissue further downstream and so its signal must be removed.

To solve this problem, Ye et al. [42] proposed the use of bipolar crusher gradients to eliminate the signal from the large feeding arteries in CASL and PASL sequences. Another solution is to choose a sufficiently long inversion time, allowing the feeding vessels to empty before acquisition [42, 43].

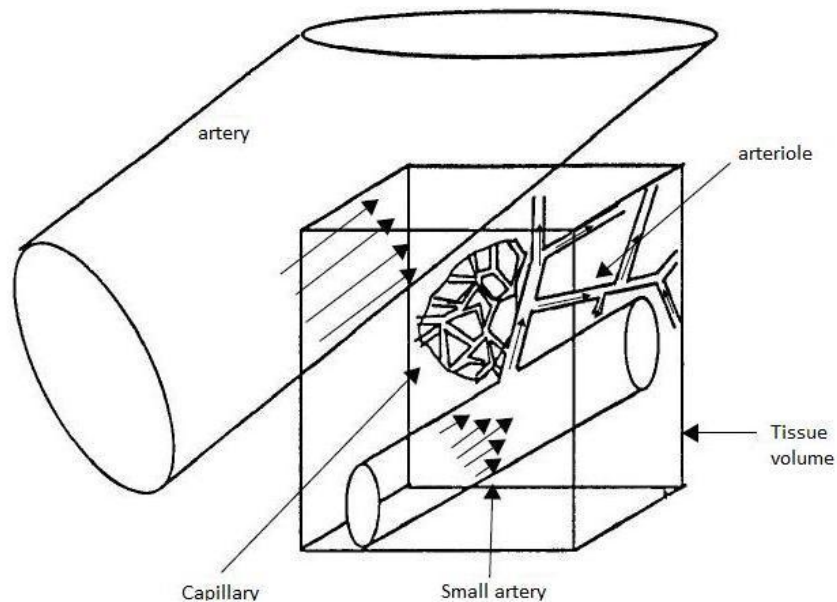


Figure 3.9: Vascular architecture showing the different vessel types that could pass through a typical tissue volume [6].

### 3.4.2.3. Inversion pulse shape and efficiency

In PASL sequences, where a spatially well defined label is used, the shape of the inversion pulse is of great importance. Ideally, the profile should be truly rectangular, allowing zero spacing between the labelling slab and the imaging region. However, this is not realizable due to finite duration of the RF pulse [27]. The imperfect profiles can reduce labelling efficiency, and there can be contamination in the imaging region from the labelling slab. So, a gap between the inversion and imaging slab is often introduced to avoid those problems, but as a result, transit times increase. In order to minimize this gap, adiabatic pulses specially designed for this type of labelling are used such as (see Figure 3.10): hyperbolic secant (HS), frequency offset corrected inversion (FOCI), or bandwidth-modulated adiabatic selective saturation and inversion (BASSI) [27].

For CASL approaches, the labelling is performed in general at a reasonable distance from the imaging slices, so the profile is less of a concern.

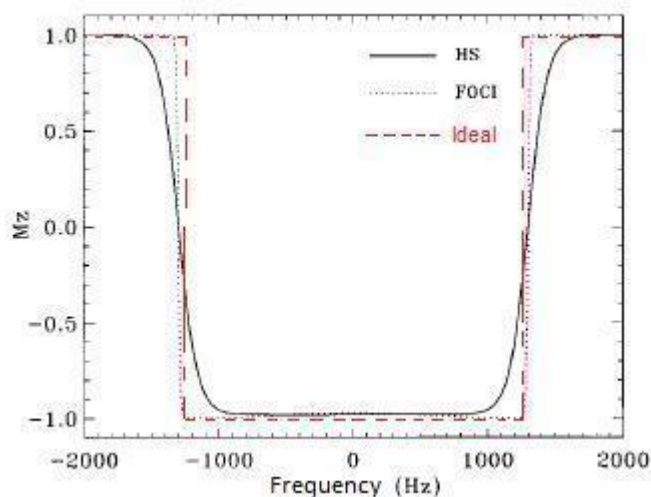


Figure 3.10: A comparison of inversion profiles a hyperbolic secant (HS) pulse, a frequency offset corrected inversion (FOCI) pulse, and the rectangular ideal pulse (adapted from [27]).

#### 3.4.2.4. Magnetisation transfer effects

As mentioned earlier, the labelling pulse can cause substantial magnetisation transfer (MT) effects in the static tissue of the image slice, particularly with CASL due to the long labelling. It is important that the control image has the same MT effects so that they will cancel on subtraction. Any difference in MT effects will produce an additional non-perfusion signal in the difference image, leading to inaccurate quantification [27].

#### 3.4.2.5. Signal to noise issues

At normal perfusion rates (between 40 and 100  $ml\ 100\ g^{-1}\ min^{-1}$ ), the signal change  $\Delta M$  is in the order 0.5 – 1.5% of the full signal [27]. Consequently, an average from typically 30 to 40 pairs of subtracted control and labelled images are required to get the desired SNR in the perfusion-weighted maps. A total scan time of 4 minutes is needed in order to acquire these data, which makes the technique very sensitive to motion artefacts. Proper head fixation and collaboration of the subject are necessary in order to obtain good results.

Fast imaging techniques like single shot EPI or spiral sequences are often used to reduce the scan time between successive control-label pairs as well overall scan time. Furthermore, prior saturation of the image plane reduces the sensitivity to motion [27].

#### 3.4.2.6. The role of blood equilibrium magnetisation

The inflowing blood has a proton density different from the tissue. For absolute quantification, the equilibrium magnetisation of the arterial blood  $M_{0B}$  is needed, i. e., the available longitudinal magnetisation from a fully relaxed blood filled voxel. To achieve this parameter, a common approach is to measure the equilibrium magnetisation in a grey matter or white matter region and estimate  $M_{0B}$  using the blood-brain partition coefficient ( $\lambda$ ) [44]. For single inversion time experiments, this is often done in a voxel by voxel basis using the control experiment as tissue magnetisation maps  $M_0$  [27].

It is important to note that  $M_{0B}$  is a direct scaling factor of the perfusion (see Equation 3.8) and therefore an error in the estimation of it will directly change the calculated CBF value.

#### 3.4.3. Clinical and Research applications

ASL techniques are unable to provide measurements of blood volume and mean tissue transit time, which could be of clinical use. However, they have been used in numerous applications, ranging from basic neuroscience using animal models and human volunteers to clinical perfusion measurement in pathologies such as stroke and brain tumours [28, 41, 45]. As long as the same procedure and parameters are consistently used, reproducible results can be achieved using ASL [4,



6]. Despite the problems related to the quantification of perfusion using ASL, most clinical decisions can be based on relative differences in CBF rather than absolute measures, which could render this method useful in the daily clinical practice.

Although the majority of ASL perfusion research has been carried out in the brain, other organs including kidney [46] and lungs [47], have gained attention for measuring perfusion. Improved techniques and hardware available, in particular the move toward 3 T high field scanners in the standard clinical environments, seems to push this method from the research and development stage headed for clinical applications.

### 3.5. Comparison between BOLD and ASL measurements

BOLD contrast is the most commonly used fMRI method for studies of brain activity. However, there are some potential problems with the commonly applied technique in these applications. One of them is that the signal change can vary substantially between subjects and across sessions, for reasons that are poorly understood [23]. Moreover, the underlying physiological processes associated to BOLD signal changes, which includes a complex interaction of CBF, CBV and  $CMRO_2$ , make changes in the BOLD signal difficult to interpret [24]. Direct CBF measurements using ASL had provided an attractive alternative. Because perfusion methods directly measure the amount of arterial blood that has been delivered to the capillary bed, the functional CBF signal may be more localised to the sites of neuronal activation than the BOLD signal, which derives primarily from blood oxygenation changes in the draining venules and veins proximal to the activated tissues [17, 24, 39].

A powerful feature of ASL techniques for fMRI is that they can be used to simultaneously acquire quantitative perfusion data and BOLD contrast data. If a sufficiently long TE is used for image acquisition, then BOLD contrast is present in the image series [27]. In fact, from a series of ASL images acquired with alternating control and labelling, perfusion and BOLD signals can be obtained by subtracting or adding the control and labelled images, respectively, in the same data sets. Recent studies have compared BOLD with CBF measurement using this non-optimised BOLD acquired simultaneously with the ASL technique. Such reports suggest that CBF measurement provides improved sensitivity relative to BOLD particularly for low-frequency tasks and is associated with lower inter-subject variability [39]. As a consequence, it has also been found that CBF measurements provide a more useful approach when assessing longitudinal activation changes [4].

In conclusion, simultaneous acquisition of ASL and BOLD data provides several advantages for fMRI studies, including efficient acquisition of two functional images and minimization of temporal and spatial variations in the two signals. As ASL methods have become increasingly sophisticated, they have become increasingly useful in studies of brain-behaviour relationships in health and disease, ensuring a good complementary technique for BOLD contrast to measure neuronal activity during behavioural challenge tasks. In particular, the pre-surgical mapping of eloquent tissue can now be performed using combined ASL-BOLD techniques.



## Chapter 4

### Materials and Methods

#### 4.1. Subjects

Fifteen adult volunteers (six females, mean age 25.6, range 22-51 years) participated in this study. Participants were selected without regard to ethnicity or race or any other criteria. All subjects were right handed and none of them had a history of major medical, psychiatric or neurological disorders. The experiments were not carried out in the same day neither in the same period of the day, and with no control of subject's state.

This study was approved by the local ethical committee, and written informed consent was obtained from all volunteers.

#### 4.2. MR scanning

Imaging was performed using a 3 Tesla Magnetom Verio MRI system from Siemens in *Hospital da Luz* Imaging Department.

All subjects participated in a functional imaging session that involved one functional protocol for BOLD and two functional protocols for ASL, in which two different experiments were conducted: protocol #1 and protocol #2. The fMRI sessions included the acquisition of a high-resolution anatomical image using a 3D T1-weighted sequence (Magnetization Prepared Rapid Acquisition Gradient Echo, MP-RAGE), providing 160 sagittal slices with 1.0 mm of thickness, 256 x 240 mm<sup>2</sup> field of view (FOV) and a matrix size of 256 x 240, yielding an isotropic spatial resolution of 1 mm<sup>3</sup>. Further scan parameters were: TR = 2250 ms, TE = 2.26 ms, an inversion time (TI) of 900 ms and a flip angle of 90°.

It is important to report that the imaging sessions of some volunteers were split in two parts which were conducted in different days: a first part where the BOLD and the first ASL protocols were conducted and a second part where the second ASL protocol was performed.

##### 4.2.1. BOLD fMRI

The BOLD protocol used a block design consisting on 4 cycles of 30 sec of rest (OFF) and 30 sec of motor task (ON), resulting in a total acquisition time of 240 sec (4 minutes). The motor activity consisted on a finger tapping task, by sequential thumb-digit opposition (as shown in Figure 4.1).

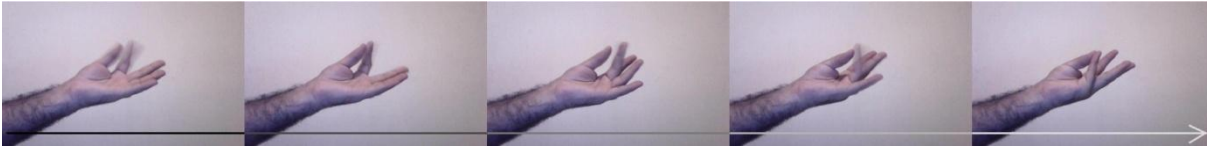


Figure 4.1: Motor task performed by all volunteers: from left to right sequence of images illustrating the movement of the motor task.

Functional images were acquired using a multi-slice single-shot gradient-echo (GRE) echo-planar imaging (EPI) sequence. The whole brain was covered with 37 contiguous axial slices of 3 mm thickness, positioned parallel to the anterior-posterior commissure (AC-PC), as shown in Figure 4.2 a). Eighty dynamic volumes were collected for each functional scan. The other imaging parameters were as follows: TR = 3 sec, TE = 30 ms, flip angle = 90°, FOV = 256 x 256 mm<sup>2</sup> and a matrix size of 64 x 64, yielding a resolution of 4 x 4 x 3 mm<sup>3</sup>. The slice acquisition order was ascending, interleaved. The sequence has been driven in 3D PACE mode (Siemens Erlangen) enabling prospective motion correction.

Prior to the functional scanning, a B<sub>0</sub> field map was acquired for the same slice prescription as the one to be used for the BOLD acquisition. The field maps are based on gradient echo sequences and allow the measurement of the main magnetic field (B<sub>0</sub> field). They can then be used to explain the susceptibility artefacts observed in EPI, namely geometric distortions and signal loss. The former can at least partially be corrected for. The latter can only be indicated, to allow more accurate interpretation of the results.

It is important to refer that this BOLD protocol is the one used in clinical applications at *Hospital da Luz*, which has been used extensively by neuroradiologists with satisfactory results.

#### 4.2.2. ASL fMRI

The ASL application package commercially available by Siemens consists of a sequence with pulsed arterial spin labelling for perfusion-weighted imaging. This sequence comprehends three different labelling schemes:

1. PICORE Q2TIPS using FOCI pulses;
2. FAIR QUIPSS II using HS pulses;
3. PICORE QUIPSS II using BASSI pulses.

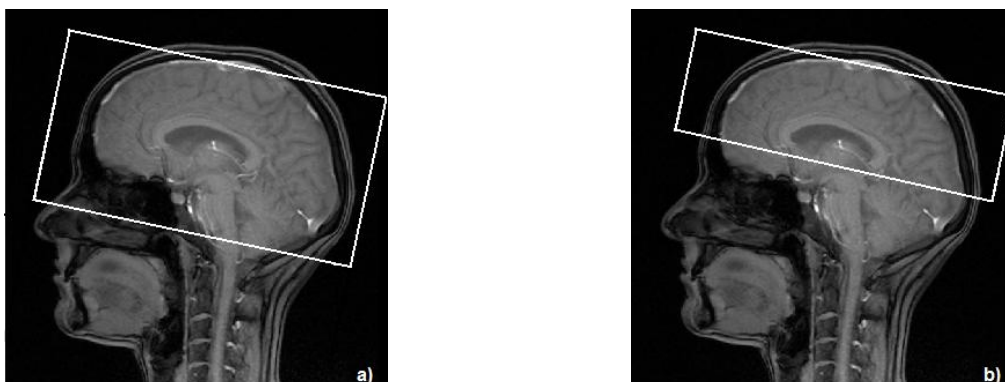


Figure 4.2: Illustration of a typical prescription of the imaging slab positions for a) BOLD and b) ASL experiments, from sagittal scout scan.

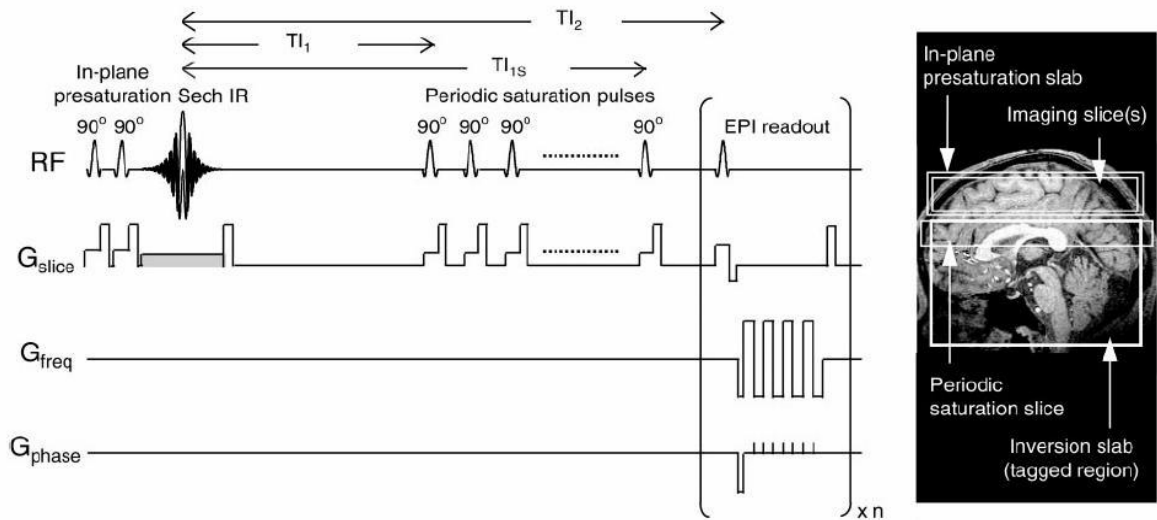


Figure 4.3: Pulse sequence used for Q2TIPS ASL imaging. On the right the locations of the in-plane pre-saturation slab, imaging slice(s), periodic saturation slice, and inversion slab used in the PICORE labelling scheme are shown [38].

The method used in this work was the scheme 1 and it has been described by Luh et al. [38], and is illustrated in Figure 4.3. In this method two  $90^\circ$  RF pulses (*sinc* modulation, 25 ms duration) are applied to pre-saturate the imaging region. Next, a  $180^\circ$  inversion pulse (FOCI modulation) is applied to label the arterial spins over a 10cm thick labelling region. The first inversion time  $TI_1$  allows the inverted arterial spins to flow to the imaging slab. Between  $TI_1$  and  $TI_{1s}$  ( $TI_1$  stop time)  $90^\circ$  saturation pulses (*sinc* modulation, 20 ms duration) are repeatedly applied over a 20 mm thick saturation slab, in order to define the time width of the bolus. Image acquisition is carried out at  $TI_2$  using a GRE-EPI readout module. In the control measurement, the inversion pulse is applied off-resonance, with a symmetrical frequency relative to the imaging region, such that that no inversion occurs in the labelling slab but the same off-resonance effects are present in the imaging slices. The off-resonance effects should therefore be cancelled out on the difference image between control and tag.

Two different protocols for functional studies with ASL have been conducted. The parameters of both experiments are described next.

#### 4.2.2.1. ASL protocol #1

This primary ASL protocol consisted on the acquisition of one perfusion scan during rest and another one during an equal period of motor activation, resulting in a total acquisition of approximately 8 minutes. A total of 91 interleaved tag and control volumes were acquired (for each perfusion scan). The PASL parameters were as follows:  $TI_1 = 700$  ms,  $TI_{1s} = 1600$  ms,  $TI_2 = 1800$  ms,  $TR/TE = 2500/11$  ms and flip angle =  $90^\circ$ . The imaging region consisted of 9 contiguous axial slices of 8 mm thickness positioned parallel to the AC-PC axis, between the vertex of the brain to the top of cerebellum (as shown in Figure 4.2 b)). The imaging slab had a  $FOV = 256 \times 256$  mm<sup>2</sup> and a matrix size of  $64 \times 64$ , yielding a resolution of  $4 \times 4 \times 8$  mm<sup>3</sup>, and the gap between the labelling slab and the proximal slice was 18.8 mm. The slices were acquired in ascending order.

The sequence was also been driven in 3D PACE mode (Siemens, Erlangen) enabling prospective motion correction.

#### 4.2.2.2. ASL protocol #2

For functional studies, the previous protocol was changed to a new protocol, where not only the functional paradigm was modified, but also some acquisition parameters were optimized. This new experiment consisted on a blocked design with 5 cycles of OFF blocks (25 sec each) alternated with 5 ON blocks (25 sec each). A total of 101 volumes alternating between tag and control were acquired, resulting in a total scan of 4 min 12.5 sec.

In order to find the optimal TE value for ASL functional measurements, a pilot test was performed using three different TE values: 11 ms, 20 ms and 30 ms. The value TE = 11 ms was chosen, because it optimized the ASL functional changes, while still allowing for simultaneous BOLD contrast in the same scan. The parameters chosen for ASL functional protocol #2 were the same as protocol #1, except for: TR/TE = 2500/11 ms, 9 contiguous axial slices of 6 mm thickness parallel to the AC-PC line (the imaging slab was positioned as shown in Figure 4.2 b), with a FOV = 224 x 224 mm<sup>2</sup> yielding a resolution of 3.5 x 3.5 x 6 mm<sup>3</sup>.

Prior to the functional scanning, a field map with the same slice prescription as the one used for the PASL scan was acquired.

Functional data acquisition parameters for the three protocols described early are resumed in Table 4.1.

Table 4.1  
Functional data acquisition parameters

Prot.	EPI readout				Tagging Sequence: PICORE Q2TIPS									
	TR (ms)	TE (ms)	FA	No. vols.	No. slices	Slice thick (mm)	Matrix size	FOV (mm <sup>2</sup> )	T11 (ms)	T11s (ms)	T12 (ms)	Inv. slab thicknes	Gap (cm)	T <sub>aq.</sub> (min)
<b>BOLD</b>	3000	30	90°	80	37	3	64 x 64	256 x 256	-----	-----	-----	-----	-----	4:00
<b>ASL #1</b>	2500	25	90°	91+91	9	8	64 x 64	256 x 256	700	1600	1800	1 cm	1.88	7:35
<b>ASL #2</b>	2500	11	90°	101	9	6	64 x 64	224 x 224	700	1600	1800	1 cm	1.88	4:13

### 4.3. Image analysis

Image processing and analysis were carried out with Siemens *Syngo MR* software (task cards *Viewer, 3D and Neuro 3D*), a software from the Oxford University Centre for Functional MRI of the brain (FMRIB) called FSL (FMRIB's Software Library) [48], and self-written MATLAB (The Mathworks, Natick, MA, USA) and Linux shell script routines.

Syngo Neuro 3D is a highly intuitive user interface software that simplifies and improve workflows in clinical routine. Statistical analysis of the functional data is performed by fitting a general linear model (GLM) to the BOLD data. The final result of this analysis is a t-map called “Eva-Series – GLM” that contains the activation clusters: its lower and upper limits can be tailored manually with the Neuro 3D task card.

FSL is a powerful software that includes a comprehensive library of analysis tools for fMRI, MRI and DTI brain imaging data [49]. Some of these tools can be run both from the command line and as graphical user interfaces (GUI). For functional data analysis, the fMRI Expert Analysis Tool (FEAT) was used. FEAT is part of FSL and has a complete toolbox for high quality fMRI data analysis. This software tool carries out data preprocessing, including slice timing correction, motion correction with MCFLIRT (Motion Correction FMRIB’s Linear Image Registration Tool) and fieldmap-based EPI-distortion correction with FUGUE (FMRIB's Utility for Geometrically Unwarping EPis). The data modeling which FEAT uses is based on the GLM. It allows the description of the experimental design and then a model is created that should fit the data showing where the brain has activated in response to the stimuli. The GLM is then fitted to the time-series data using FILM (FMRIB's Improved Linear Model), a robust and accurate nonparametric estimation algorithm, with autocorrelation correction by prewhitening; this gives improved estimation efficiency compared with methods that do not prewhiten. The following tools from FSL have also been used: BET (Brain Extraction Tool) to delete non-brain tissue from an image of the whole head, FAST (FMRIB’s Automated Segmentation Tool) to perform segmentation of the brain into different tissue types (grey matter, white matter and CSF), FLIRT (FMRIB’s Linear Image Registration Tool) to perform linear image registration, and FSL View to display 3D and 4D data and prescribe imaging ROI’s. Furthermore, a set of useful command-line utilities called FSLUTILS has also been used to allow the conversion and manipulation of the images [25, 49].

It is important to note that Syngo MR works with DICOM (Digital Imaging and Communications in Medicine) format images, and that FSL uses NifTI-1 (Neuroimaging Informatics Technology Initiative) data format by default. For that matter, *MRIConvert* has been used to perform the conversion from DICOM to NifTI FSL format.

### 4.3.1. Field map-based EPI distortion correction

It is possible to measure the field inhomogeneities across an imaging scan with a fieldmap sequence. These measured field values can be used to calculate the geometric distortion and signal loss, and then to use the calculate information to compensate for these artifacts. The aim of this approach was to compare the main applications of both FSL and Neuro 3D task card Syngo software with the field map image.

The Syngo software simply loads the fieldmap and overlays it to the functional t-map: the user is then able to identify regions of severe susceptibility /strong  $B_0$  inhomogeneity) artifacts and can chose to ignore the results obtained in those regions. The threshold for the region exclusion based

on the severity of the artifacts can be adjusted manually by the user, according to how strict the analysis should be.

In FSL, the fieldmap is further used to actually correct the geometric distortions present in the EPI data due to the susceptibility artifacts. A GUI interface exists for applying FUGUE as part of the FEAT pre-processing options (see Figure 4.4). This implementation of FUGUE uses a measured field map to unwarp distorted images by performing pixel shifts in the phase-encode direction. In the GUI, the two images that are required are: a real fieldmap image which must have units of rad/s, and a brain-extracted and registered magnitude image. Next it also needs the Effective EPI echo spacing (in ms), which is the time between echoes in successive k-space lines, the EPI echo time (also in ms), and the Unwarp direction, which is the phase-encoding direction of fMRI EPI data. To further understand what kind of processing has been done here is important to know how these fieldmap images are acquired. Unfortunately, there is no standard sequence for fieldmap acquisitions and different scanners return different images. The most common sequences acquire two images with different echo times. The change in MR phase from one image to the other is proportional to both the field inhomogeneity in that voxel and the echo time difference. The field value is therefore given by the difference in phase between these two images divided by the echo time difference. As the phase is of great importance in fieldmapping, but is normally not saved in other sequences, these images are often quite different from the standard images.

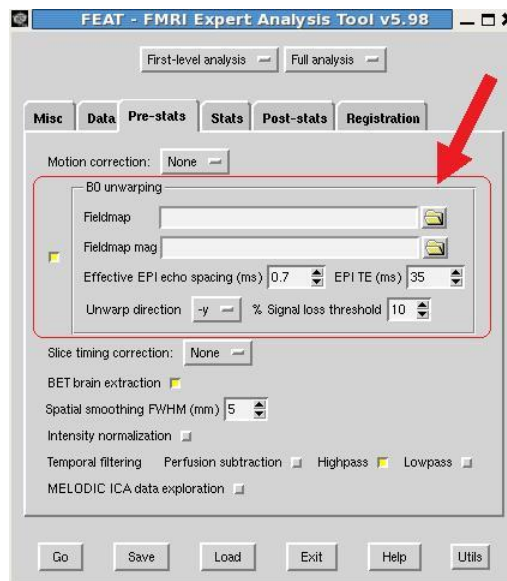


Figure 4.4: Layout of GUI interface for FUGUE (part of FEAT), for applying EPI distortion correction.

Since each scanner can give different data, the first step in practice was to find what kind of fieldmap acquisition data the scanner gives. Using *fslinfo* and consulting the DICOM header of these images, it was determined that the type of the fieldmap images was one single image: the result of the subtraction between phase images. So this image hadn't been reconstructed fully into a fieldmap yet. For that, it was necessary to follow some pre-processing steps. As we only have the subtracted phase image, we needed to get a magnitude image that is undistorted and registered with this phase image. This has been made registering the brain extracted from the structural image from the high



resolution space to the fieldmap space based in their qforms and sforms (those matrixes give the locations of the voxels centers in the  $(x, y, z)$  coordinate system). After we check that the magnitude image and the subtracted phase image have the same resolution, we convert the phase image to radians, tapping the follow command:

```
fslmaths phase_image -mul 3.14159 -div 2048 phase_rad -odt float
```

The value 2048 is the maximum intensity in the integer format of the raw images. Then we used PRELUDE (Phase Region Expanding Labeller for Unwrapping Discrete Estimates) to do the required phase unwrapping:

```
prelude -a fieldmap_mag -p phase_rad -o phase_unwrap_rad
```

Finally, to get the real fieldmap in rad/s we did:

```
fslmaths phase_unwrap -mul 1000 -div TE fieldmap_rads -odt float
```

where TE was replaced with the appropriate difference in echo times. In this case TE = 7.38 ms. The Effective EPI echo spacing used was 0.7 ms, and the phase-encoding direction (unwarp direction) selected was  $-y$ .

This approach was performed for all subject's data for BOLD protocol and ASL functional protocol #2 (since in ASL protocol #1 it hadn't been acquired a fieldmap image).

### 4.3.2. Functional data

Analysis of functional data was carried out with both FSL and Neuro 3D task card Syngo software. This latter automatically produces a t-map using a GLM approach, based on the indication by the user of the baseline and activation periods throughout the experiment. However, during this study, this GLM approach couldn't be applied for ASL functional data, because the functional analysis utility was disabled for the ASL sequence. In terms of perfusion analysis, the Neuro 3D task card Syngo software performed the pairwise control/tag subtraction and subsequent perfusion calculation. The output is therefore a perfusion weighted map (arbitrary units) and a quantitative relCBF map (ml/min/100ml). For the first protocol, we have two quantitative relCBF maps: one corresponds to the rest state, and the other corresponds to the motor activation. The difference between these two maps was computed, and then fused with BOLD information in order to achieve a better comparison between both results. The steps for this procedure involved not only Neuro 3D task card, but also the Viewer and 3D task cards within Syngo software, and are resumed in Appendix A A.1.

In FSL, analysis of functional data was performed using FEAT Version 5.98 [25]. For these analyses, motion corrected (PACE) time-series were used. The following pre-statistics processing steps were applied to all datasets: non-brain removal using BET, spatial smoothing using a Gaussian kernel of full width at half maximum (FWHM) 5 mm, and high-pass temporal filtering ( $\sigma = 20$  sec). Time-series statistical analysis was performed using FILM with local autocorrelation correction. The definition of the stimulus conditions in this tool was different for the three functional protocols.

For the BOLD protocol, one stimulus condition was defined, using one EV (explanatory variable), according to the stimulation paradigm applied, i.e., 30 s OFF and 30 s ON. This block pattern was convolved with a gamma function with Stddev of 3 s and mean lag of 6 s (default values), which models the hemodynamic response function (HRF) (see Figure 4.5).

For ASL protocol #2 the data needed specific processing because each voxel's time-series alternates between "tag" and "control" conditions. So, 3 EV's were setup: EV1 to model the alternation between control and tag conditions, EV2 to model the alternation between periods of activation and rest, similar to the one described for BOLD protocol, and EV3 is the interaction between EVs 1 and 2, to model the activation component of the control-tag signal (see Figure 4.5). This last explanatory variable reflects the expected response from an ASL functional study. In summary, the EV1 was defined with a pattern of 2.5 s OFF and 2.5 s ON, since the TR of the acquisition sequence was 2.5 s. The EV2 was defined according to the stimulation paradigm applied: 25 s OFF and 25 s ON. This pattern of 25 s ON and 25 s OFF was convolved with a gamma function with Stddev of 3 s and mean lag of 6 s (similar to the BOLD analysis). Finally, the EV3 was simply defined by the interaction between the last two EVs (which can be made automatically by FEAT). For this approach, it's important to note that the tag-control order of the data must be known.

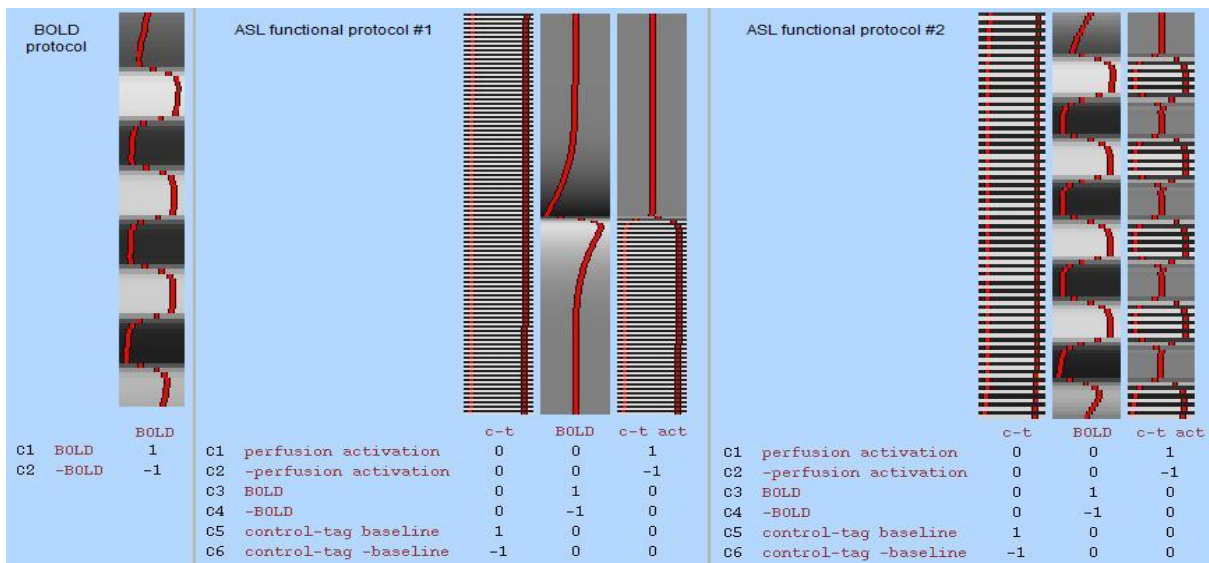


Figure 4.5: Design matrixes for the three functional protocols performed with FEAT. For each EV of each protocol, two contrasts were considered (C1 and C2, C3 and C4, and C5 and C6) where one is the symmetric of the other. In practice, only the first contrast of each EV has been considered.

In order to analyse the data from ASL protocol #1 using a similar approach in FSL, we had to concatenate the rest and activation scans, in order to have one single time-series data. We eliminated the first volume of each time-series, so that this procedure results in one single time-series dataset with 180 volumes, which the first 90 volumes corresponding to the rest state and the other 90 volumes corresponding to the activation state. Then we were able to define the 3 EV's. EV1 and EV3 were equally defined. EV2 was defined with 225 s OFF and 225 s ON pattern, convolved with a gamma function with the same parameters defined for the other two protocols (see Figure 4.5).

By fitting of the GLM to the data, the parameter estimates (PE) corresponding to each EV are determined and the pre-defined contrasts (COPE) are computed. A t test is then applied to each COPE, resulting in a Z (Gaussianised T/F) statistic map for each contrast. The Z maps were thresholded using a clustering procedure, whereby each cluster is determined by a voxel  $Z > 2.5$  and a (correct) cluster significance threshold of  $P = 0.05$  for all data sets.

For BOLD data, registration of the functional images to the corresponding individual high-resolution T1-weighted structural images and the MNI (Montreal Neurological Institute) standard brain was carried out using FLIRT with 7 and 12 degrees of freedom (DOF), respectively. For ASL functional data, we first registered the functional images to an equivalent EPI image but covering the whole-brain (acquired during the same session from the subject), using FLIRT 3 DOF, before further transformation to the high-resolution T1-weighted structural and MNI standard brain.

### 4.3.3. Segmentation of structural data

The segmentation was performed using the FAST tool, part of FSL [25]. To do this, first we registered the  $T_1$  high resolution image to the perfusion images using FLIRT, in order to have a structural image with higher definition and without signal distortion and loss in ASL space. Then, FAST was used to segment this structural image of each subject into grey matter (GM), white matter (WM) and CSF. The output images created for each subject were: a partial volume map, which is a non-binary partial volume image for each class, where each voxel contains a value in the range of 0-1 that represents the proportion of that class's tissue present in that voxel, and a binary segmentation image per class. These images were needed for CBF quantification, and were also used in the subsequent computation of CBF analysis and in obtaining subject specific masks.

## 4.4. Data analysis

The data analysis consisted in approaches developed for specific tests in order to evaluate the results given from each functional protocol, to look at some abilities of ASL protocols and to explore some properties of ASL data analyses in FSL. The statistical analyses were performed by means of the MATLAB software and the Statistical Package for the Social Sciences (SPSS) Version 17.0. For all statistical tests described below, significance was accepted if  $p < 0.05$ .

### 4.4.1. Variability and Localisation of motor activation

To define the location of motor activation, only BOLD protocol (currently used in clinical applications) and ASL functional protocol #2 have been considered. This study was performed to evaluate the extent of motor activation areas given by the two experiments. Although the TE is short and not optimized for BOLD contrast in ASL protocol #2 (TE = 11 ms), this contrast was additionally used in this study for the comparison between both protocols. It provides an additional measure

within the same setup. In summary, we are comparing here two protocols by means of three different approaches:

- BOLD: the BOLD contrast from BOLD protocol;
- BOLD<sub>ASL</sub>: the BOLD contrast from ASL protocol #2;
- CBF: functional CBF contrast from ASL protocol #2.

The activation clusters given by each experiment of each subject were registered to the MNI standard brain using FLIRT from FSL to perform an inter-subject comparison and a group analysis. For calculation of the location of activation, it has been proposed using the cluster’s centre of gravity (COG) measurement technique which is the weighted (by signal change) location of the centre of activation within a cluster volume of neighbouring voxels that are significantly activated.

To test if BOLD, BOLD<sub>ASL</sub> and CBF activation areas co-localise, the displacement of the location of activation from BOLD, BOLD<sub>ASL</sub> and CBF in each subject was calculated in terms of the Euclidean distance between the Cartesian coordinates  $(x, y, z)$  from the COG measurement within the MNI standard space. The mean displacement across the group was calculated for each experiment. The hand primary motor cortex (HMC) of left hemisphere was used as reference to measure the relative displacement and distance for each experiment. For the localisation of HMC, the knob-like structure of the precentral gyrus that most often contain a motor hand function was considered [10]. This segment is shaped like an omega in the axial plane and like a hook in the sagittal plane. Nine points (three medial points M1, M2 and M3, three lateral points L1, L2 and L3, and three central points CM, CL and CC) under the omega shaped segment of MNI standard brain were drawn by a neuroradiologist, and two mean points were calculated: C1 which is the mean point of the three central points, and C2 which is the mean point of all nine points (as shown in Figure 4.6). The rationale of this approach was to determine which BOLD, BOLD<sub>ASL</sub> or CBF activations is closer to HMC. The displacement with respect to the HMC and the Euclidean distance were calculated for each subject for each experiment. Euclidean distance between generic points A and B was defined as:

$$D_{A-B} = \sqrt{(x_A - x_B)^2 + (y_A - y_B)^2 + (z_A - z_B)^2} \tag{Equation 4.1}$$

where  $x_i$ ,  $y_i$  and  $z_i$  are the coordinates of point  $i$ . The group mean Euclidean distance between BOLD, BOLD<sub>ASL</sub> and CBF activation was compared using an Analysis of Variance (ANOVA).

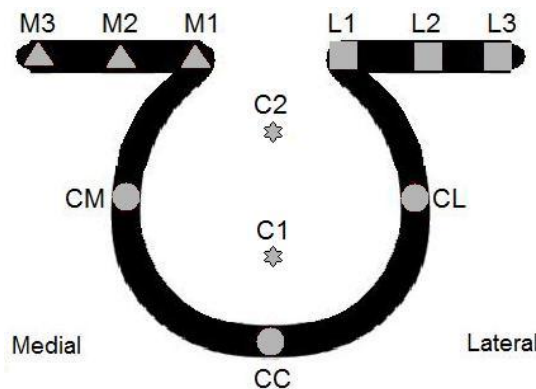


Figure 4.6: Localisation of the hand primary motor cortex: 3 medial points  $\blacktriangle$ (M3, M2 and M1), 3 lateral points  $\blacksquare$ (L1, L2, L3), 3 central points  $\bullet$ (CC, CM and CL), and two mean points  $\star$ (C1 and C2).

To compare the inter-subject extent of activation areas, for each experiment and for each coordinate, the variance of activation COGs between all subjects was calculated ( $Var = \sum(x_i - x_{avg})^2 / (N - 1)$ , with  $N = 15$  subjects). In addition, three inter-subject activation maps were computed: for each experiment the COGs and the local maxima location of the activation clusters of all subjects were displayed in order to illustrate the common area of overlap and to qualitatively compare the extent of activation between BOLD, BOLD<sub>ASL</sub> and CBF.

#### 4.4.2. CBF quantification methods

In the Q2TIPS PASL sequence used in this work, as previous mentioned, bolus width  $TI_1$  is well defined and can be set by the user. The ASL difference signal between labelled and control images ( $\Delta M$ ) can then be made minimally sensitive to the transit delay  $\delta t$  by setting the image acquisition time  $TI_2 \geq TI_1 + \delta t$ . In this case, quantitative perfusion maps can be obtained by computing the CBF in each pixel using the equation [39]:

$$CBF = \frac{\lambda \Delta M}{2\alpha M_0 TI_1 e^{-TI_2/T_{1b}}} \quad \text{Equation 4.2}$$

Table 4.2 displays the values used for perfusion quantification parameters.

Table 4.2  
Perfusion quantification parameters used to calculate CBF ( $\alpha$ ,  $\lambda$  and  $T_{1b}$  were consulted in [27, 50])

$\alpha$	$\lambda$	$TI_1$	$TI_2$	$T_{1b}$
90 %	0.9 ml/g	700 ms	1800 ms	1500 ms

The equilibrium magnetization of the tissue,  $M_0$ , was determined considering the average of the control volumes from each subject ASL data sets. The averaged image was then masked with the GM binary mask from FAST (obviously registered to ASL space). To account for the slice acquisition ordering effects and to avoid introducing noise in the perfusion maps, we calculate the signal mean for each slice, i.e., for each slice of a specific volume there is a single mean value.

For this single TI quantification, three different approaches were explored in order to obtain more accurate CBF values and study the variances between the values given by each approach:

- *Method 1*: In this method we applied Equation 4.2, with the values expressed in Table 4.2 for the whole volume.

- *Method 2*: In this second method we applied Equation 4.2, with the values expressed in Table 4.2 for the whole volume, but with correction of slice readout timing,  $TI_2$ . The slices of a specific volume are not acquired simultaneously, i.e., the first slice is acquired in a certain time  $t_1$ , but the second slice is acquired in a time  $t_1 + \Delta t$  (since the slice acquisition is performed in the ascending order). This causes a error in the estimation of perfusion, which is

especially significant for the upper slices. So, we use the information of slice acquisition time (from the DICOM header) to correct this slice acquisition timing effect.

- *Method 3*: In this last method we used the same equation but with the correction factor  $q_p$ :

$$CBF = \frac{\lambda \Delta M}{2\alpha M_0 T_{1b} q_p e^{-T_{12}/T_{1b}}} \quad \text{Equation 4.3}$$

$q_p$  is the correction factor that accounts for the difference between the  $T_1$  of blood and the  $T_1$  of brain tissue [36], and is expressed by:

$$q_p = \frac{e^{kt} (e^{-k\delta t} - e^{-k(\tau+\delta t)})}{k(t-\delta t)}$$

with

$$k = \frac{1}{T_{1b}} - \frac{1}{T_1} \quad \text{and} \quad \frac{1}{T_1'} = \frac{1}{T_1} + \frac{f}{\lambda}$$

To apply Equation 4.3 we had to do several approaches. Since this is a non-linear equation we approximated  $1/T_1' = 1/T_1 + f/\lambda$  to  $1/T_1' \approx 1/T_1$ . A typical human CBF of  $60 \text{ ml}/100\text{g}/\text{min}$  corresponds to  $f = 0.01 \text{ s}^{-1}$ , and with  $\lambda = 0.9$  and  $T_1$  of approximately 1 s, the difference between  $T_1'$  and  $T_1$  is only approximately 1%. That's the error that we are committing in this approximation. The transit time  $\delta t$  could be calculated experimentally as mentioned before, but not with this sequence/protocol. So, we had to estimate this parameter. Wong et al. [17] have determined experimentally that this transit delay ranges from about 500 – 1500 ms for a physical gap of 1 – 3 cm between the tag region and the imaging slice. Then, the linear relation  $\delta t(z) = 500z$  was assumed. This expression allows estimating the transit time  $\delta t$  (in ms) at a slice distance  $z$  from the tag region (in cm), and reflects that the transit delay of blood is 500 ms per cm of distance travelled. In this approach we also used the information of slice acquisition time (from the DICOM header) to correct the slice acquisition timing effect. The value of  $T_1$  used was 1200 ms [50].

In order to detect statistically significant differences between CBF values provided by each approach, t-tests were performed. To allow a more complete comparison between them, the mean value of each slice for all volumes was calculated from each of the three maps obtained.

To generate the quantitative perfusion maps by these three methods, a shell script routine in Linux with some FSL command utilities has been developed (see Appendix A A.2).

#### 4.4.3. CBF quantification in Rest and Activation conditions

The difference on CBF values between the condition of rest and the condition of activation was assessed using both ASL functional protocols. For ASL protocol #1, quantitative perfusion maps for rest and activation were easily performed, since we had two different images corresponding to both

conditions. For ASL protocol #2, first we had to concatenate the images of the 5 blocks in rest and images of the 5 five blocks in activation, in order to produce also two quantitative maps for both conditions.

For each subject and for each protocol, the respective CBF activation clusters given by statistical analysis were used to mask the respective quantitative maps, and the mean value within the cluster was calculated. The difference between CBF of activation ( $CBF_{act}$ ) and CBF of rest ( $CBF_{rest}$ ) in absolute unities ( $ml/100g/min$ ) was computed:

$$\Delta CBF = CBF_{act} - CBF_{rest} \quad \text{Equation 4.4}$$

Moreover, the relative variation between  $CBF_{act}$  and  $CBF_{rest}$  in percentage was also calculated:

$$\% \Delta CBF = \frac{CBF_{act} - CBF_{rest}}{CBF_{rest}} \times 100 \quad \text{Equation 4.5}$$

#### 4.4.4. SNR of perfusion-weighted images

The resultant perfusion-weighted images from the ASL difference signal between labelled and control images ( $\Delta M$ ) were used for the estimation of SNR in both GM and WM. For SNR estimates, two ROIs (one per tissue type) with 25 pixels were manually prescribed in the perfusion maps (see Figure 4.7 a) and Figure 4.7 b)) by using the segmented GM and WM masks from FAST as guides. Their mean signal intensity was calculated. Noise was computed as the SD in a 25 pixels ROI placed outside the head in the upper right corner of the image (see Figure 4.7 c)). The mean perfusion SNR was then calculated for both GM and WM. A t test analysis was then performed to assess for significant differences between the mean GM perfusion SNR and the mean WM perfusion SNR.

SNR was computed for PW images of ASL protocol #1 and ASL protocol #2.

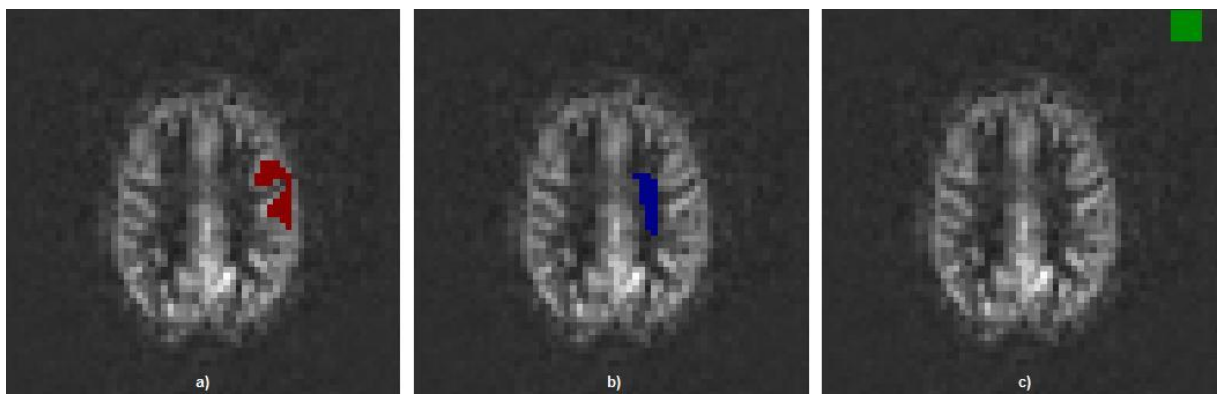


Figure 4.7: Manually prescribed example ROIs for GM and WM SNR estimation: a) GM signal ROI, b) WM signal ROI and c) noise ROI.

#### 4.4.5. CBF quantification: effect of anterior and posterior circulation

For the analysis of both anterior and posterior circulation effects, we consider the quantitative perfusion maps in rest of ASL protocol #1 obtained with *Method 2*. Two regions of interest (ROIs) were selected in each subject. Both ROIs were drawn by hand on the perfusion-weighted maps to select one frontal brain region (ROI 1) and one occipital region (ROI 2). To keep the ROIs equal in size across subjects, both ROIs drawn have 30 voxels each. The mean values of CBF in each ROI were compared.

#### 4.4.6. CBF quantification in GM and WM

To assess the difference between CBF values of GM and WM, we also consider the quantitative perfusion maps in rest of ASL protocol #1 obtained with *Method 2*. Each subject's perfusion map was masked with the binary masks of GM and WM obtained from FAST. The mean value has been calculated.

##### 4.4.6.1. Partial volume effect

One of the two outputs of the segmentation procedure is a partial volume map for each tissue type. It means that for each tissue type, there is a non-binary partial volume image where each voxel contains a value in the range of 0-1 that represents the proportion of that tissue type present in that voxel. These non-binary maps (called *pve\_maps*) were used in order to correct the partial volume effect in the perfusion measurements. For this, the rationale was that the mean value of perfusion in the GM binary mask is equal to the true GM perfusion multiplied by the GM fraction in the mask, i.e., the mean of the GM *pve\_map* in the GM binary mask, added to the true WM perfusion multiplied by the WM fraction in the mask, i.e., the mean of the WM *pve\_map* in the GM binary mask. Following the same logic for the mean perfusion in the WM mask, we reached two expressions:

$$\begin{cases} \langle f \rangle_{GMmask} = \langle pve_{GM} \rangle_{GMmask} f_{GM} + \langle pve_{WM} \rangle_{GMmask} f_{WM} \\ \langle f \rangle_{WMmask} = \langle pve_{GM} \rangle_{WMmask} f_{GM} + \langle pve_{WM} \rangle_{WMmask} f_{WM} \end{cases} \quad \text{Equation 4.6}$$

where  $\langle f \rangle_{GMmask}$  and  $\langle f \rangle_{WMmask}$  are the mean values of CBF in GM and WM binary masks, and  $\langle pve_{GM} \rangle_{GMmask}$ ,  $\langle pve_{WM} \rangle_{GMmask}$ ,  $\langle pve_{GM} \rangle_{WMmask}$ ,  $\langle pve_{WM} \rangle_{WMmask}$  are the mean values of the GM and WM *pve\_maps* in GM and WM binary masks, and  $f_{GM}$  and  $f_{WM}$  are the true CBF values of the GM and WM respectively.

These two equations were then solved in order to determine  $f_{GM}$  and  $f_{WM}$  for each subject and compare with the previous values achieved.



## Chapter 5

### Results and Discussion

In this chapter, the results of the image pre-processing, post-processing and data analysis are shown, explained and discussed. Considering the images presentation, it's important to report that only the images from one of the 15 subjects are presented in order to illustrate the results. The functional images of all subjects can be seen in Appendix A A.3.

#### 5.1. EPI distortion correction

With Neuro 3D task card *Syngo* software, the field map is automatically co-registered to the subject's structural anatomic space and is overlaid on to the structural anatomic image. Figure 5.1 shows a representative EPI image acquired for BOLD experiment and the resulting field map given by Neuro 3D.

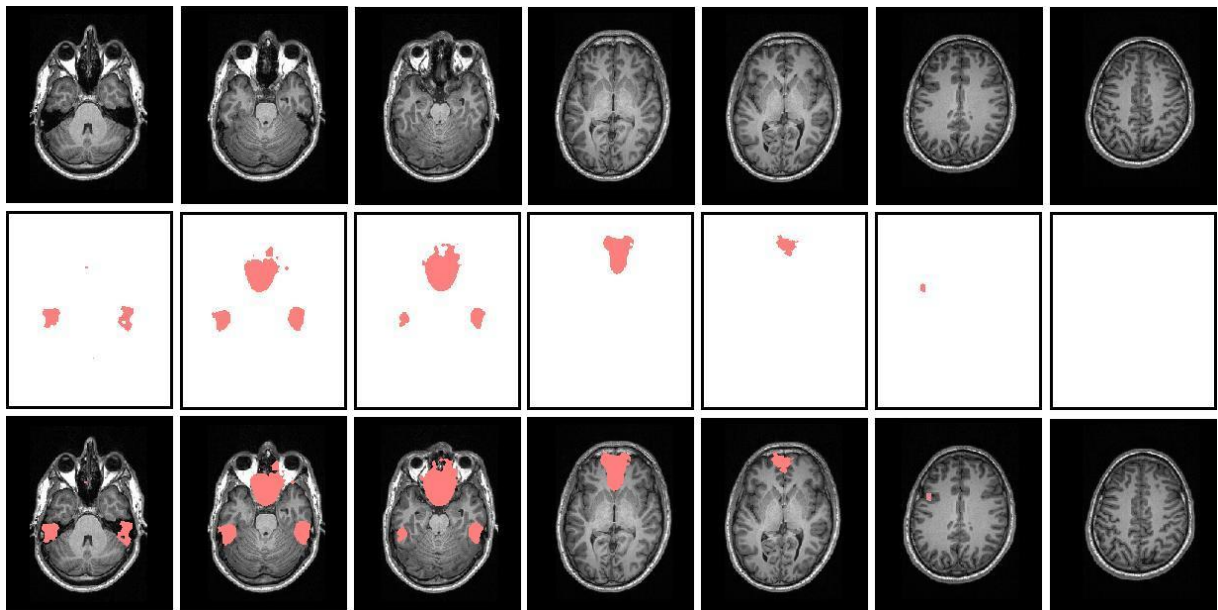


Figure 5.1: Field map image given by Neuro 3D from subject 4. Seven axial slices of the structural image (on the top) and the respective regions of severe field inhomogeneity obtained from the field map (on the middle) are represented. On the bottom is represented the overlay of the field map upon the structural image.

In the images of Figure 5.1 we can see the regions of severe field inhomogeneity obtained from the field map, represented in pink, which are co-registered to the structural space and displayed over the structural image. This pink map points out the regions where local distortion and signal loss of functional images occur, due to the main magnetic field inhomogeneities and the sensitivity of the EPI measurement technique to these.

With FSL we used the fieldmap image given by the scanner without any treatment by Neuro 3D. Figure 5.2 shows a typical fieldmap image from the scanner of one subject.

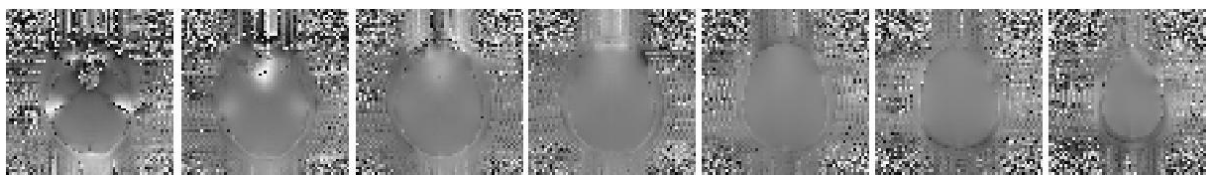


Figure 5.2: Phase difference image given by the scanner from subject 4. Seven representative axial slices are represented.

Although the image appears to be useless, it contains the relevant information about the phase changes, which are proportional to field inhomogeneity and echo time difference. The image obtained after we performed the pre-processing needed to achieve a real field map (application of PRELUDE and conversion to rad/s) is shown in Figure 5.3.

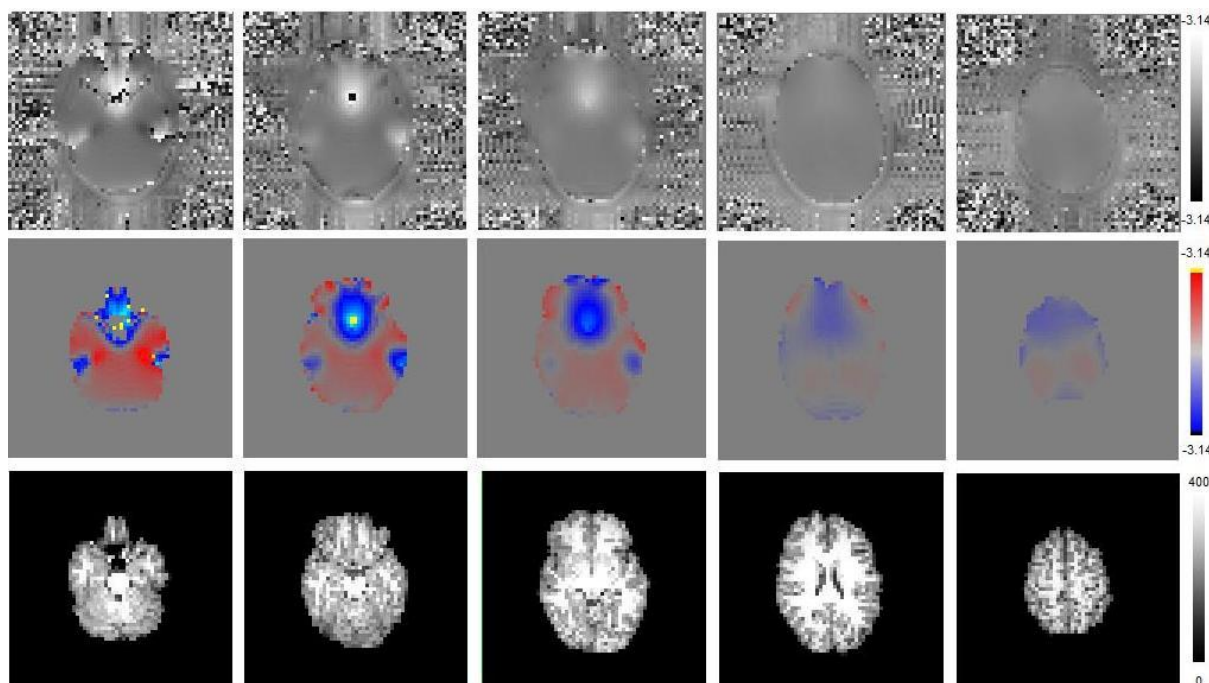


Figure 5.3: Field map obtained with FSL. 5 representative slices from subject 7 are represented: the phase difference image (on top), the unwrapped field map image (on the middle), and the magnitude image (on the bottom).

The two bottom images were the two used in FEAT: the first is the field map image (in rad/s) and the second is the magnitude image. As we can see, image quality improved a good bit.

Like the pink map displayed by Syngo Neuro 3D task card, in the field map achieved the signal is more intense in the inferior temporal and frontal lobes, which means those are the main regions where the functional image’s artifacts are more noticeable. These regions don’t include the primary sensory motor region. Then, in this study the functional results don’t suffer from artefacts caused by the main field inhomogeneities. By the graph of Figure 5.4 we can fully grasp the field map differences between the frontal lobe region and the other brain regions.

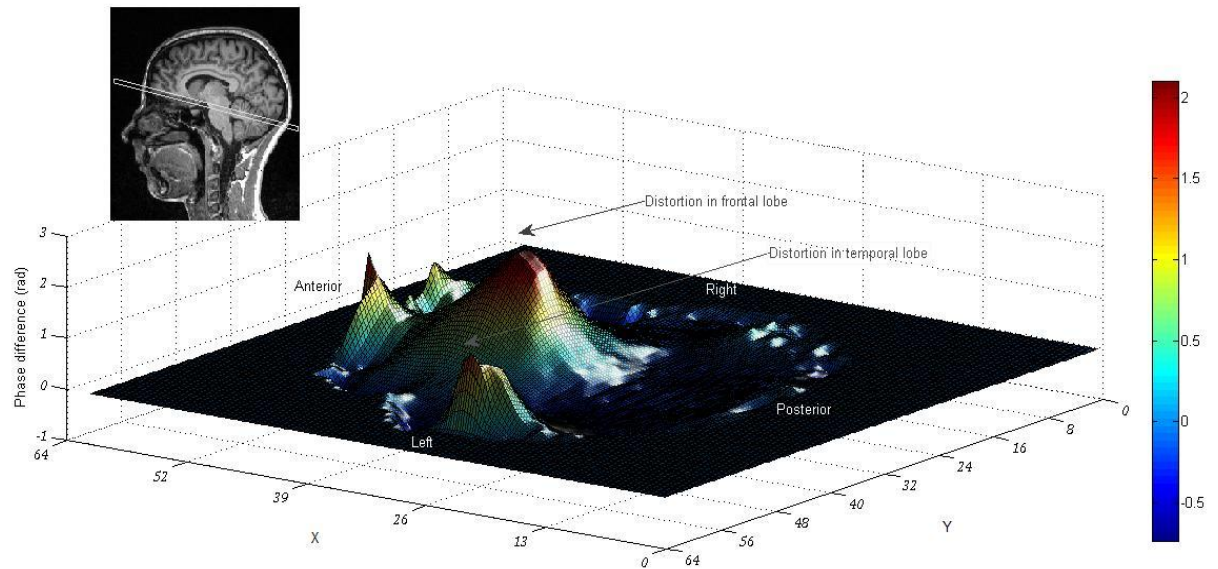


Figure 5.4: 3D representation of one slice of the unwrapped field map. Slice location is showed on top left sagittal slice. The major phase difference (in rads) is clearly shown in the frontal and temporal region of the brain.

In Figure 5.5, the original distorted EPI are compared with the undistorted EPI after FUGUE.

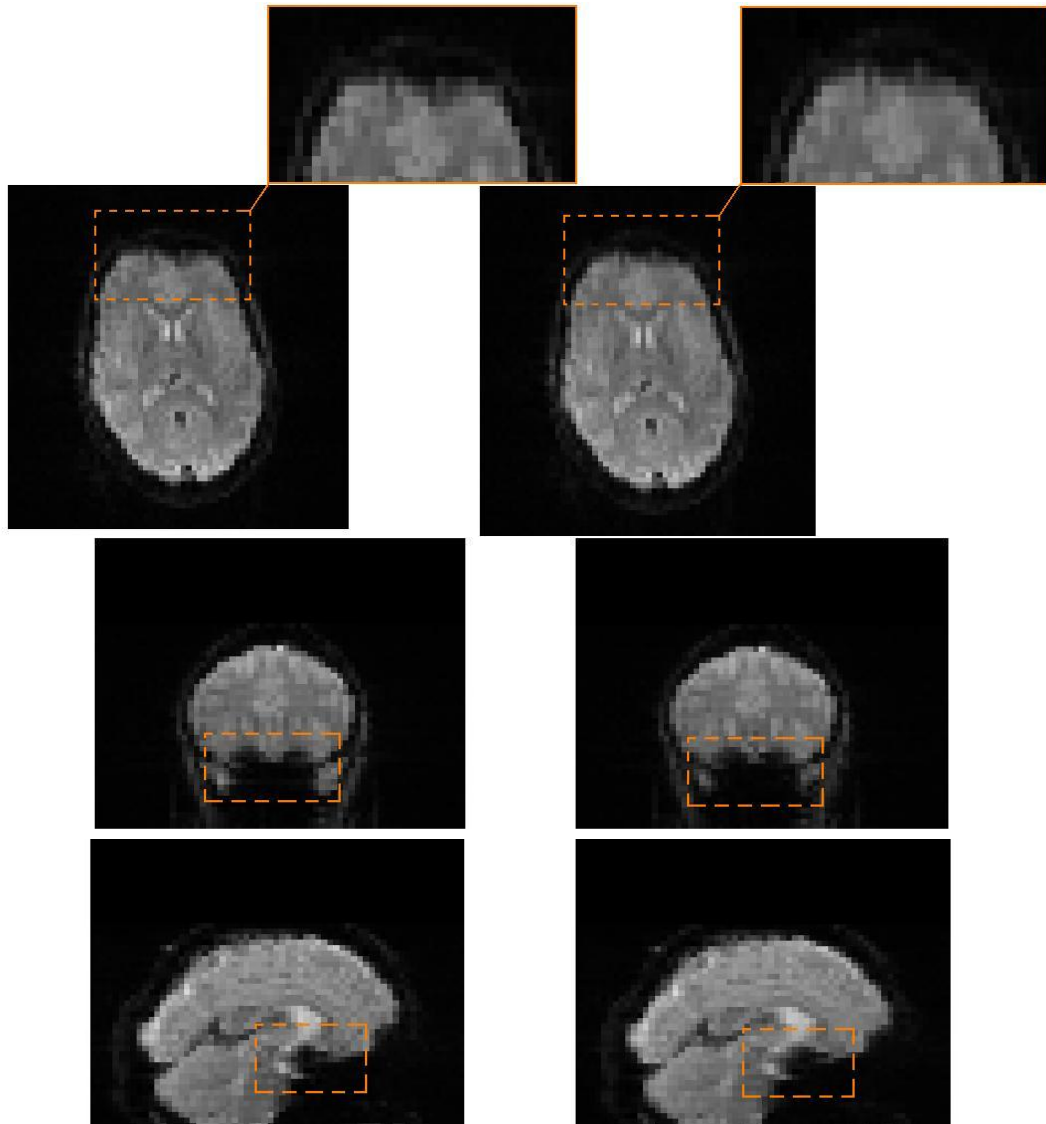


Figure 5.5: Distorted and undistorted EPI images of functional data. On the left we have three different views/plans of the distorted (original) EPI, and on the right we have the same three different views of the undistorted (after FUGUE) EPI.

In Figure 5.5, orange squares point out the areas where differences between the corrected and uncorrected images are more pronounced. In the right images, we can observe some improvements in the EPI images. Although the signal loss (intensity) wasn't restored, local geometric distortion presented in the original EPI was corrected. Moreover, we used both EPI distorted and undistorted images in registration procedures. And the distortions of the original EPI images lead to more global errors in registration than undistorted EPI images.

Distortion of EPI-based functional images is a particular problem for high-field (3T and higher) MR scanners. The inhomogeneities in the magnetic field caused by susceptibility differences at air–tissue interfaces (predominantly near air-filled sinuses) result in both signal loss and geometric distortion of images. As we saw, such artefacts are particularly noticeable in the inferior temporal and frontal lobes, and restrict the use of standard fMRI techniques in these areas. In addition, the distortions can also lead to global errors in registration, if not accounted for, causing errors in the spatial localisation of activations from any brain region, including those where there is little or no distortion present. Then the acquisition of this field map is very important in clinical applications. With Neuro 3D task card from Syngo software, areas where functional information is superimposed upon anatomic data can be checked against the field map. If field map distortion and functional activation overlap, then this information must be ignored for the reason that local distortion and signal loss “contaminate” that region. Otherwise, FSL allows not only field map display over the anatomic structural image but also correction of the EPI distortions, although it can't restore signal loss. In practice, this approach is very useful to allow a better registration and to achieve fewer errors in the spatial localisation of activations with functional data.

## 5.2. Comparing three functional protocols

With Neuro 3D, the statistical map (t-map) from BOLD protocol data was displayed over the structural anatomic image of each subject. Figure 5.6 illustrates the achieved image: we can see the activation clusters in the primary hand motor cortex of the left hemisphere, which is consistent with bibliography findings.

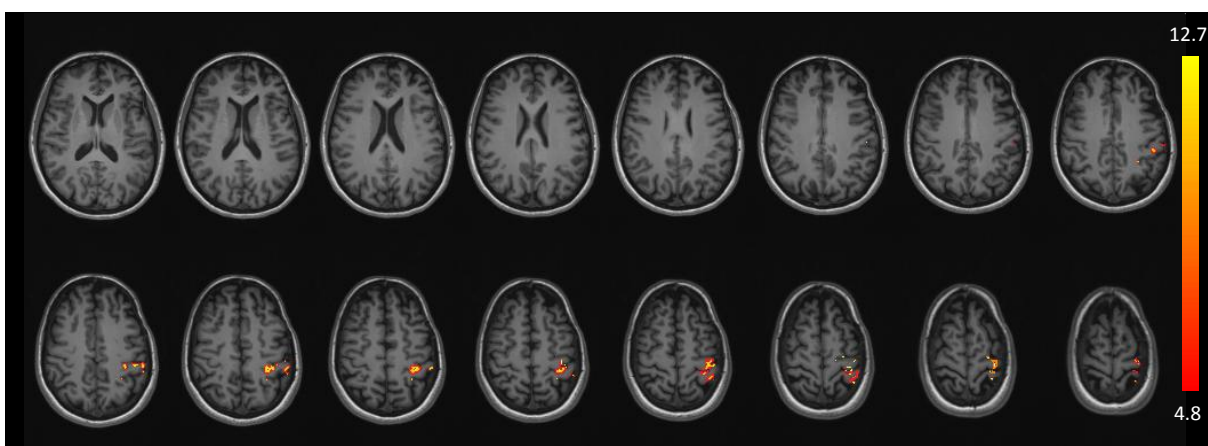


Figure 5.6: BOLD statistical map obtained with FSL from Subject 2. BOLD results are displayed over the structural anatomic image.

The functional ASL data processing with Neuro 3D was limited. Therefore, it was only possible to analyse the ASL protocol #1, and not the ASL protocol #2, with this software. In that case, we have performed the subtraction between the quantitative  $relCBF_{rest}$  map corresponding to the rest state and the quantitative  $relCBF_{activation}$  map corresponding to motor activation (the procedure is presented in Appendix A A.1). The result of this image processing is shown in Figure 5.7.

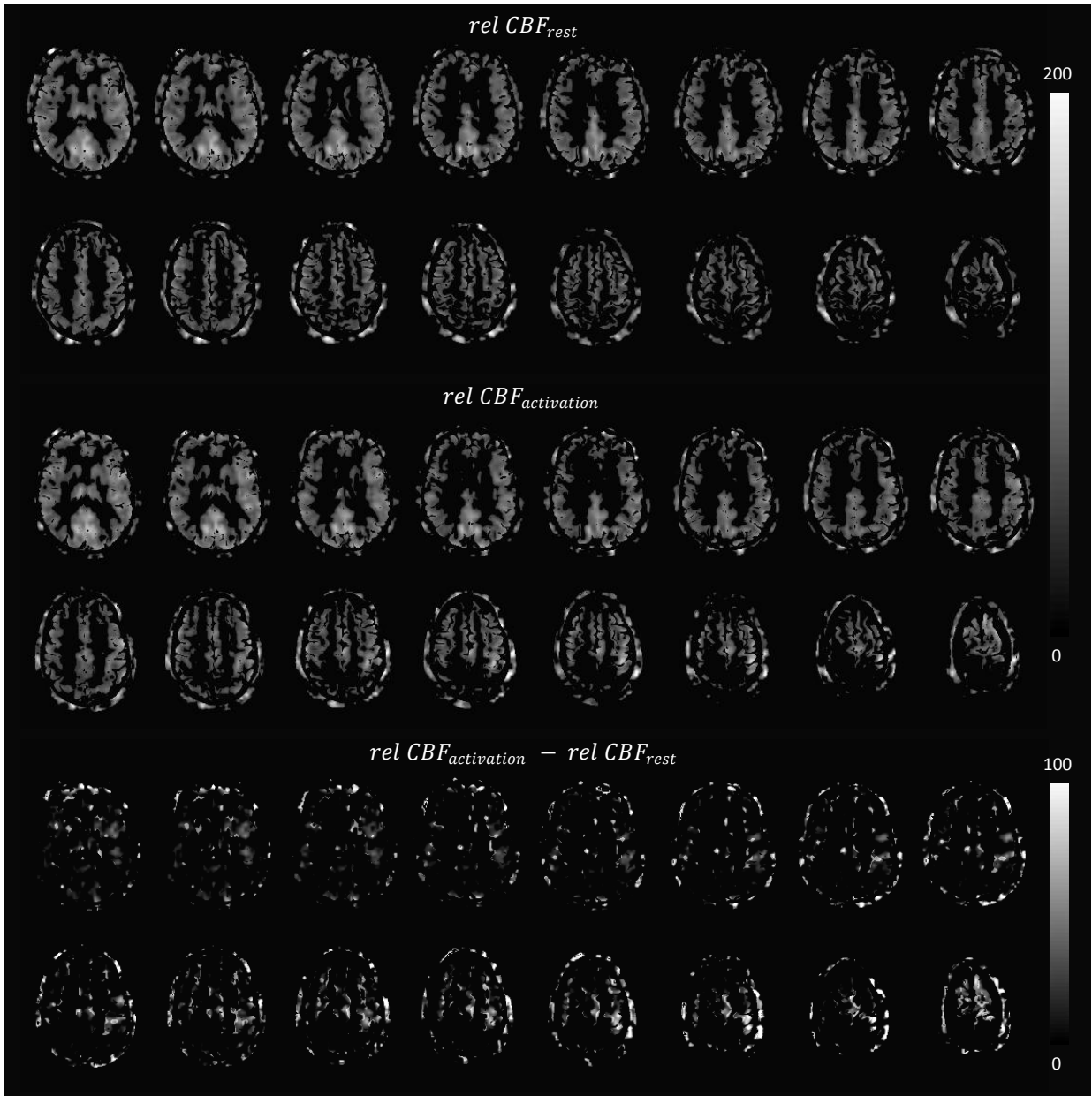


Figure 5.7: Perfusion maps obtained with Neuro 3D, for 16 axial slices in one subject. With this software,  $relCBF$  maps are co-registered to the structural space, and then the image processing was carried out. Top: quantitative  $relCBF$  maps corresponding to the rest state and to motor activation (respectively). Bottom: resultant map from the subtraction of the previous maps.

As we can see, the difference image exhibits signal intensity in the primary sensory motor region, which reflects the perfusion change between the two states. Then, this difference image also shows the brain region that was activated by the motor task. For better comparison, we performed a fusion between BOLD information and the difference image (see Figure 5.8).

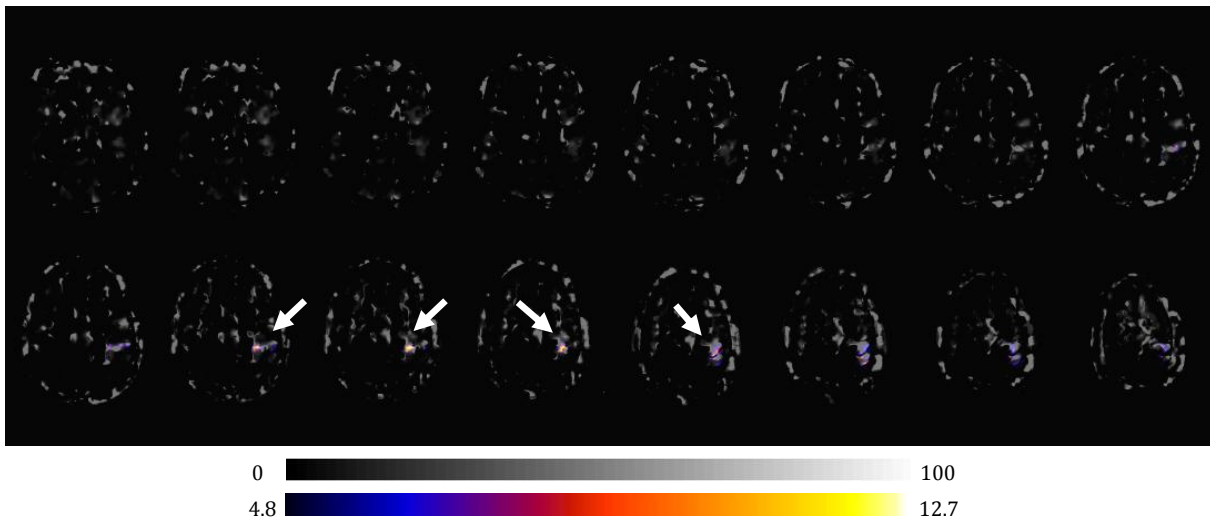
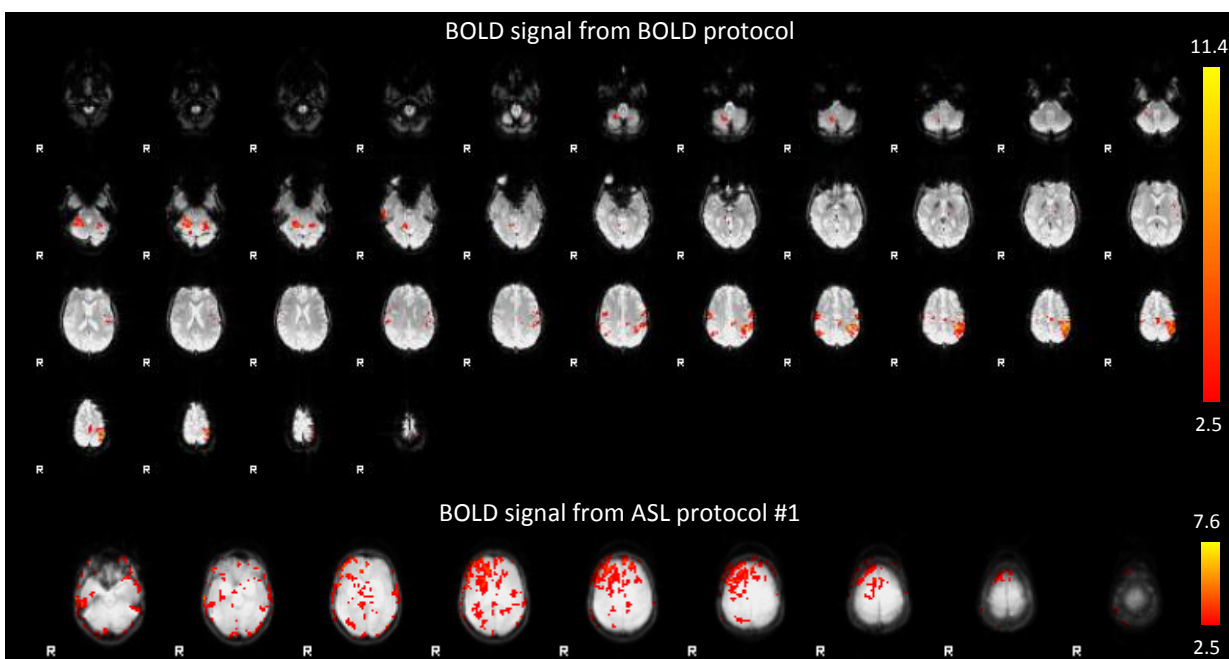


Figure 5.8: Fusion between BOLD t statistical map and the ASL difference map between  $relCBF_{activation}$  and  $relCBF_{rest}$  maps. Grey colour scale is related to CBF absolute units (ml/100g/min), and the hot metal colour scale corresponds to the t-value from the t statistical test.

In the fused image, we can see that there's some agreement between both informations in the motor activation region, since there's an overlap between BOLD statistical map and the difference image between  $relCBF$  maps. However, we are combining and comparing here two different types of information that can lead to an erroneous interpretation. In this approach, BOLD information is provided by a statistical t test that results from several complex steps, while ASL information is the result of a simple subtraction between two images acquired in different conditions. In fact, we performed a fusion of a statistical map with a CBF difference map, which is not the best approach if we want to compare the specificity of both activations. It might have some applications, but with this approach we are not completely using the potential of ASL for functional analysis.

With FSL we were able to perform a more complete analysis of functional BOLD and ASL protocol's data. The post-stats results from BOLD protocol and functional ASL protocols #1 and #2 are shown in Figure 5.9.



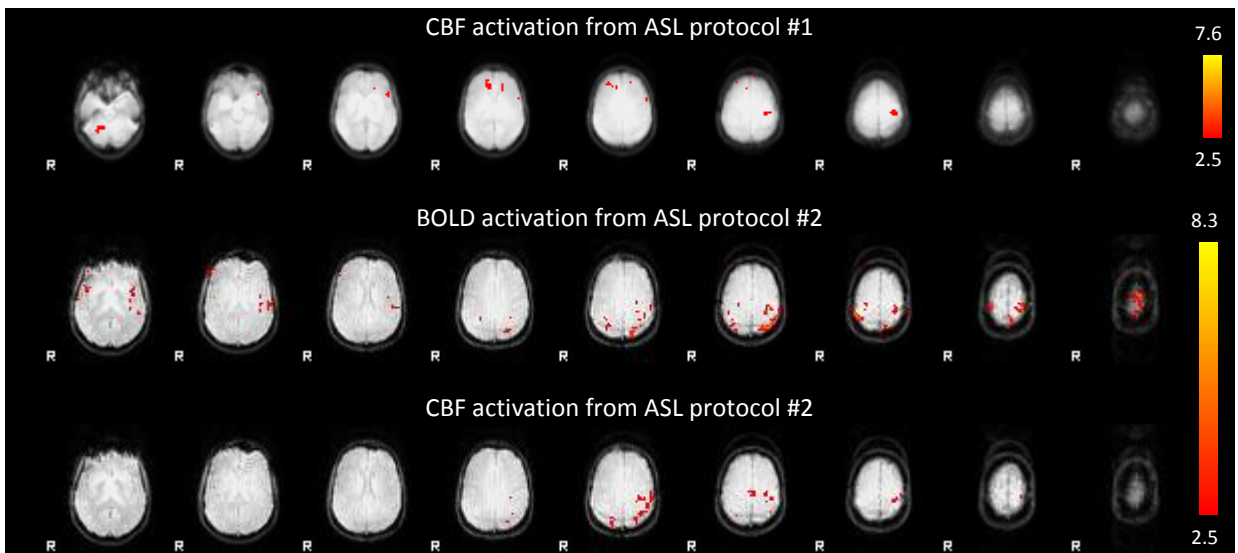
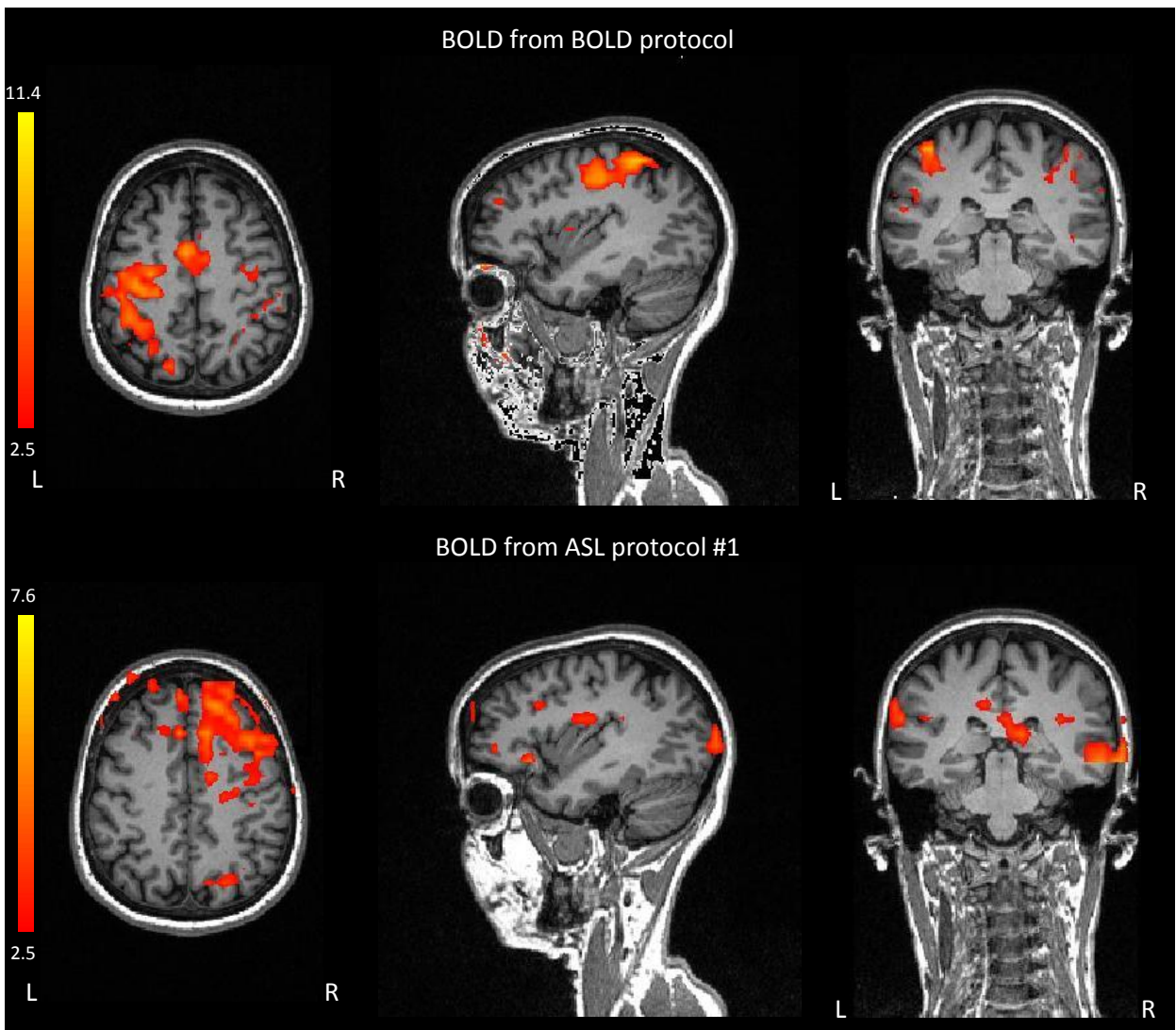


Figure 5.9: Activation Z maps superimposed on an example EPI image obtained for each experiment of each protocol from subject 2.

The group of images shown above demonstrates the z-map of BOLD activation from BOLD protocol and the z-maps of BOLD and CBF activations from ASL protocols #1 and #2 for one subject. For better interpretation of these results and to allow a better localisation of the hand motor area, the statistical maps were registered to the structural anatomic image space (see Figure 5.10).



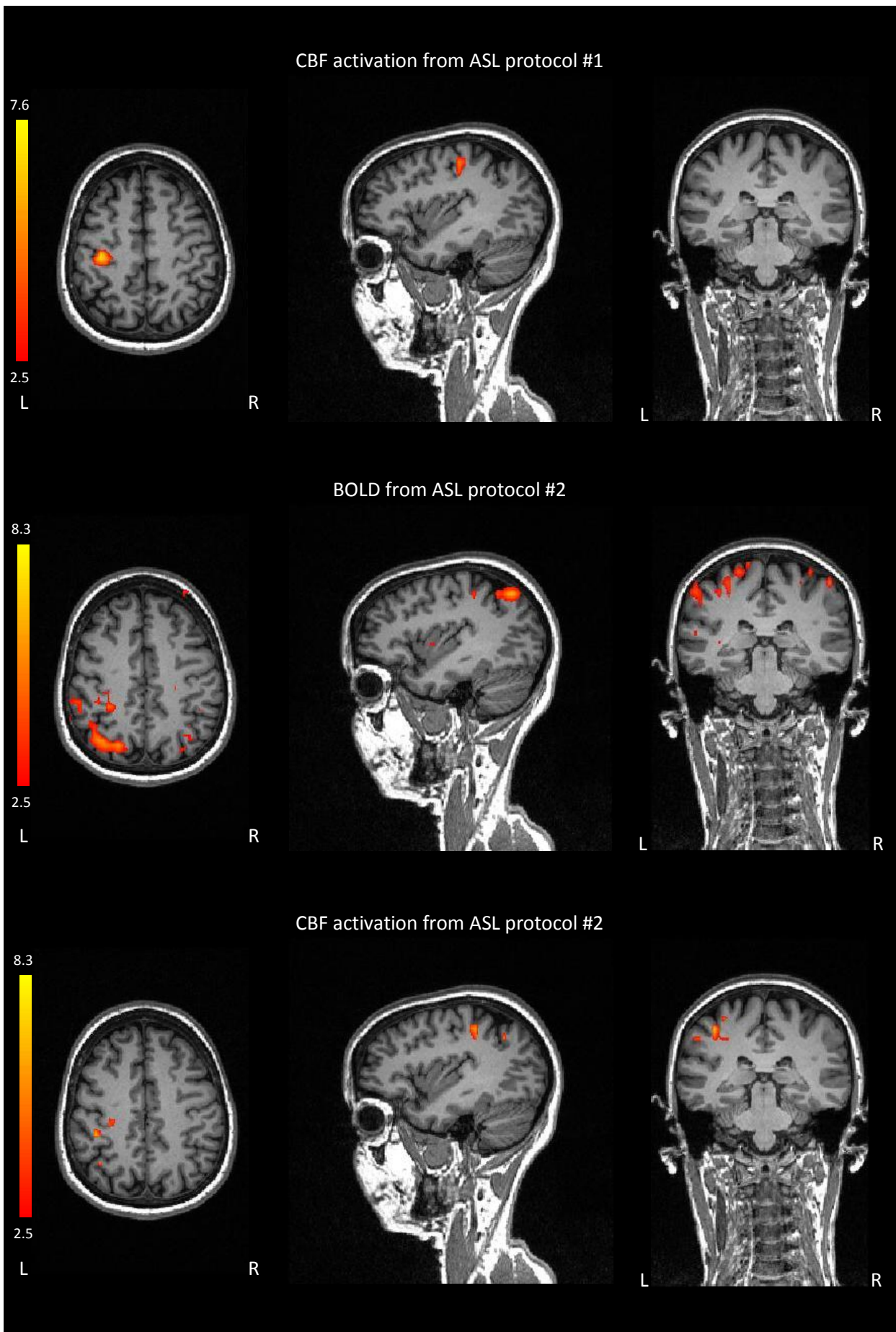


Figure 5.10: Activation Z maps (scale indicated in colorbar) obtained for each experiment of each protocol superimposed on the structural anatomic image from subject 2: from left to right we have the axial, sagittal and coronal planes, respectively.



For all subjects, the three functional protocols were able to give information of activation areas in the HMC of the left hemisphere of the brain. Although it wasn't expected good results with ASL basic protocol #1 data, functional information can be seen in the statistical map obtained for CBF activation. However, ASL protocol #1 doesn't have a design's shape commonly used to assess functional information. It consists in a single block design which is not optimized for functional studies. In this protocol, distinctively from the others functional protocols, there is only one change between the condition of rest and the condition of activation. As we know, the measured functional signal is based on changes between the state that we want to explore and a state of reference. If there is only one exchange between these two states, the study will be limited to few relevant statistical data, which can induce poor functional information. According to that, we can conclude that ASL protocol #1 is not optimized for functional studies. In fact, the BOLD activation results extracted from ASL protocol #1 are not consistent with the results given by the other experiments, as we can see in Figure 5.10; they don't point the activation region near the HMC on the left side of the brain.

Therefore, the basic ASL protocol #1 was discarded for functional studies and changed to ASL protocol #2, which provided significantly better results. Indeed, for this new protocol both BOLD and perfusion activation regions are consistent with the expected, providing a good localisation of the brain region responsible for the motor task.

Moreover, the optimized functional ASL protocol #2 allows simultaneous BOLD and perfusion data acquisition, since both contrasts can be retrieved from a single acquisition.

### 5.3. Variability of extent and localisation of motor activation

The MNI coordinates for the centre of gravity (COG) of the activation regions, as well as the number of activated voxels, for each subject and for each protocol, BOLD, BOLD<sub>ASL</sub> and CBF, are summarized in Table 5.1.

The mean number of activated voxels in the hand motor cortex was  $27.0 \pm 4.7$  for CBF,  $299.7 \pm 54.0$  for BOLD<sub>ASL</sub> and  $386.1 \pm 78.2$  for BOLD, as summarized in Table 5.2. Analyses of Variance (ANOVA) revealed significant differences in the number of voxels between the three experiments ( $p < 0.050$ ). Post-hoc multiple comparison of mean voxel values according to Scheffe revealed significantly fewer activated voxels for CBF relative to BOLD<sub>ASL</sub> ( $p = 0.004$ ) and for CBF relative to BOLD ( $p < 0.001$ ).

Table 5.2 summarises the results of the variance of each coordinates for each experiment across the 15 subjects. The variance values of the COG coordinates for CBF activation are smaller than the variance values for the other modalities.

Table 5.1

Results for the analysis of the location of activation measured by the centre of gravity (COG) and number of activated voxels for BOLD, BOLD<sub>ASL</sub> and CBF

Subject	MNI coordinates for centre of gravity ( $x, y, z$ ) in mm									Number of activated voxels		
	BOLD			BOLD <sub>ASL</sub>			CBF			BOLD	BOLD <sub>ASL</sub>	CBF
1	-28.9	-12.8	42.3	-17.3	-20.4	67.9	-31.8	-28.9	53.3	265	110	33
2	-19.3	-9.19	46	-39.9	-18.5	60.3	-36.7	-19.3	52.3	614	58	12
3	-33.1	-18.0	47.2	-26.0	-40.7	59.2	-38.3	-22.1	51.4	773	258	29
4	-40.5	-8.51	50.5	-36.6	-19.6	59.5	-35.4	-23.1	50.8	215	156	24
5	-20.8	-5.4	50.1	-23.8	-20.1	55.2	-31.1	-19	52.8	176	125	10
6	-14.7	-41.2	55.6	-42.9	-17.1	53.0	-35.3	-17.6	57.3	94	63	7
7	-32.2	-27.5	51.9	-22.7	-6.15	56.6	-30	-22.9	56.2	193	380	33
8	-33.2	-26.3	51.6	-34.6	-17.2	57.5	-38.4	-13.7	54.1	117	281	87
9	-41.2	-3.94	49.6	-20.0	-7.85	42.5	-30.6	-17.4	48.8	299	765	20
10	-36.4	-18.4	57.3	-20.7	-28.9	57.7	-35.3	-16.3	51.8	438	479	20
11	-43.2	-31.4	49.3	-28.8	-12.6	53.4	-39.5	-12.2	52.0	1173	372	28
12	-37.1	-15.1	52.8	-42.7	-15.7	61.9	-35.9	-10.3	53.5	693	472	18
13	-41.8	-10.1	51.8	-39.8	-12.4	47.0	-38.2	-14.6	52.1	142	187	31
14	-30.5	-10.6	57.8	-38.2	-36.1	53.2	-36.2	-12.2	53.2	305	603	31
15	-31.8	-24.1	49.3	-31.6	-26.5	51.3	-32.7	-25	58.0	294	186	16
G. mean	-32.3	-17.5	50.9	-31.0	-20.0	55.8	-35.0	-18.3	53.2	386.1	299.7	27.0
± (SE)	(2.2)	(2.7)	(1.1)	(2.3)	(2.5)	(1.6)	(0.8)	(1.4)	(0.6)	78.2	54.0	4.7

Table 5.2

Results for the calculation of variance of MNI COGs for CBF, BOLD<sub>ASL</sub> and BOLD activations across  $N = 15$  subjects

Experiment		N	Range (mm)	Minimum (mm)	Maximum (mm)	Std. Deviation (mm)	Variance (mm <sup>2</sup> )
CBF	X	15	9,5	-39,5	-30,0	3,0889	9,541
Activation	Y	15	18,6	-28,9	-10,3	5,3181	28,282
	Z	15	9,2	48,8	58,0	2,4450	5,978
BOLD <sub>ASL</sub>	X	15	25,6	-42,9	-17,3	8,8519	78,357
activation	Y	15	34,5	-40,7	-6,2	9,6208	92,561
	Z	15	25,4	42,5	67,9	6,1616	37,966
BOLD	X	15	28,5	-43,2	-14,7	8,5477	73,063
Activation	Y	15	37,3	-41,2	-3,9	10,3146	106,391
	Z	15	15,5	42,3	57,8	4,1043	16,845

The variance across subjects can be qualitatively evaluated with the illustration in Figure 5.11. In this figure, the inter-subject activation maps obtained for the three protocols are shown on the MNI standard brain. These maps represent the COGs and the local maxima of the activation clusters for all subjects, for each experiment. Figure 5.12 shows that the activation cluster achieved with CBF is within both BOLD and BOLD<sub>ASL</sub> activation clusters.

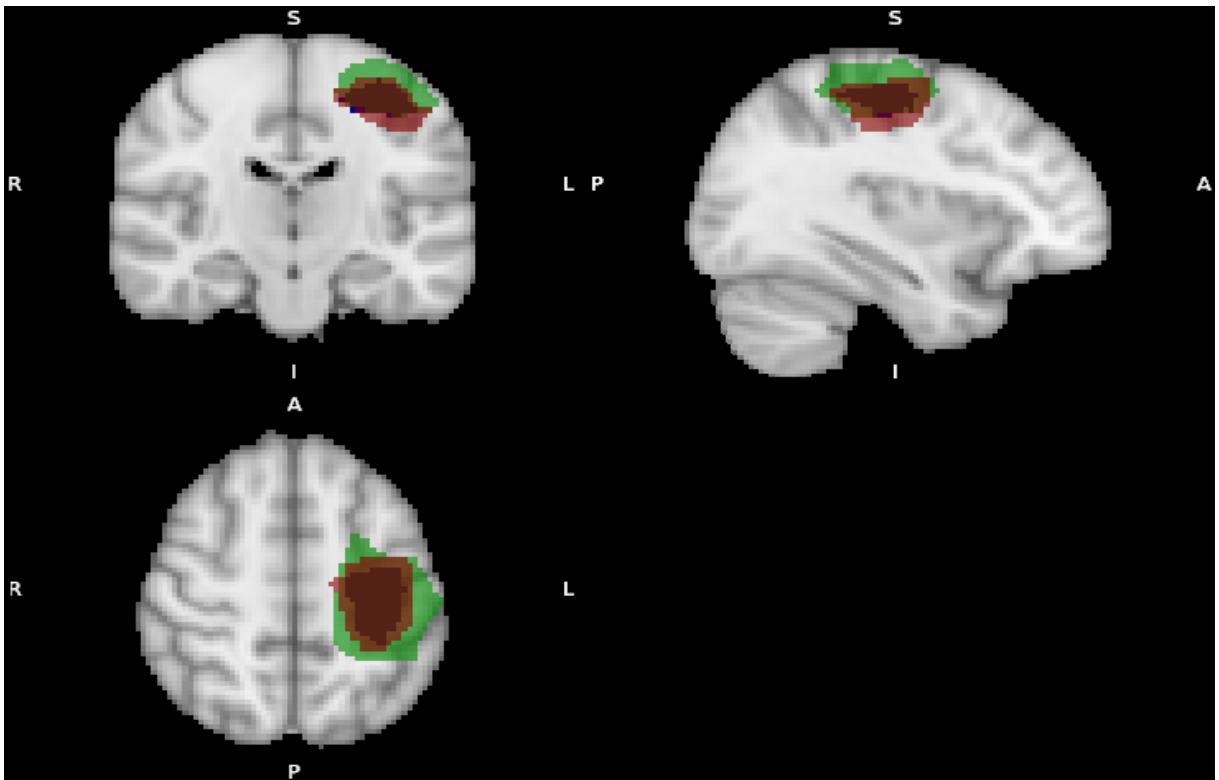


Figure 5.11: Orthogonal views (coronal, sagittal and axial) of inter-subject activation maps for BOLD (red), BOLD<sub>ASL</sub> (green) and CBF (blue) in the MNI standard brain.

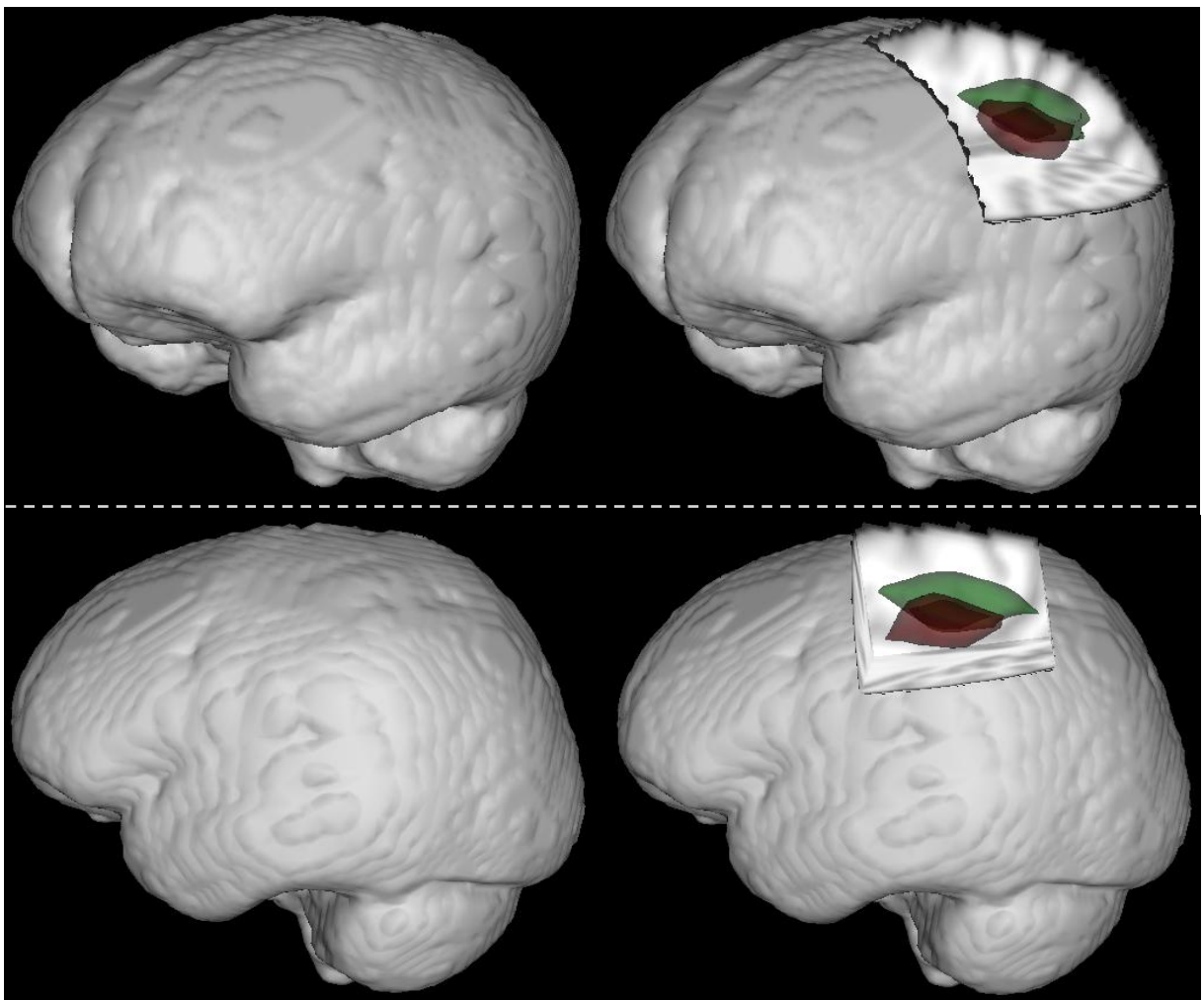


Figure 5.12: 3D views of inter-subject activation clusters for BOLD (red), BOLD<sub>ASL</sub> (green) and CBF (blue). On the left is represented the MNI brain, and on the right is represented the MNI brain without a piece of it to show activation clusters.

These results show that between-subject variability in motor activity localisation was smaller when measured with perfusion fMRI as compared with BOLD fMRI. On the other hand, the group activation maps showed larger areas of BOLD and BOLD<sub>ASL</sub> activations compared to CBF (see Figure 5.11 and Figure 5.12), reflecting the superior sensitivity of BOLD compared to ASL. Since perfusion images are not sensitive to many of the non physiologic factors that impact BOLD images, this is an expected result. These results suggest that blood flow changes were more consistent across subjects than changes in BOLD contrast.

Figure 5.13 shows the positions of the 9 points used to localise the HMC of the left hemisphere of the MNI standard brain. The two mean points C1 and C2 are also displayed in this figure.

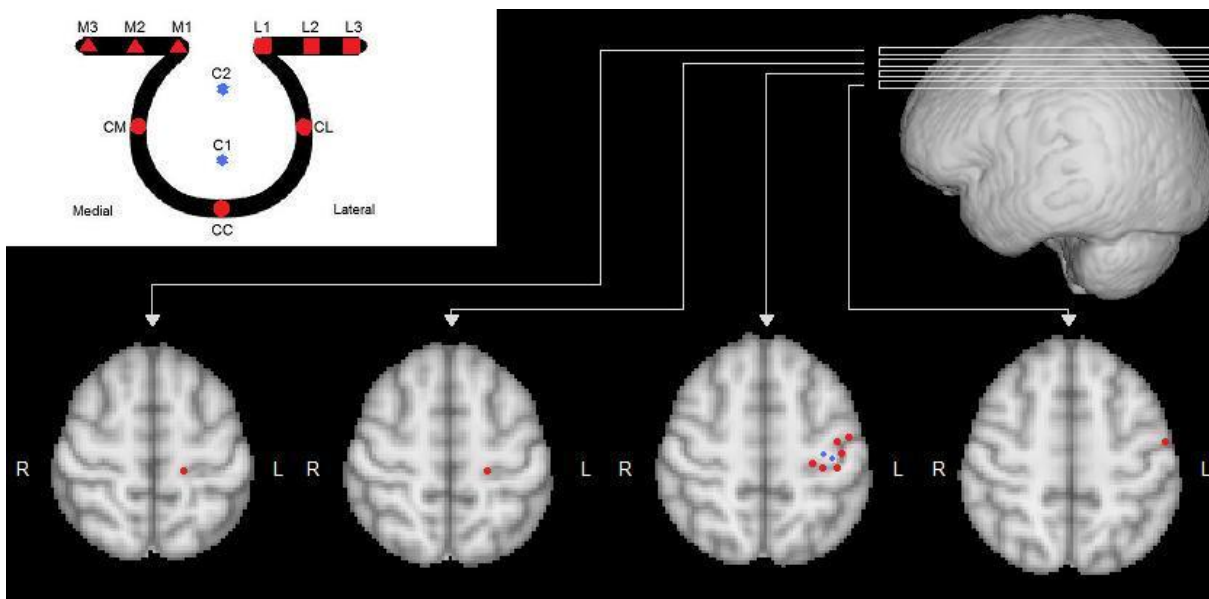


Figure 5.13: Localisation of the hand primary motor cortex. The representation on the top left corner illustrates the 9 points over the segment of the precentral gyrus (red) and the two mean points calculated (blue). The same points are shown in the MNI brain axial slices (bottom). The segment of the precentral gyrus is not contained in one single axial slice, so we had to localise it over four different axial slices, positioned as illustrated on the top right.

Figure 5.14 summarises the mean Euclidean distance from the 11 points of HMC to BOLD, BOLD<sub>ASL</sub> and CBF activation COGs.

ANOVA revealed significant differences in the distances between BOLD, BOLD<sub>ASL</sub>, and CBF COGs with respect to CL ( $p < 0.017$ ), L1 ( $p < 0.019$ ), C1 ( $p < 0.017$ ) and C2 ( $p < 0.009$ ). The post-hoc multi comparison of the mean distance values according to Scheffe revealed significant differences between the following distances: CBF and BOLD<sub>ASL</sub> COG to CL ( $p < 0.036$ ), CBF and BOLD<sub>ASL</sub> COG to L1 ( $p < 0.027$ ), CBF and BOLD COG to C1 ( $p < 0.041$ ), CBF and BOLD<sub>ASL</sub> COG to C1 ( $p < 0.046$ ), CBF and BOLD COG to C2 ( $p < 0.010$ ) and CBF and BOLD<sub>ASL</sub> COG to C2 ( $p < 0.013$ ). A quantitative exposition of Figure 5.14 is given in Appendix A A.4, with the distance values for each subject.

The localisation of the HMC allows the comparison of the spatial location of activation COGs in the MNI standard brain. We found that CBF activation was closer to the HMC points compared to BOLD and BOLD<sub>ASL</sub>. This supports the notion that CBF may more accurately localise brain activation due to its greater sensitivity to changes in the capillary bed local to the activated neuronal population

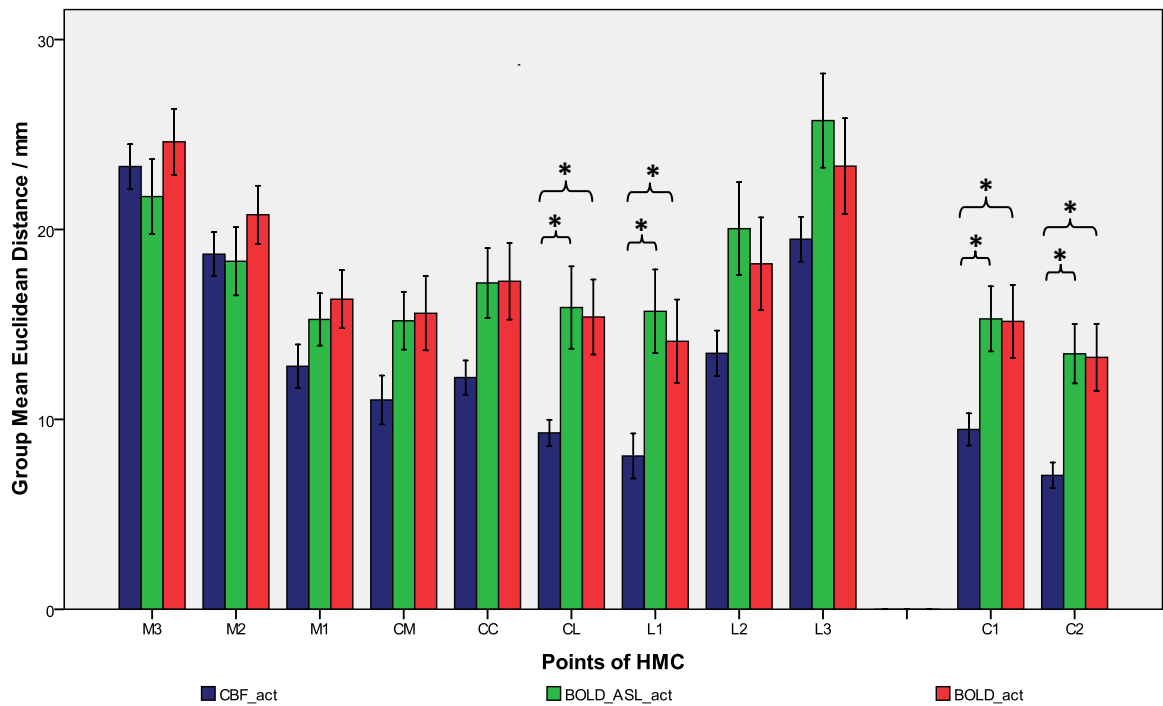
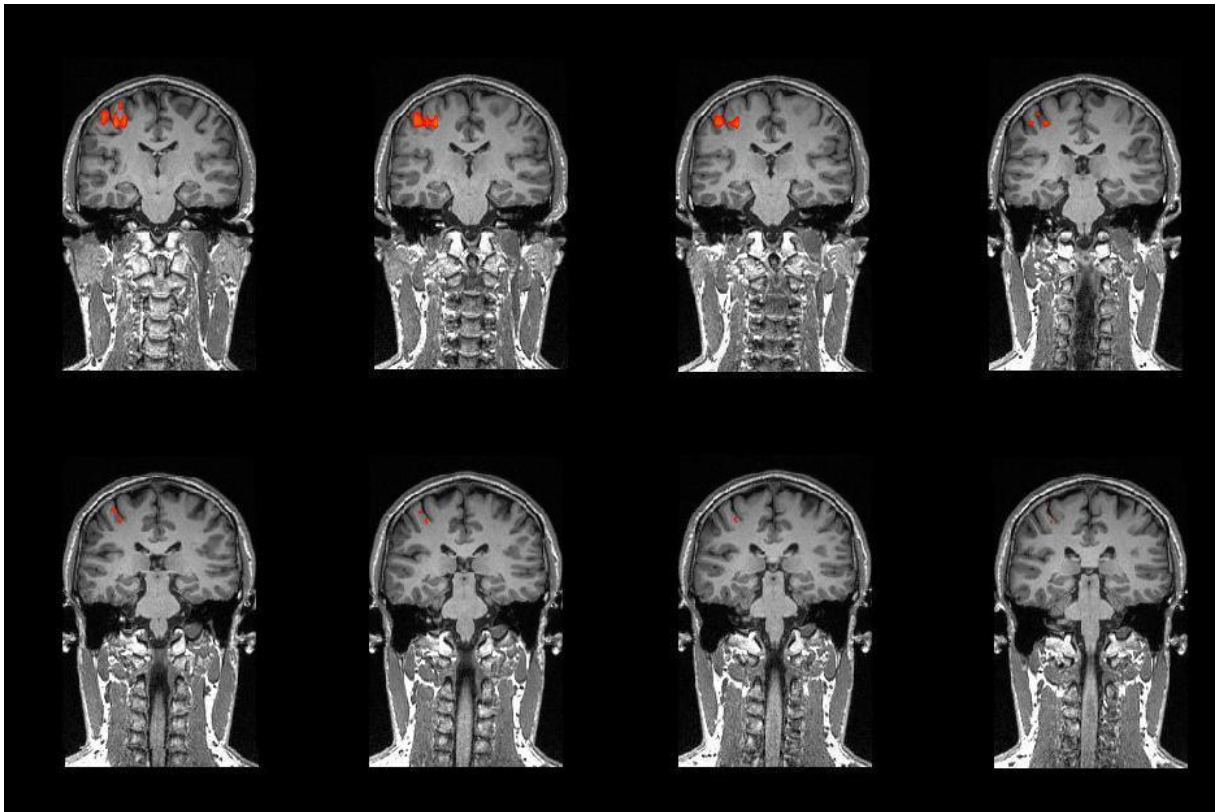


Figure 5.14: A plot of the group mean Euclidean distance (in mm) from HMC points to CBF, BOLD<sub>ASL</sub> and BOLD activation COGs. Error bars denote one standard error of the group mean. \* denotes significant differences between the pointed bars.

than the venule side – as is the case for BOLD contrast. Indeed, some BOLD fMRI studies showed apparent activation over distant draining veins that is not observed using perfusion contrast (see Figure 5.15).

#### CBF Activation



BOLD Activation

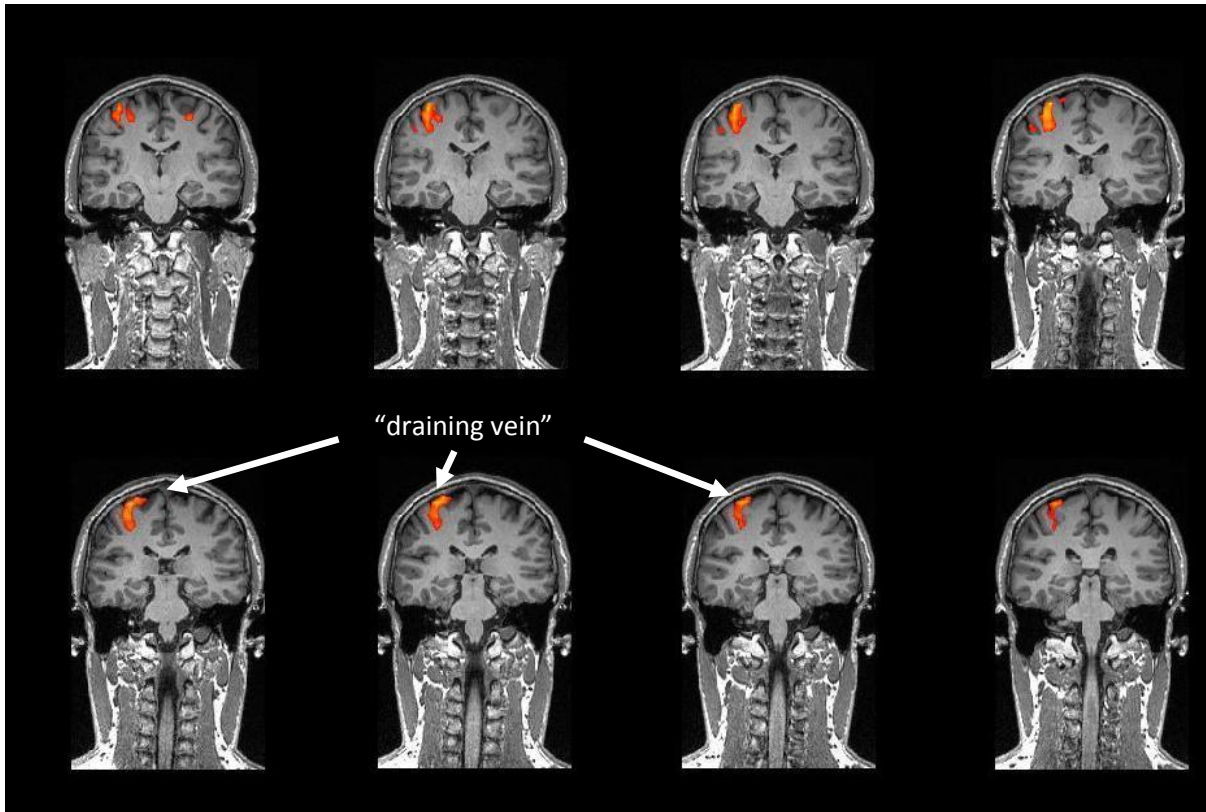


Figure 5.15: Representation of BOLD and CBF activations in coronal slices of subject 12 (presented from anterior to posterior, from left to right and from top to bottom in the figure), showing apparent activation over draining veins for BOLD experiment, but not for ASL.

In Figure 5.15, activation detected with perfusion MRI is confined to the HMC, whereas BOLD contrast also shows apparent activation over the superior longitudinal sinus (indicated by arrows) which drains motor cortex. Furthermore, considering the original points drawn to localise HMC, as we can see in the graph of Figure 5.14, CBF was significantly closer to the central and lateral points CL and L1, and mean points C1 and C2, which is consistent with a study that showed individual digit activated areas with predominance in the lateral region of the segment of the precentral gyrus [51].

Despite all of this, we have to be careful when we are looking for the evidence for greater accuracy of localisation with CBF. If we consider the group mean Euclidean distance between the modalities (see Table 5.3), we observe that these values are within the intrinsic spatial resolution of collected data ( $3.5 \times 3.5 \times 6 \text{ mm}^3$  for CBF and  $\text{BOLD}_{\text{ASL}}$  and  $4 \times 4 \times 3 \text{ mm}^3$  for BOLD).

Table 5.3  
Group mean Euclidean distance between modalities (BOLD,  $\text{BOLD}_{\text{ASL}}$  and CBF)

	Euclidean distance between BOLD and $\text{BOLD}_{\text{ASL}}$	Euclidean distance between CBF and $\text{BOLD}_{\text{ASL}}$	Euclidean distance between CBF and BOLD
Group mean $\pm$ SE	$5.65 \pm 1.05 \text{ mm}$	$5.06 \pm 1.10 \text{ mm}$	$3.64 \pm 0.93 \text{ mm}$

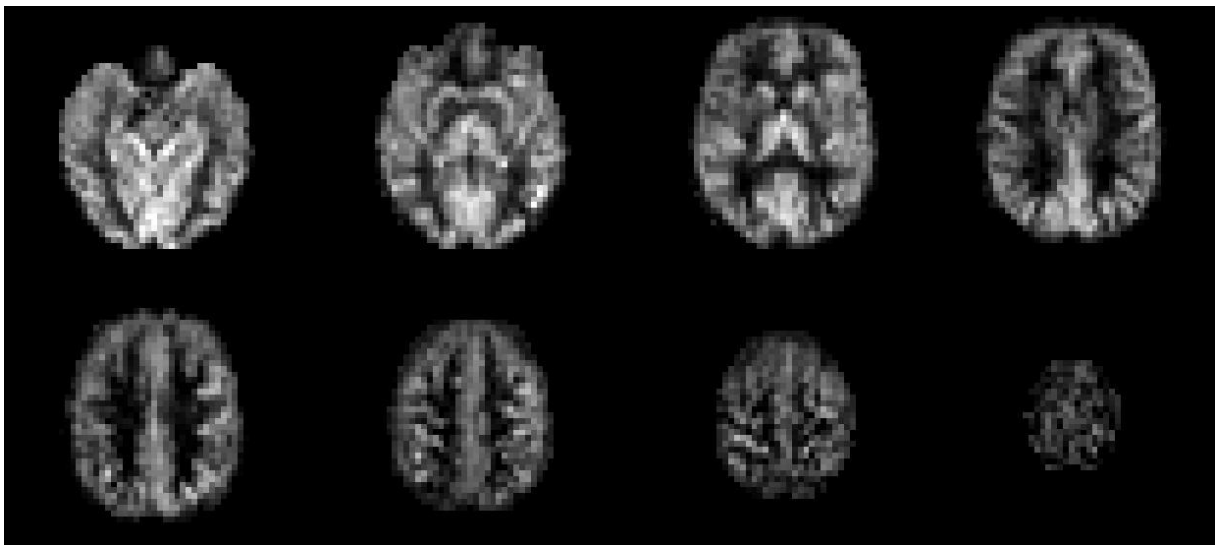
Although the MNI standard space to which the experiments were registered has a better resolution ( $2 \times 2 \times 2 \text{ mm}^3$ ), the space where functional data was collected is the one that we must consider. In fact, these differences could be due, at least in part, to registration problems during

transformation from functional to the structural space of the MNI brain. Moreover, we mustn't forget that, for registration of ASL data, comparing with BOLD data registration, we needed to do an additional transformation (since the imaging slab doesn't cover the whole brain), which consists in using a low resolution image that covers the entire brain (in practice, an EPI image from BOLD data). The usage of an additional transformation introduces one additional source of errors, which can affect the localisation of activation COGs in the structural space.

Nevertheless, the consistency of the results is undeniable. In fact, 15 heads were analysed in this study, which provides a good statistical number for validation of the results. Besides, in literature there are some different approaches that support that this occurs [4, 42, 52-54]. So, and according to the information posted in Chapter 2 and Chapter 3 about the nature of BOLD and ASL signals, the results achieved corresponded to the expected.

#### 5.4. CBF quantification: comparing the three methods

Figure 5.16 shows a typical quantitative perfusion-weighted image obtained from a 25 year-old female subject.



0 ml/100g/min  150 ml/100g/min

Figure 5.16: A typical perfusion-weighted image from a 25 years old female subject. The first 8 axial slices are shown from inferior (top left) to superior (bottom right). The top slice (ninth slice) is not shown because it does not have any brain signal.

For this study, only the image of rest from ASL protocol #1 was used. The values of perfusion used for comparison between the 3 methods described in Section 4.4.2, were obtained by applying the grey matter (GM) binary mask of each subject as a ROI.

Table 5.4 shows the results of CBF values calculated by the 3 methods for each subject.

Table 5.4  
 CBF values in  $ml/100g/min$  in the GM mask for each subject calculated using the three methods

Subject	Cerebral brain flow (CBF) values ( $\pm$ SE) in the grey matter mask in absolute units of $ml/100g/min$		
	Method 1	Method 2	Method 3
1	64.44 $\pm$ 1.23	66.46 $\pm$ 1.25	61.19 $\pm$ 1.28
2	69.86 $\pm$ 1.80	71.88 $\pm$ 1.83	67.31 $\pm$ 1.89
3	70.01 $\pm$ 1.34	72.06 $\pm$ 1.36	67.33 $\pm$ 1.44
4	74.41 $\pm$ 1.45	76.87 $\pm$ 1.48	70.19 $\pm$ 1.51
5	72.86 $\pm$ 1.79	75.79 $\pm$ 1.81	67.67 $\pm$ 1.87
6	57.05 $\pm$ 1.28	58.92 $\pm$ 1.30	53.86 $\pm$ 1.35
7	71.69 $\pm$ 1.52	73.97 $\pm$ 1.56	67.99 $\pm$ 1.53
8	61.67 $\pm$ 0.98	63.83 $\pm$ 0.98	57.71 $\pm$ 1.06
9	47.74 $\pm$ 1.17	49.43 $\pm$ 1.18	44.58 $\pm$ 1.22
10	67.44 $\pm$ 1.11	69.88 $\pm$ 1.13	62.79 $\pm$ 1.17
11	60.23 $\pm$ 1.00	62.34 $\pm$ 1.01	56.31 $\pm$ 1.08
12	81.99 $\pm$ 1.07	85.08 $\pm$ 1.08	75.93 $\pm$ 1.19
13	69.04 $\pm$ 1.35	71.86 $\pm$ 1.38	63.07 $\pm$ 1.38
14	82.83 $\pm$ 1.26	85.89 $\pm$ 1.27	76.86 $\pm$ 1.36
15	68.10 $\pm$ 1.17	71.08 $\pm$ 1.18	61.47 $\pm$ 1.24

The graph of Figure 5.17 summarises the results given in Table 5.4, representing also the group average of CBF given by each method.

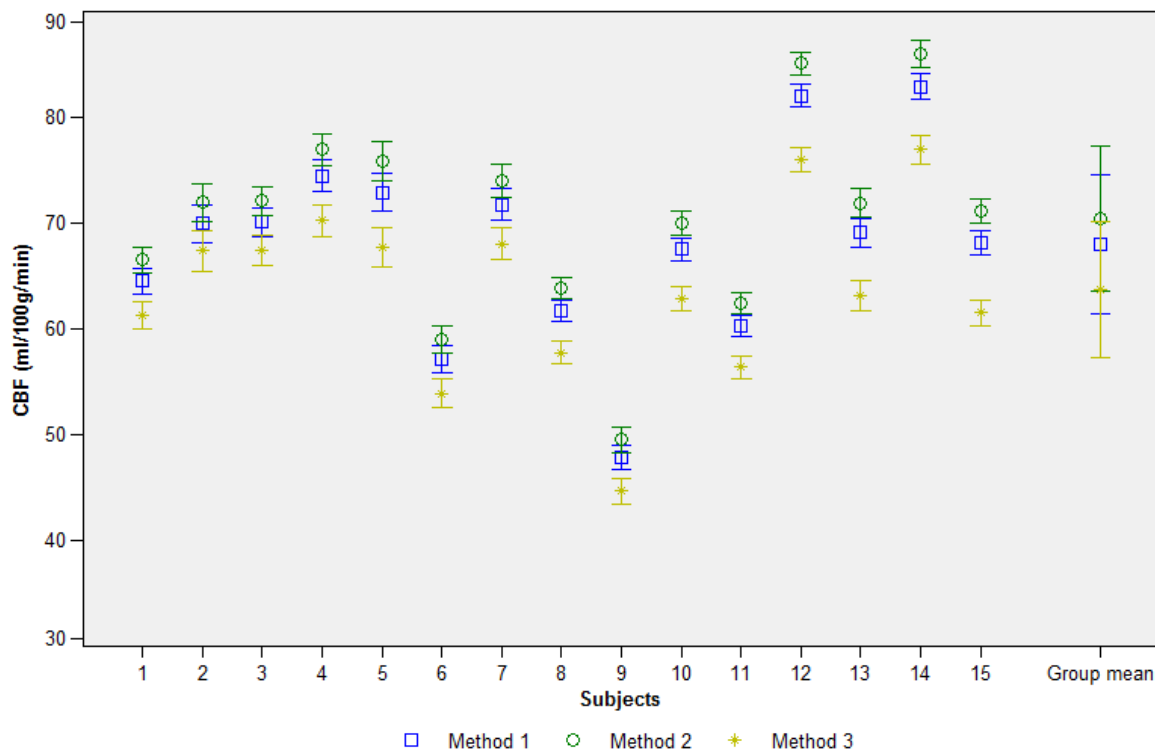


Figure 5.17: A plot of perfusion values (in  $ml/100g/min$ ) computed using the 3 methods for each subject and group mean. Error bars denote one standard error of the mean value.

As we can see in the plot of Figure 5.17, the three methods used to perform quantitative maps, provided systematically different values for CBF. For all subjects, *method 2* gave higher values of CBF



and *method 3* gave lower values of CBF in grey matter. The 95% confidence intervals of CBF mean value is [62.95 ; 72.97] ml/100g/min for *method 1*, [65.14 ; 75.57] ml/100g/min for *method 2* and [58.96 ; 68.28] ml/100g/min for *method 3*. Although there was an obvious trend, the differences in CBF values for the three methods were not significant.

Considering these results, is not surprising that we found no significant differences between the values given by the three methods, which mean that the corrections of the CBF expression parameters didn't represent great improvements on the perfusion values with respect to the original expression without any correction (*method 1*).

#### 5.4.1. Inter-slices effect

The results shown in the previous section are global values in the grey matter mask across the whole volume. In light of the type of corrections that we made, it's also important to evaluate the performance of these methods between the slices of the volumes. Considering the quantification methods used, CBF values between slices were evaluated in order to explore if there're significant differences. For ASL data, 9 slices were acquired, but only the firsts 7 slices (from the bottom) have been considered in this analysis, since the top slices only had non-brain structures (see Figure 5.18).

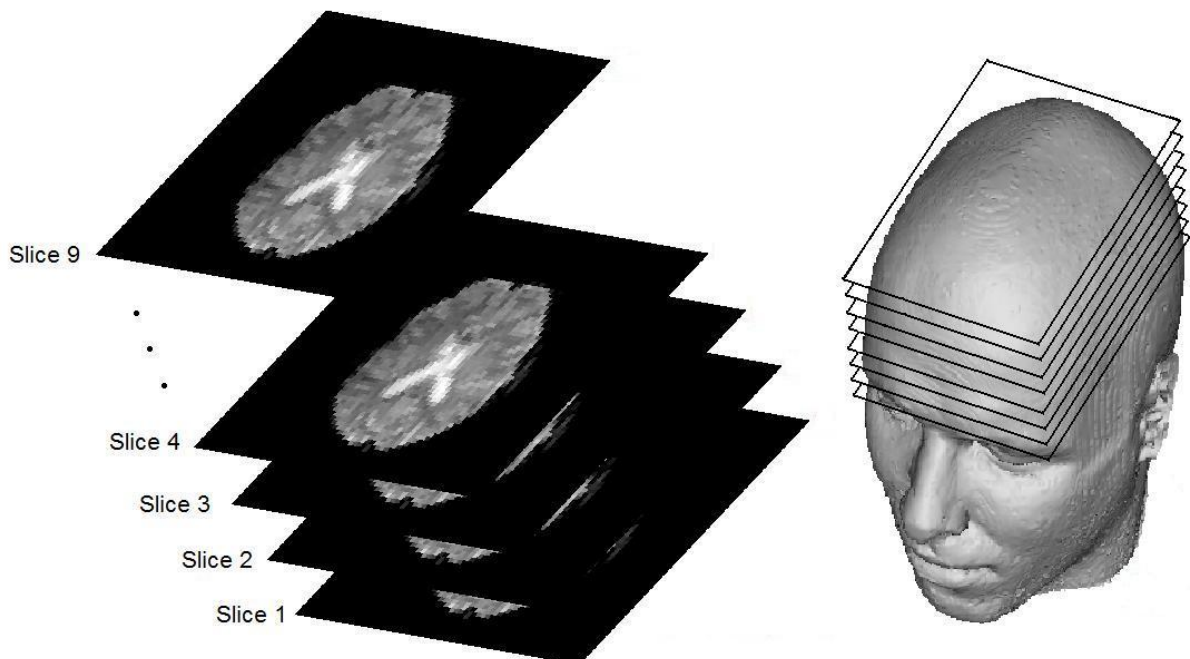


Figure 5.18: Illustration of the positions of the 9 axial slices acquired (images do not correspond to the respective positions).

The group mean values for each slice determined using each of the three maps are shown in Figure 5.19.

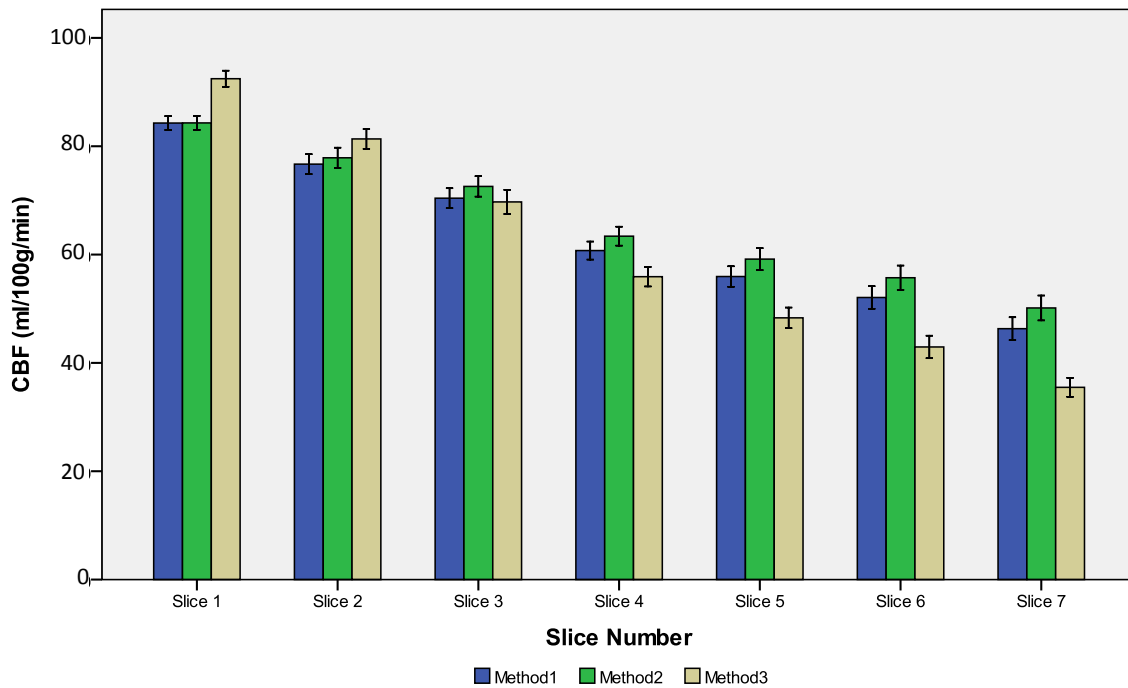


Figure 5.19: A plot of perfusion values (in ml/100g/min) across the 15 subjects calculated with the 3 methods for the firsts 7 slices. Error bars denote one standard error of the group mean.

The plot of Figure 5.19 shows some differences between slices. For all methods, a decrease of CBF values across the slices can be observed. However, the tendency of the decrease of each method is different. The results of *method 3* exhibit a more abrupt decrease across slices, while the decrease of the results of *method 2* is more gradual.

Comparing *method 1* with *method 2*, the second method accounts for the acquisition time of the different slices. In fact, the slices of the volume are not acquired at the same time. Considering the ascending acquisition order of the EPI sequence used, top slices are acquired latter than bottom slices. This effect, if not accounted, can induce some errors in CBF quantification results between slices, providing an underestimation of CBF. As expected, the CBF values of *method 2* are greater than the CBF values of *method 1*, especially for the top slices. Based on these results, we can say that *method 2* provides a good correction for CBF estimation.

*Method 3* with respect to *method 1* and *method 2*, not only accounts for the acquisition time of the slices, but also accounts for the correction factor  $q_p$ , which includes the arterial transit time. However, as we can see in Figure 5.19, the decrease of CBF values between Slice 1 and Slice 7 is more pronounced if we use *method 3*. Indeed, the percentage of decrease of CBF with *method 3* is 61.6%, while with *method 1* it is 45.04% and with *method 2* it is 40.5%. There are some reasons that explain why this happened. The most important one, however, seems to be the arterial transit time.

As mentioned before,  $q_p$  includes the transit delay of arterial blood. Since the tagged blood doesn't reach all imaging slices at the same time, we had to estimate this parameter. For this, we have considered that the transit delay of blood per centimetre of distance travelled in the z axis is 500 msec. This relation for the transit time isn't a very good assumption. Firstly, when we use this approach (considering a gap between the inversion slab and the imaging slab of 1.88 cm, and a slice spacing of approximately 1 cm), we are accepting that the time that arterial blood takes to reach the

top slice (Slice 7) is 3.94 sec. This is a very long time for tagged blood to reach brain structures. And secondly, we are considering a linear relation between the transit time and the distance that blood travelled in the z axis (see Figure 5.20a)). However, we know that this is not necessarily true: in fact, it may be a more realistic model that the transit time should be steadily shorter for the upper slices, as shown in Figure 5.20b).

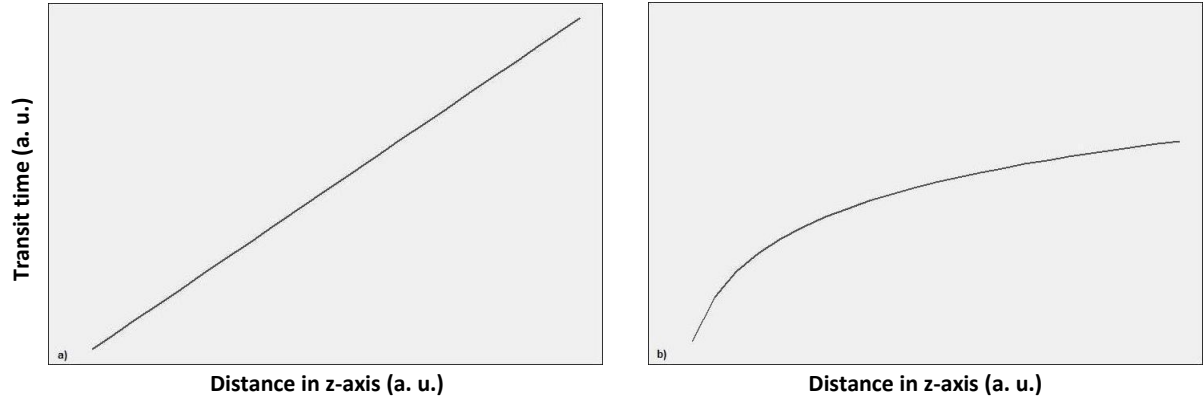


Figure 5.20: Relation between arterial blood transit time in arbitrary units (a. u.) and the distance travelled in z-axis (in a. u.): a) a linear relation that was used in the approach presented in this study, and b) a different and perhaps better approach for transit time estimation.

Thus, this linear assumption seems to be a very rude approximation to what actually happens. The mode illustrated in the graph represented in Figure 5.20b) would probably be more appropriate. Nevertheless, the brain vascular system has a complex arrangement, which precludes any accurate estimation of this local parameter. These results highlight the importance of either determining transit time as part of the PASL measurement (which is possible with a multiple  $Tl$  quantification), or knowing the approximate range of values that it is likely to take for a given application.

This may be fully understood if we consider the simulation kinetic curves represented in Figure 5.21, where the same parameters were used, except the arterial transit time variation (in this simulation we consider that the arterial transit time  $\delta t$  is 100 ms per cm of distance travelled in the z-axis).

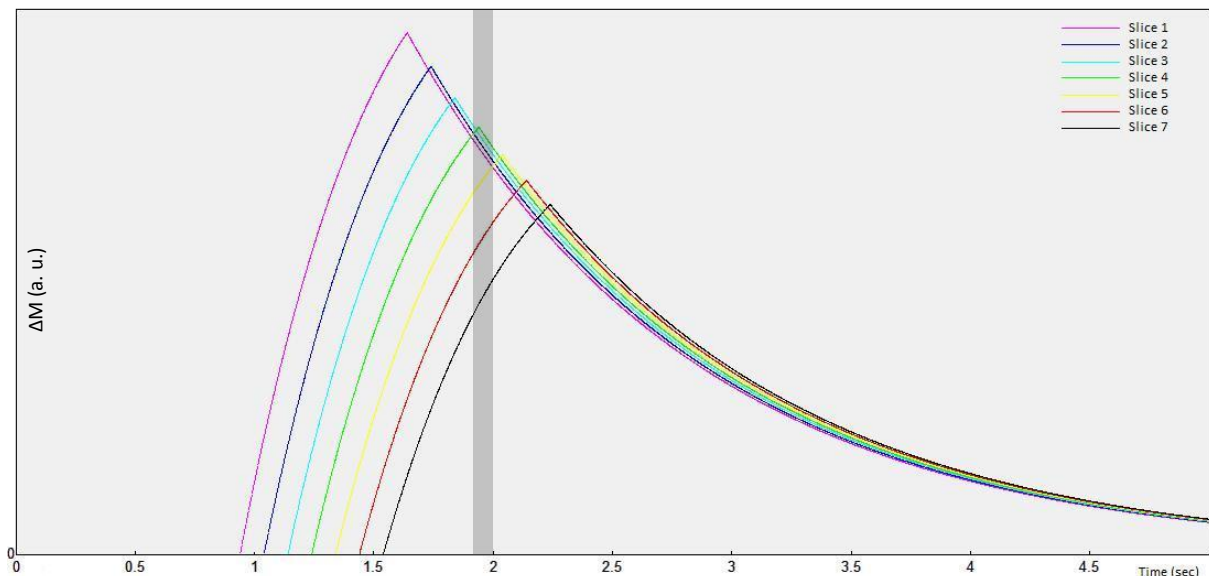


Figure 5.21: Theoretical curves of PASL signal versus time calculated from Equation 3.3. Slice acquisition effect considering a transit time variation of 100 msec per 1 cm in the z-axis. Grey vertical bar is readout time of the slices.

As it can be noticed from in Figure 5.21, the kinetic curve has not reached the descending part for all the slices at the time  $TI_2 = 1.8$  sec chosen for imaging or even considering the real time of slice acquisition. This can be confirmed by examining the mean curve across subjects for slice 6, for example (red line in Figure 5.21), where the acquisition time (1.8 sec plus correction for slice number) clearly falls on the rising portion of the curve. This means that this single  $TI$  method will consistently underestimate CBF if the assumption that the chosen  $TI$  is sufficient for acquiring the image in the descending portion of the curve is not met. In our data a consistent underestimation of CBF increasing with the slice number is observed, which can possibly be explained by the fact that the single  $TI_2$  we chose, 1.8 sec, is not long enough and the effect observed in this simulation is affecting CBF quantification.

This example evidences the importance of carefully choosing the acquisition time  $TI_2$  when designing single  $TI$  ASL experiments. Acquiring the images at a conservatively long  $TI_2$  has the disadvantage of decreasing SNR due to the decay of the control-tag difference signal. These data show that for this tagging geometry used, a  $TI_2$  of 1.8 s is sufficient for the firsts 3 – 4 slices. In higher slices, with longer arrival times (longer transit times), the proportion of the slice where the  $TI_2$  is too short is likely to increase.

In conclusion, taking into consideration the above mentioned facts, we can say that *method 2* provides a better estimation of CBF than the other 2 approaches used. Moreover, by using this method we do not need to estimate intrinsic or local parameters neither to do approximations to calculate perfusion values. In fact, as demonstrated here, those assumptions could lead to an even more erroneous estimation of CBF. Therefore, *method 2* seems to be the most accurate of these three methods, for single  $TI$  quantification with this sequence. Nevertheless, we must take into account the differences between slices, specially the higher slices, where we could be underestimating CBF. This problem, as mentioned before, could be solved with a multiple  $TI$  quantification method, which provides not only CBF but also the arterial transit time.

## 5.5. CBF quantification in Rest and Activation conditions

The data sets used for this analysis were the time-series from ASL protocols #1 and #2, in order to evaluate the feasibility of both protocols for quantifying CBF variations between the conditions of rest and activation. The method used to obtain perfusion quantitative maps was *method 2*, since it was the one which gave best results.

### 5.5.1. Comparing ASL protocols

Table 5.5 shows the CBF values calculated with both protocols for the conditions of rest and activation and the difference between CBF of activation and CBF of rest ( $\Delta CBF = CBF_{act} - CBF_{rest}$ ) in absolute unities ( $ml/100g/min$ ) for the 15 subjects.

The perfusion values presented in Table 5.5 were calculated applying the CBF activation clusters given by statistical analysis as a mask in the respective quantitative maps. It's also important to

report one more time that both protocols were conducted in each subject at the same imaging session.

Table 5.5  
CBF values provided by each protocol for both conditions of rest and activation for the 15 subjects

Subject	CBF values (ml/100g/min) calculated with ASL protocol #1			CBF values (ml/100g/min) calculated with ASL protocol #2		
	$CBF_{rest}$	$CBF_{act}$	$\Delta CBF$	$CBF_{rest}$	$CBF_{act}$	$\Delta CBF$
	1	63.4 ± 6.9	121.3 ± 9.7	57.9 ± 5.4	84.4 ± 15.7	135.8 ± 16.6
2	79.6 ± 16.4	101.9 ± 17.6	22.3 ± 2.4	90.7 ± 10.5	115.2 ± 10.3	24.6 ± 2.1
3	75.6 ± 10.7	103.8 ± 11.7	28.2 ± 2.1	84.8 ± 16.0	129.2 ± 24.1	44.5 ± 8.1
4	71.9 ± 8.3	125.4 ± 8.4	53.5 ± 4.2	89.0 ± 12.5	117.1 ± 22.8	28.2 ± 10.3
5	61.3 ± 7.1	119.2 ± 11.6	57.9 ± 5.5	71.2 ± 10.7	123.2 ± 17.1	52.0 ± 11.2
6	45.1 ± 2.7	76.2 ± 4.9	31.1 ± 4.4	43.6 ± 7.7	84.1 ± 24.1	40.6 ± 6.4
7	64.0 ± 11.4	85.4 ± 9.1	21.4 ± 4.2	79.5 ± 8.9	90.4 ± 9.3	10.9 ± 1.4
8	57.0 ± 7.8	101.1 ± 10.1	44.1 ± 3.2	59.7 ± 5.6	94.1 ± 5.9	34.4 ± 3.3
9	53.0 ± 10.1	101.9 ± 11.3	48.9 ± 2.3	56.4 ± 10.0	108.3 ± 11.4	51.9 ± 4.4
10	53.7 ± 5.2	104.3 ± 6.6	50.6 ± 2.6	81.2 ± 10.9	106.3 ± 13.8	25.2 ± 2.9
11	58.5 ± 4.6	104.8 ± 6.5	46.3 ± 3.6	56.3 ± 8.1	107.3 ± 10.3	51.0 ± 6.2
12	56.2 ± 4.9	107.3 ± 7.7	51.1 ± 5.4	63.9 ± 10.8	115.4 ± 14.6	51.5 ± 4.8
13	56.7 ± 6.1	111.9 ± 8.9	55.2 ± 5.5	76.2 ± 13.2	117.0 ± 7.5	55.1 ± 3.1
14	73.8 ± 7.3	121.2 ± 7.6	47.4 ± 2.7	66.8 ± 13.2	122.5 ± 25.2	55.7 ± 12.1
15	45.9 ± 6.3	86.0 ± 7.1	40.1 ± 2.5	52.2 ± 16.7	82.3 ± 13.8	30.1 ± 4.0
Mean (± SE)	61.0 (± 2.7)	104.8 (± 3.7)	43.7 (± 3.2)	69.4 (± 3.8)	109.9 (± 4.2)	40.5 (± 3.6)

Figure 5.22 summarises the percentage of CBF change ( $\% \Delta CBF = 100 \times (CBF_{act} - CBF_{rest}) / CBF_{rest}$ ) obtained with both protocols for the 15 subjects.

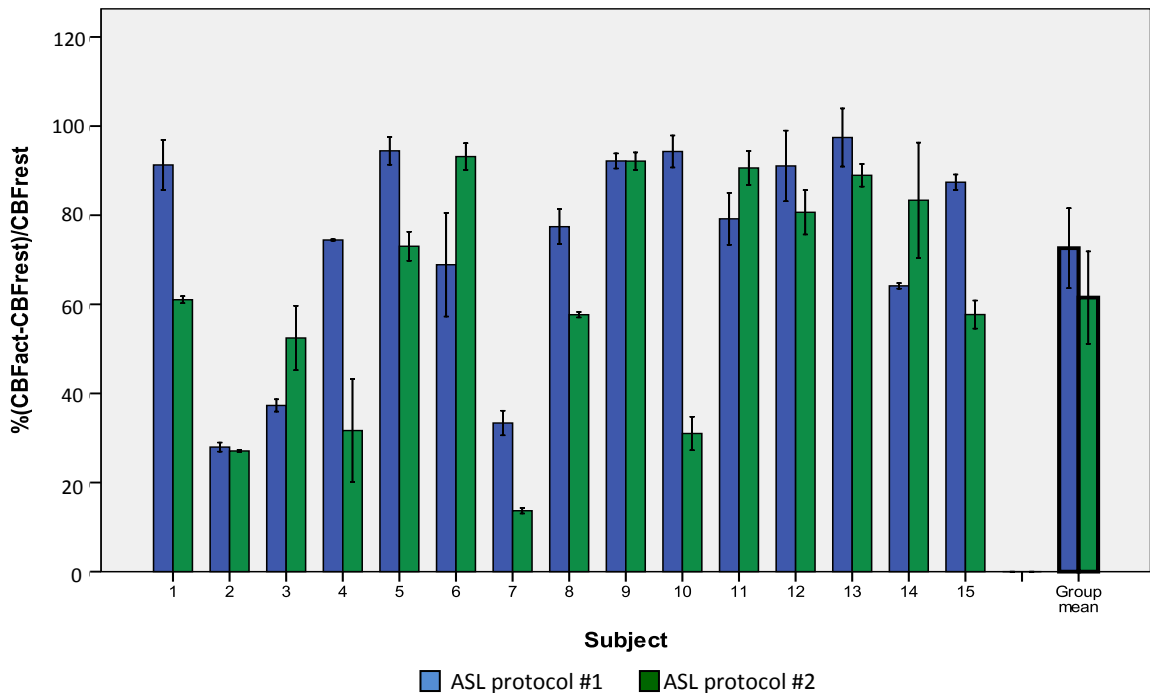
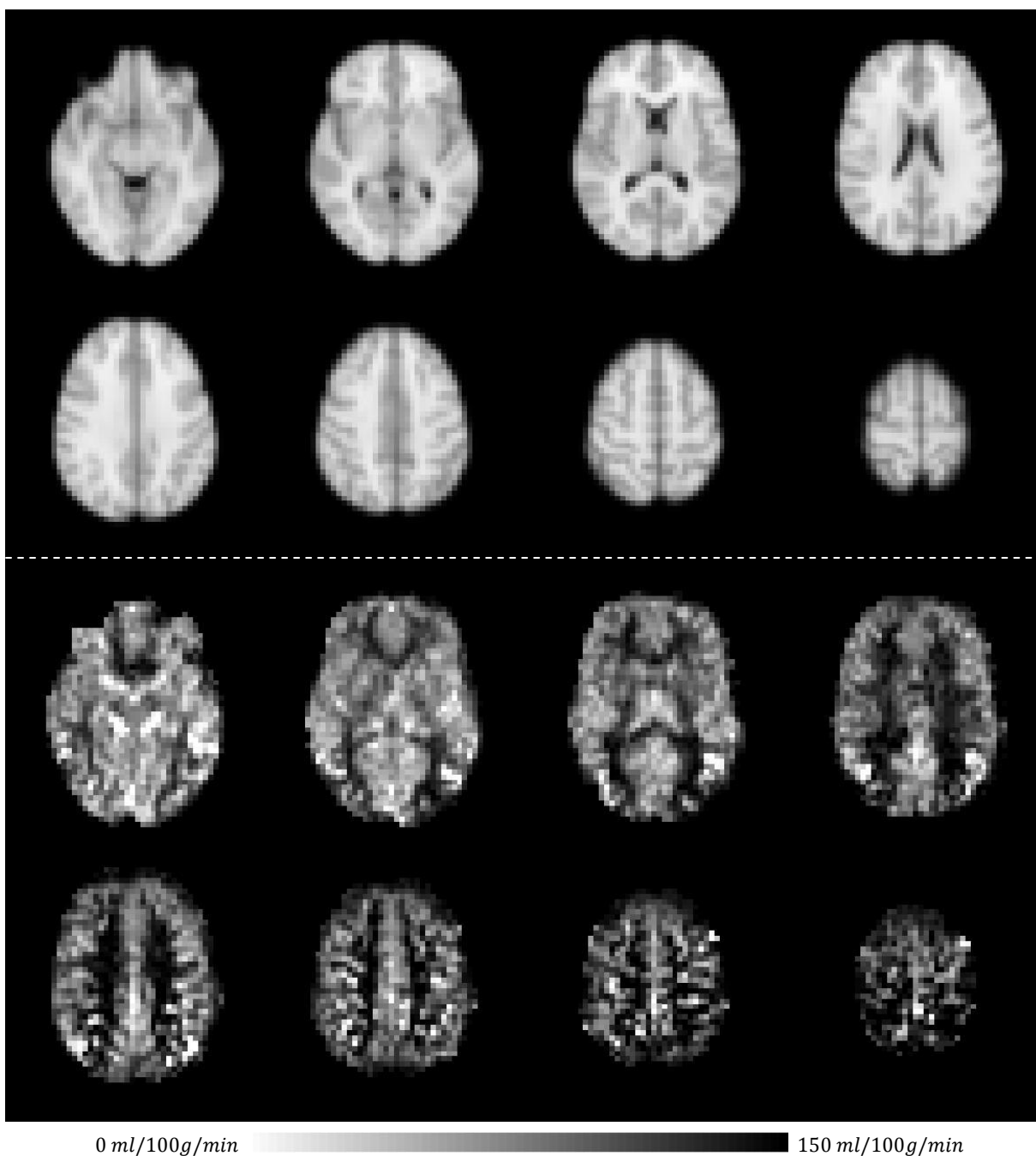


Figure 5.22: A plot of perfusion change (%) between the conditions of rest and activation. Error bars denote one standard deviation.

As we can see, motor stimulation elicited marked CBF increases in the hand motor cortex, which ranged from approximately 20% to 100% for both protocols. Indeed, in the graph of Figure 5.22, considering only the values provided by the first protocol, we can see that, the increase of CBF for Subject 2 is only 27%, while the increase of CBF for Subject 13 is 97%. There are a few reasons that explain this variability between subjects and also between protocols. According with a study carried out by A. Kastrup et al. [55], one of the most important factors that affect CBF increases during activation is the stimulation frequency. CBF was calculated during a graded motor stimulation (bilateral finger tapping at different rates), and they found that CBF increases ranged from  $32 \pm 3 \%$  (at a rate of 0.5 Hz) to  $97 \pm 8 \%$  (at a rate of 3 Hz). There are some other studies that showed that different stimulation frequencies can indeed affect CBF increases during activation [16]. In this study the stimulation frequency was not controlled, so we cannot say who performed the motor task at a higher rate.



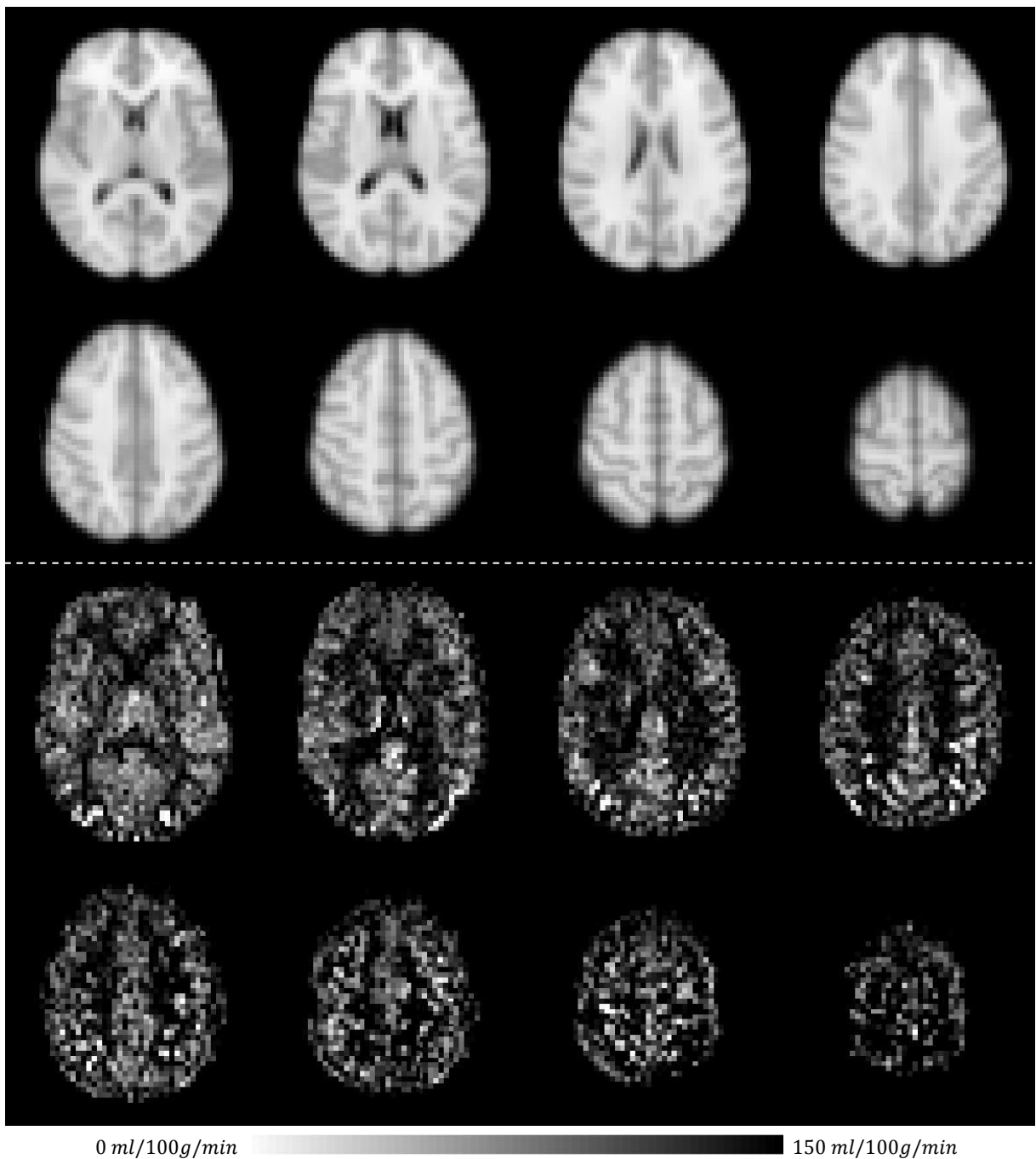


Figure 5.23: Quantitative perfusion maps (8 axial slices) provided by ASL protocols from subject 9. Firstly, the perfusion map from ASL protocol #1 and the corresponding structural image for reference (on top) are presented. Secondly, the perfusion map from ASL protocol #2 (on bottom) and also the corresponding structural image for reference are presented. Although the imaging sections are not the same for both protocols, due to the reduction of slice thickness from ASL protocol #1 to ASL protocol #2, the imaging slab covers the hand motor cortex in both cases.

Therefore it is likely that some differences observed in CBF increases between subjects might be induced by this factor, since each subject could have performed the motor task at a different rate from the others.

On the other hand, as we can see in Figure 5.22, the group mean CBF changes between both conditions were  $73 \pm 6\%$  for ASL protocol #1 and  $62 \pm 7\%$  for ASL protocol #2. We found no significant difference between the group mean values provided by both protocols, although the mean value given by the second protocol was 10% lower. These results showed that both protocols

were capable to detect variations in CBF according to the stimulus, and the results from the first and the second protocol were consistent. However, we must attend to the inferior SNR of the data while considering ASL protocol #2 to quantify CBF changes. In fact, Figure 5.23 shows the quantitative perfusion-weighted images provided by each protocol from a 27 year-old male subject. As we can see, the image provided by the second protocol is noisier and has a worse quality than the image provided by the first protocol. The SNR issues of these two images are discussed in the next section.

### 5.5.2. SNR of perfusion-weighted images

Figure 5.24 shows the group mean SNR of perfusion-weighted images provided by ASL protocol #1 and ASL protocol #2.

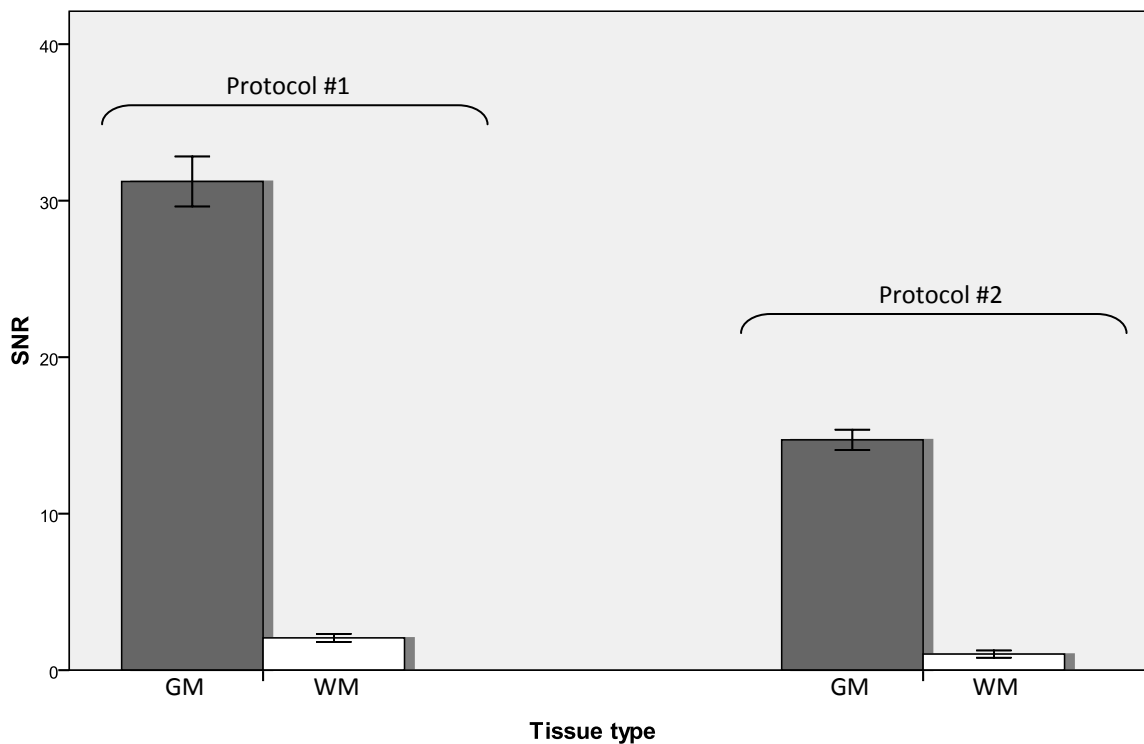


Figure 5.24: A plot of the group mean SNR of grey matter (GM) and white matter (WM) calculated for both protocols. Error bars denote one standard error of the mean.

As expected, the mean grey matter perfusion SNR (31.2) calculated for ASL protocol #1 images was found to be significantly higher ( $p < 0.01$ ) than the corresponding grey matter perfusion SNR (14.7) obtained for ASL protocol #2 images. For the white matter perfusion-weighted images from ASL protocol #1, the mean perfusion SNR (2.1) was also significantly higher ( $p < 0.01$ ) than the corresponding mean value (1.0) from ASL protocol #2 images. These differences can be easily explained. We know that SNR increases in proportion to voxel volume ( $vox$ ) and to the square root of the number of acquisitions ( $N_{aq}$ ):

$$SNR \propto \sqrt{vox \times N_{aq}}$$



In fact, if we average several measurements of the signal, SNR will increase because we are in presence of white noise and its random contributions will tend to cancel out. That is what happens in this case. In fact, the voxel volume from ASL protocol #1 ( $128 \text{ mm}^3$ ) is larger than the voxel volume from ASL protocol #2 ( $73.5 \text{ mm}^3$ ), which means that SNR from ASL protocol #2 images should be lower. In addition, the number of measurements averaged to perform the quantitative perfusion maps from ASL protocol #1 was higher, 90, than the number of volumes used to obtain the quantitative perfusion maps from ASL protocol #2, 50 (see Figure 5.25). According to the SNR equation, an improvement of 1.55 in the SNR from protocol #2 to protocol #1 is expected. The ratio of the measured SNR values in grey matter, between protocols #1 and #2, is actually 2.12. The greater than expected difference in the SNR could be due to the alternation between rest and activation periods in protocol #2, which may have introduced additional sources of variances in the signal, as will be further discussed next.

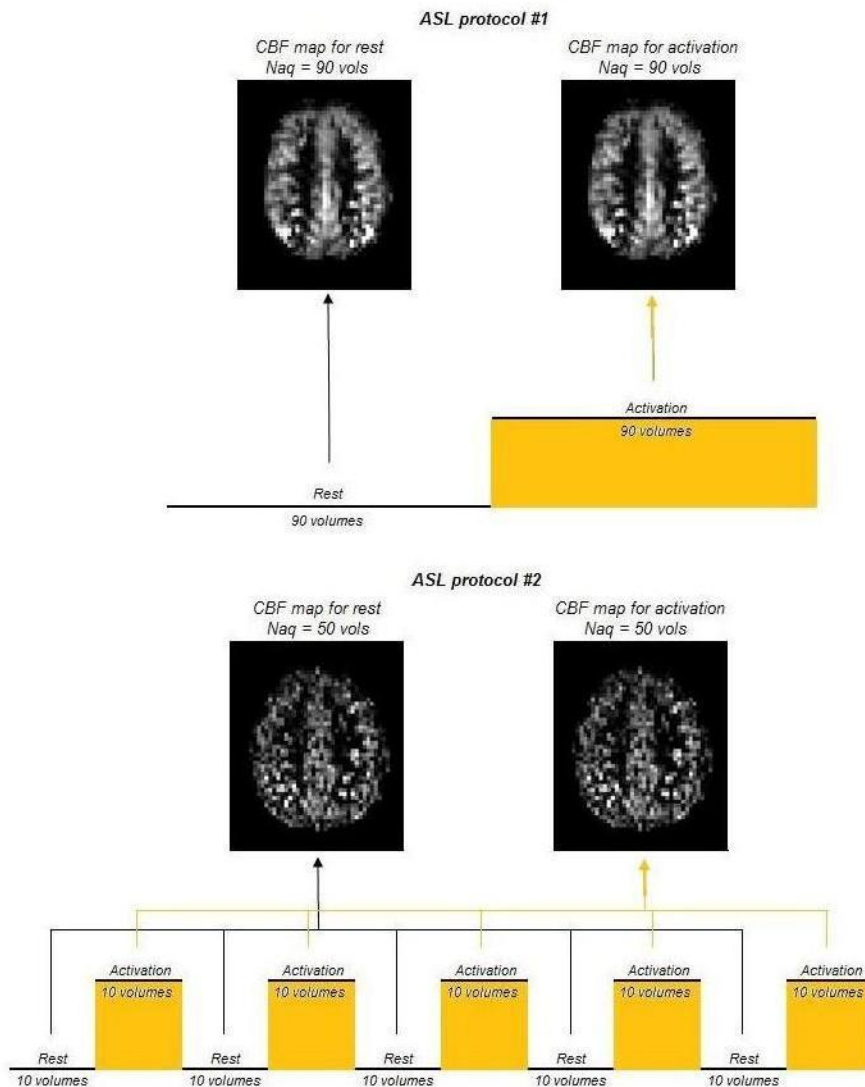


Figure 5.25: A schematic diagram for the assessment of the perfusion maps of each functional protocol. Perfusion maps from ASL protocol #1 were obtained by the average of 90 measurements, while perfusion maps from ASL protocol #2 were achieved by the average of 50 measurements.

Therefore, although both ASL protocols allow the detection of perfusion signal change, the second protocol gives perfusion images with a lower SNR, which means that the background noise can

obtrude the desired signal with more impact and induce some errors in CBF quantification. So, it can be in the origin of the differences observed between the perfusion changes (%) given by both protocols. This factor can also be seen as a criterion for image quality, and is able to justify the worse quality of the images provided by ASL protocol #2 (see Figure 5.23). On the other hand, ASL protocol #2 provides images with better spatial resolution (thinner slices).

As a final point, there is one other important vindication that could explain why the mean  $\% \Delta CBF$  from ASL protocol #2 was lower than the corresponding mean value from ASL protocol #1. To perform the quantitative perfusion maps from the second protocol we had to concatenate the images from the rest blocks and the images from the activation blocks. However, the nature of the block design of this time-series (in this case, 5 blocks on and 5 blocks off) precludes any accurate division, i.e., in some cases the rest blocks or the activation blocks could have 11 or 12 volumes instead of the exactly 10 measurements considered. This would result in a lower mean signal change, which was what really happened. To avoid this we could select only fewer images from the middle of each block to concatenate, but this would result in a worse SNR of the resultant perfusion-weighted images. With ASL protocol #1 we don't have this problem because we acquired one single series of images in rest, and one single series of images in activation, so the images were already divided.

In conclusion, ASL protocols #1 and #2 were able to detect CBF changes between rest and activation conditions which ranged from 20 % to 98 %. The differences between both protocols consist in some aspects that have to be considered in the optimization of this functional protocol. Considering the SNR of perfusion-weighted images, it is important to define the number of volumes/repetitions acquired in each block, which impinges directly on the acquisition time (if we acquire more volumes, the acquisition time will rise), the slice thickness and the field of view, which directly affect the spatial resolution of the image (if we have larger voxel volumes, we'll loss image's spatial resolution).

## 5.6. CBF quantification: effect of anterior and posterior circulation

Figure 5.26 shows the position of ROIs 1 and 2 in each of the seven slices from a representative subject (Subject 3).

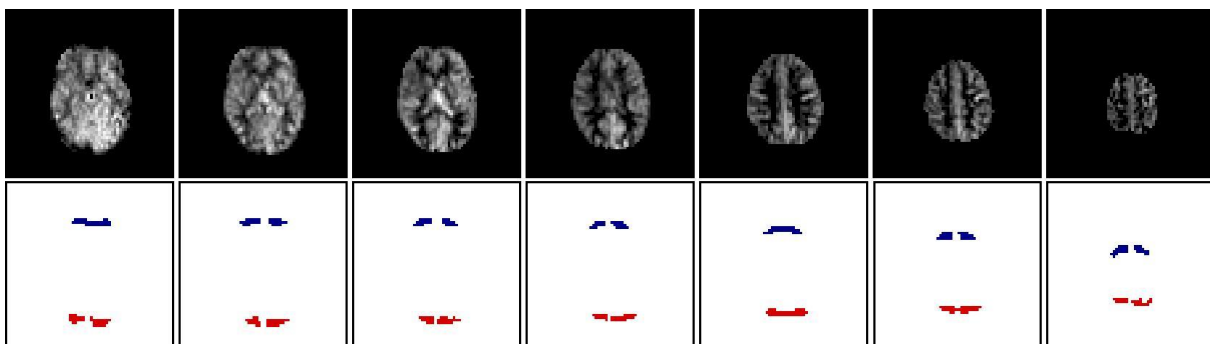


Figure 5.26: Position of ROI 1 and ROI 2. Top images show the mean control-tag difference images of the firsts seven slices (from right to left, slice 1 to slice 7) from subject 3. Bottom images show ROI 1 (blue) and ROI 2 (red) for each slice.

Figure 5.27 summarises the CBF values achieved to both ROIs in each slice using method 2.

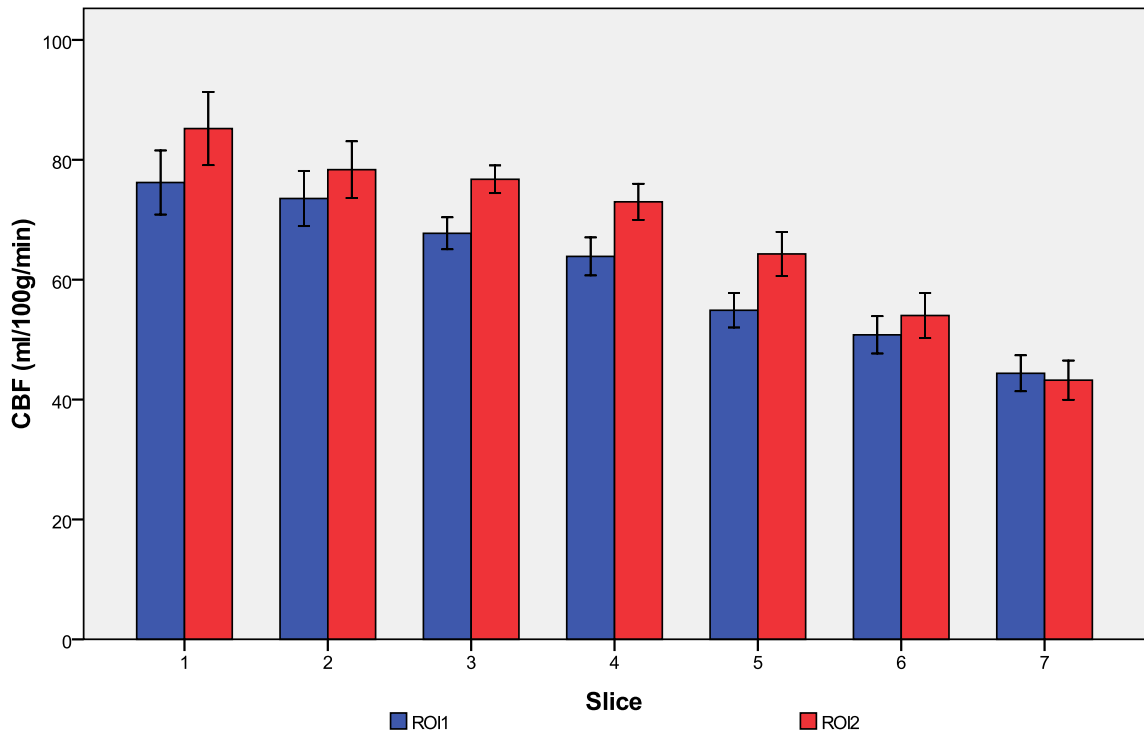


Figure 5.27: A plot of the group mean CBF values (in ml/100g/min) for each slice. Error bars denote one standard error from the mean.

The CBF values calculated for both ROIs in each slice were found to be close, i. e., there's no significant difference between CBF values in ROI 1 and ROI 2. As we can see, the decrease of CBF values across the slices observed in early section 5.4.1 is observed here as well. However, we also see that, excepting slice 7, in all slices the CBF estimate values to ROI 1 are lower than the CBF values found to ROI 2. Indeed, the CBF estimate for ROI 2 is on average 9.8% ( $\pm 2.2\%$ ) higher than for ROI 1.

These differences can be explained by several aspects. The first one, and perhaps the most important, is the fact that the arrival times of blood to occipital and frontal regions could be different. Wong et al. [56] demonstrates that transit times vary across different regions of the brain, and Figueiredo et al. [5] have demonstrated maps of the tag arrival time. Namely, Gallichan et al. [57, 58] found that the arrival times in the occipital region are longer than for the frontal region. The differences in the arrival time occur due to the brain vascular anatomy (anterior and posterior circulation).

In the analysis presented in this study, where we used a single  $T_{I_2}$  quantification, we didn't account for this factor, which is the same to say that we assumed a single transit time for both ROIs, which has been found to be not true. So, even if we consider just one slice for the analysis, the transit time seems to play an important role and can induce some errors in CBF quantification. In addition, previous works have indicated that the  $T_1$  of tissue is expected to vary across the brain, which introduces one more source of error. On the other hand, these small discrepancies may be partly explained by the various definitions of ROIs in the 15 subjects and also by differences in slice coverage. In literature, an atlas of predefined ROIs with the posterior and anterior circulation wasn't found, so we had to draw by hand 30 ROIs for each of the seven slices.

In conclusion, CBF differences between ROI 1 and ROI 2 were found, mainly due to possible differences in the arterial transit time, or incorrect definitions of both ROIs. These facts suggest that it might be useful to build an atlas of normal values of both parameters for a range of ROIs predefined in standard space. Upon scanning a new subject, this would allow a quick determination of regions where the CBF or arrival times deviate from the normal range.

### 5.7. CBF quantification in GM and WM

A typical perfusion image from a 26-year-old female subject and the corresponding GM and WM binary masks obtained are shown in Figure 5.28.

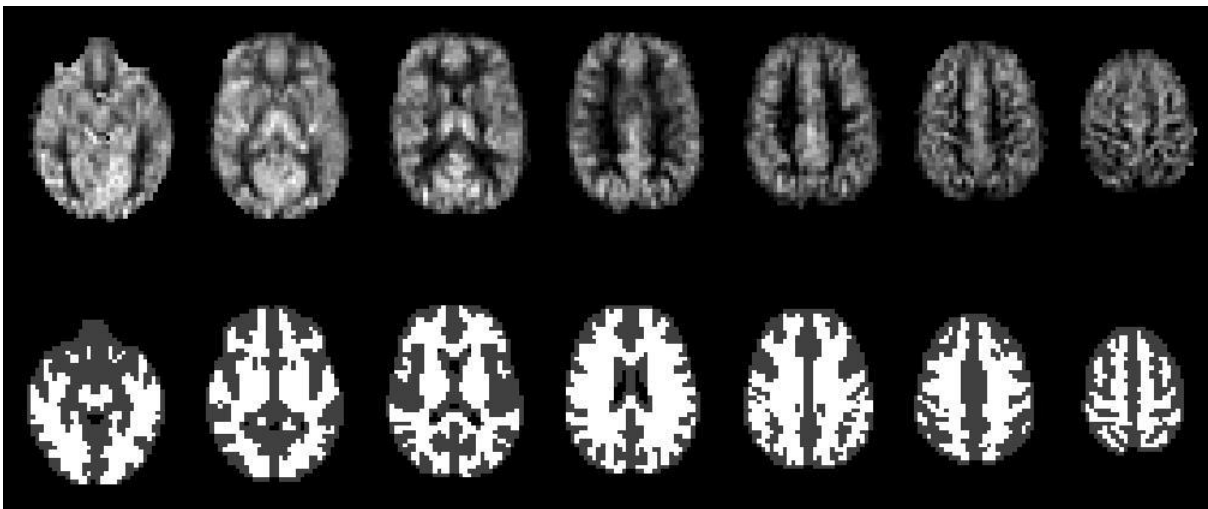


Figure 5.28: Representation of the grey matter (GM) and white matter (WM), automatically segmented, binary masks. Top images show the mean control-tag difference, perfusion-weighted images of the firsts seven slices (from right to left, slice 1 to slice 7) from subject 12. Bottom images show the GM (grey) and WM (white) masks.

The increased perfusion in grey matter compared to white matter can be clearly seen in the images shown before. The mean perfusion estimate of the voxels in each segmented region was calculated for each subject using the binary GM and WM masks. Figure 5.29 shows these results.

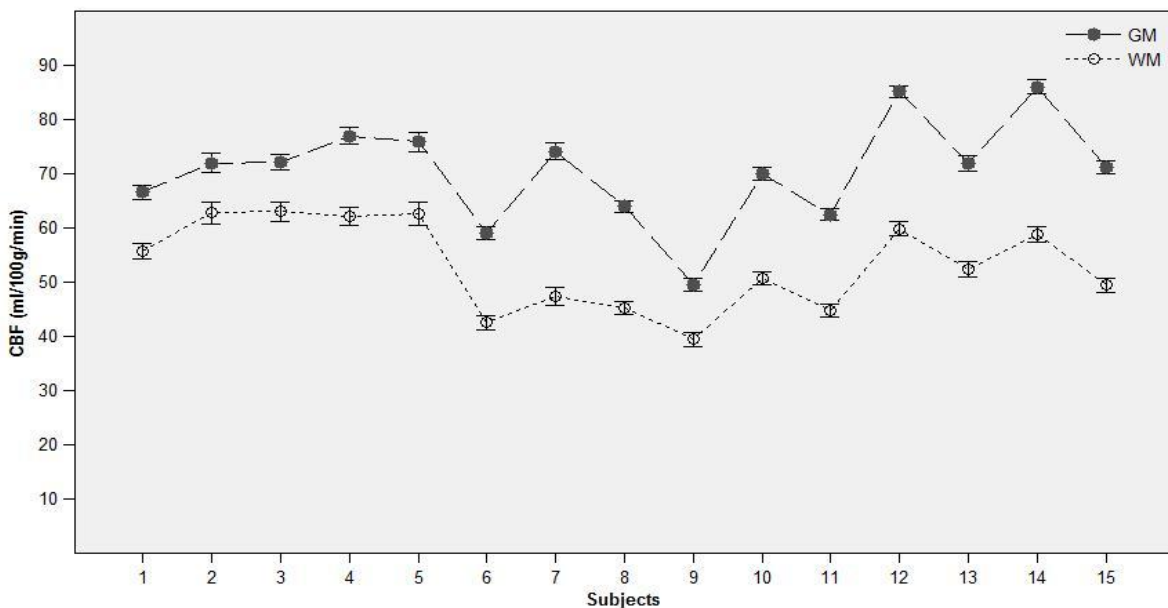


Figure 5.29: A plot of CBF values (ml/100g/min) in automatically segmented grey and white matter masks for each subject.

The mean WM perfusion ( $53.0 \pm 8.1 \text{ ml } 100 \text{ g}^{-1} \text{ min}^{-1}$ ) was found to be significantly lower ( $p < 0.05$ ) than the mean GM perfusion ( $70.4 \pm 9.4 \text{ ml } 100 \text{ g}^{-1} \text{ min}^{-1}$ ). However, although the mean grey matter perfusion values fall within the expected range, as measured by a variety of techniques, the mean white matter perfusion values were too large relative to the expected. In fact, for GM the average perfusion value across the 15 subjects was  $70.4 \text{ ml } 100 \text{ g}^{-1} \text{ min}^{-1}$  with a range of  $49.4 - 85.9 \text{ ml } 100 \text{ g}^{-1} \text{ min}^{-1}$ , and for WM it was  $53.0 \text{ ml } 100 \text{ g}^{-1} \text{ min}^{-1}$  with a range  $39.3 - 62.9 \text{ ml } 100 \text{ g}^{-1} \text{ min}^{-1}$ . Additionally, the mean ratio of grey to white matter perfusion ( $CBF_{GM}/CBF_{WM}$ ) achieved, which reflects how much the perfusion in GM is higher than the perfusion in WM, was 1.3, confirming the small difference between the perfusion in both tissues ( $17.3 \pm 4.7 \text{ ml } 100 \text{ g}^{-1} \text{ min}^{-1}$ ). According with literature [1], this ratio has been found to be in a range of 2.5 – 3.0.

These results can be easily explained by partial volume and segmentation effects. There isn't a fine and single segmentation algorithm that allows an accurate segmentation of the brain in the classes that we want. Although we have segmented the brain in only three classes (GM, WM and CSF), segmentation errors are inevitable. This segmentation procedure is even more problematic if applied in a low resolution image as are the images provided by ASL. Furthermore, it can bring on significant partial volume effects, which if not considered, can induce important errors in CBF quantification of both tissues type, especially with large voxel volumes. In this analysis we used the binary masks provided by FAST, which don't account for this outcome.

### 5.7.1. Partial volume effect correction

The partial volume effect (PVE) is the effect wherein insufficient image resolution leads to a mixing of different tissue types within a voxel, i.e., each voxel of the images can represent more than one tissue type. To compensate for this effect, we tried to use the partial volume maps (see Figure 5.30) from FAST and calculate the real grey and white matter perfusion (since there's no CSF perfusion) using the following approach:

$$\begin{cases} \langle f \rangle_{GMmask} = \langle pve_{GM} \rangle_{GMmask} f_{GM} + \langle pve_{WM} \rangle_{GMmask} f_{WM} \\ \langle f \rangle_{WMmask} = \langle pve_{GM} \rangle_{WMmask} f_{GM} + \langle pve_{WM} \rangle_{WMmask} f_{WM} \end{cases} \quad \text{Equation 5.1}$$

where  $\langle f \rangle_{GMmask}$  and  $\langle f \rangle_{WMmask}$  are the mean values of CBF in GM and WM binary masks, and  $\langle pve_{GM} \rangle_{GMmask}$ ,  $\langle pve_{WM} \rangle_{GMmask}$ ,  $\langle pve_{GM} \rangle_{WMmask}$ ,  $\langle pve_{WM} \rangle_{WMmask}$  are the mean values of the GM and WM *pve\_maps* in GM and WM binary masks, and  $f_{GM}$  and  $f_{WM}$  are the CBF values of the GM and WM respectively.

Solving Equation 5.1 in order to  $f_{GM}$  and  $f_{WM}$  we reached to the following expression:

$$\begin{cases} f_{WM} = \frac{\langle f \rangle_{WMmask} \langle pve_{GM} \rangle_{GMmask} - \langle f \rangle_{GMmask} \langle pve_{GM} \rangle_{WMmask}}{\langle pve_{WM} \rangle_{WMmask} \langle pve_{GM} \rangle_{GMmask} - \langle pve_{WM} \rangle_{GMmask} \langle pve_{GM} \rangle_{WMmask}} \\ f_{GM} = \frac{\langle f \rangle_{GMmask} - \langle pve_{WM} \rangle_{GMmask} f_{WM}}{\langle pve_{GM} \rangle_{GMmask}} \end{cases} \quad \text{Equation 5.2}$$

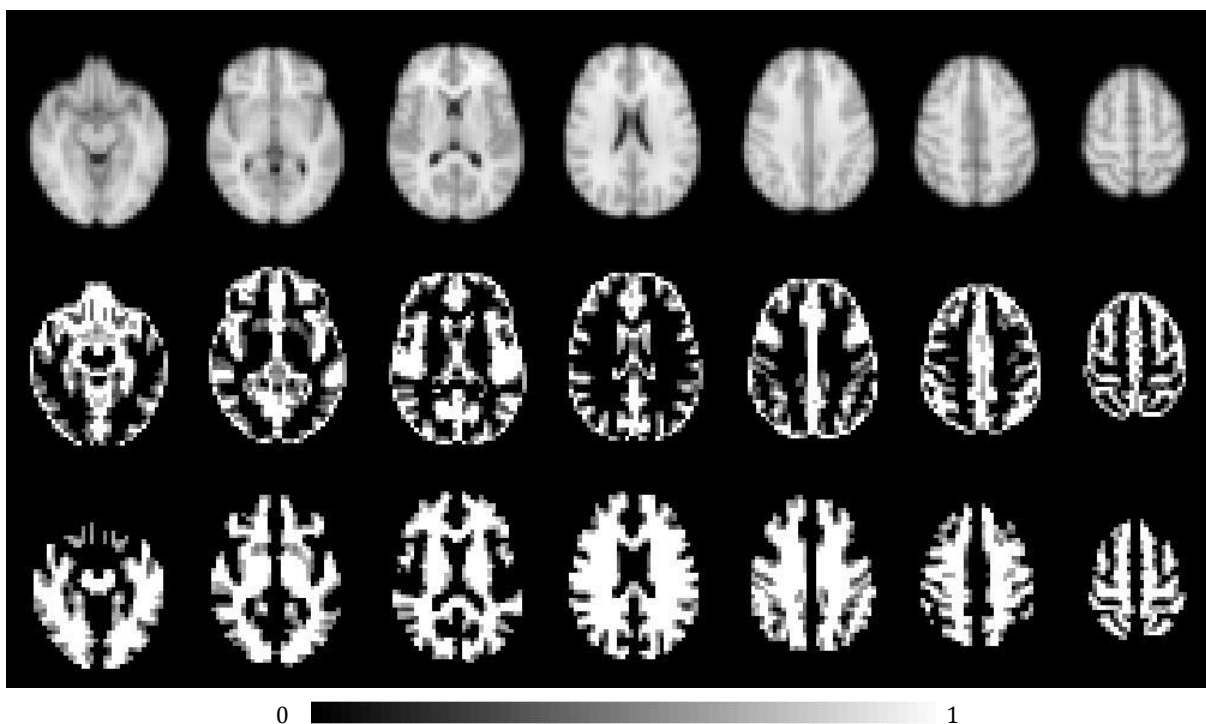


Figure 5.30: Representation of the grey matter (GM) and white matter (WM) partial volume maps. Top images show the anatomic images of the first 7 slices (from right to left, slice 1 to slice 7) from subject 12. Middle images show the corresponding GM partial volume map and bottom images show corresponding WM partial volume map.

Equation 5.2 was then computed to calculate the new grey and white matter perfusion values. These results are shown in Figure 5.31.

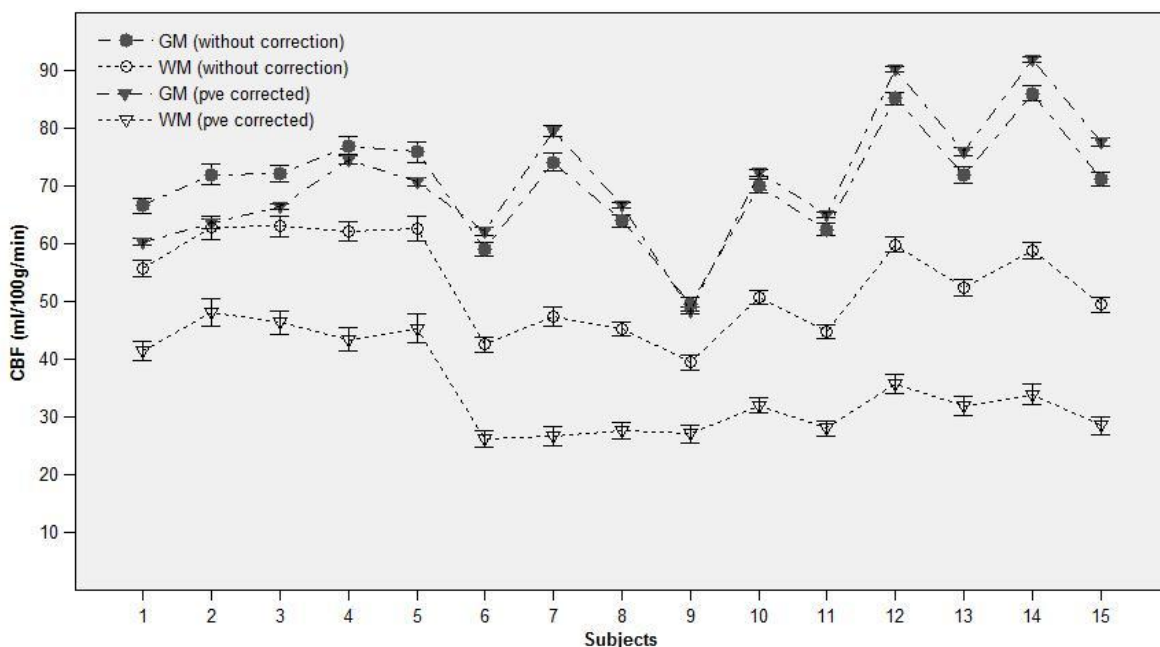


Figure 5.31: A plot of CBF values (in  $ml/100g/min$ ) of grey and white matters for each subject with and without partial volume effects correction.

Table 5.6 summarises the results presented in Figure 5.31.

Table 5.6  
 Mean CBF values in  $ml/100g/min$  in GM and WM calculated with and without partial volume effects (PVE) correction

	CBF values ( $ml/100g/min$ ) calculated without PVE correction in		CBF values ( $ml/100g/min$ ) calculated with PVE correction in	
	Grey matter	White matter	Grey matter	White matter
Group mean	70.4	53.0	70.8	$34.7 \pm 8.0$
$\pm SD$	9.4	8.1	11.3	8.0
$\frac{CBF_{GM}}{CBF_{WM}}$	$1.3 \pm 0.1$		$2.1 \pm 0.5$	

As we can see, the results show significant perfusion changes with this partial volume effect correction. White matter perfusion was found to decrease 34.5%, which is in agreement with the expected. Besides, the ratio of grey to white matter perfusion increases from 1.3 to 2.1, demonstrating a closer to expected difference between the mean perfusion values of both tissue types. However, this still is a small value if we compare it to the values found in other studies. If we look closer to the images represented in Figure 5.30, it's reasonable to think that FAST segmentation performance performed differently across the 7 axial slices. Indeed, in the lower sections, the presence of deep grey matter structures limits an accurate segmentation: those structures are in fact often erroneously classified as white matter. One example of this imprecise procedure is considering the basal ganglia. On the other hand, top slices nearly don't have brain structures, so the performance of segmentation isn't too good. This will result in an overestimation of white matter perfusion. To confirm this observation the group mean ratios of grey to white matter perfusion were calculated for each slice. Figure 5.32 shows these results.

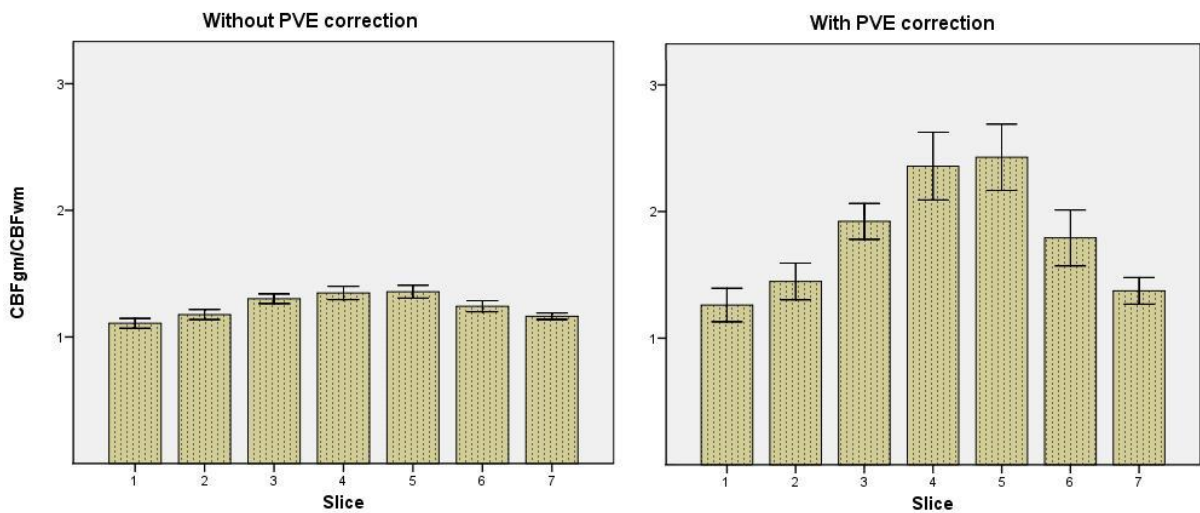


Figure 5.32: A plot of the mean ratios of grey to white matter perfusion in each of 7 slices calculated with (right) and without (left) partial volume effects correction.

As we can see in the right graph of Figure 5.32, the ratio of grey to white matter perfusion is quite different if we consider, for example, slice 1 or slice 5. For slice 5 the ratio value is closer to the expected range of values (2.5 – 3.0), which confirms our previous observation. Furthermore, the

graphs of Figure 5.32 also show the real differences between GM and WM perfusion with and without PVE correction. In summary, an accurate segmentation (in the middle slices) allows for partial volume effects to be corrected, yielding an expected grey to white matter perfusion ratio. However, where grey matter structures are classified as white matter (bottom slices), white matter perfusion is overestimated and therefore the grey to white matter perfusion ratio is underestimated.

Despite this, it is interesting and reasonable to compare the SDs of the perfusion values, which represent the inter-subject spread in perfusion. Some studies [6, 59, 60] have reported higher SDs for GM than for WM perfusion, which supports the present finding that GM perfusion variation between individuals is large. Although the cause of this variation stills unknown, it could be linked to individual variation in neuronal density [61] or neuron number [62], which are found to have a similarly large inter-subject variability. Individual differences in excitability levels during the scanning could also account for some of the perfusion differences seen in this study.



## Chapter 6

### Conclusions

#### 6.1. Discussion

In general, the study presented in this thesis accomplishes its principal objectives: provides the first results of the commercially available ASL sequence from *Siemens* implemented in the *Hospital da Luz*; contains some good approaches for functional validation of ASL technique with BOLD contrast; and includes some important quantification lines for clinical support. This work also accounted for the analysis and optimisation of the functional ASL protocol, and the evaluation of its potential to provide quantitative values of CBF. From these analyses, a few conclusions may be taken.

Firstly, ASL protocol #1 should not be used for functional studies. As mentioned in the previous chapter, this protocol precludes an accurate activation detection because it does not employ an efficient stimulation paradigm. In fact, with this protocol we acquired one series of images in a rest state, and after a while, we acquired another in an activation state. Thus, we are not actually measuring the CBF changes that result from the alternating states of rest and activation, but only a simple difference in CBF between one state and another, which might give an erroneous result for functional studies.

And secondly, we have demonstrated that the optimised functional ASL protocol #2 can replicate and produce better results for this kind of approaches, providing not only the CBF activation but also the BOLD contrast, which is an additional measure within the same setup. For clinical applications this functional protocol might be useful because it combines the better spatial specificity of ASL fMRI with the higher detection sensitivity of BOLD fMRI, and grants CBF quantification results of both baseline and activation states, which were found to be consistent with literature and previous results (with the initial functional protocol). Besides, the reduction of the acquisition time (by a factor close to 2) from the original protocol to this new one is another advantage that must be considered: it enables less motion artefacts and more comfort for the subject.

Some of the different quantification approaches made in this work may be questioned. Yet, the results attained support the importance of considering some parameters on CBF quantification, namely the arterial transit time, and how they can influence the results if erroneous assumptions were made. Furthermore, our results revealed the importance of performing an accurate segmentation in order to achieve correction of partial volume effects. In fact, we showed that this can significantly influence grey matter and white matter perfusion values. Although some tissue classification errors are still present in the segmentation procedures used in the present study, the

slices where a correct classification was possible clearly show a substantial improvement in the accuracy of the perfusion measures obtained. It has therefore been illustrated that the partial volume effects should be accounted for in this kind of analysis. The approach used here seems to be a good correction method for these effects, since it provided more accurate results.

Although the results in this work are very interesting, there were a number of factors that were not considered, and can be in the origin of some of the differences and discrepancies observed in this study. The original conditions of each subject before and during the respective imaging session could be different. For example, the imaging sessions weren't all conducted in the same period of the day, neither in the same day of the week. Some studies have confirmed that these factors are able to affect brain perfusion values [6]. Even caffeine intake can affect CBF values.

In conclusion, the main potentials and drawbacks of ASL perfusion imaging technique in brain activation studies have been demonstrated. Overall, in spite of some difficulties in arranging the fifteen imaging sessions due to the anticipated and common clinical schedule, the work was carried out as expected, and didn't present any great problem that should be mentioned.

## 6.2. Future prospects

This first study provided some results for the clinical validation of functional ASL techniques. Yet, this validation for functional MRI should proceed by performing many other functional studies using different paradigms and different stimulations (visual, auditory, word generation, etc). Other tests with fMRI should be performed in order to analyse the reproducibility of ASL results.

Also, CBF values calculated with the single  $TI$  quantification method used in this work should be compared to the CBF values obtained with the multiple  $TI$  quantification method, which provides the arterial transit time as well and can more accurately quantify CBF in different regions of the brain. One approach using this multiple  $TI$  method [63], has already been carried out in the end of this work. In addition, dynamic susceptibility contrast MRI could be used to cross-validate the perfusion values from ASL.

One important clinical drawback of ASL is the fact that it does not provide CBV measurements. However, there is one technique called vascular space occupancy (VASO) that can be combined with ASL and provide simultaneously CBF and CBV [64].

Finally, as mentioned, some physiological factors potentially affecting perfusion values were not considered in this work. In future studies, a control for at least some of these factors should be made.

## Bibliography

1. Buxton, R.B., *Introduction to functional magnetic resonance imaging: principles and techniques*. 2002: Cambridge University Press.
2. Moonen, C.T.W. and P.A. Bandettini, *Functional mri*. 1999: Springer Verlag.
3. Golay, X. and E.T. Petersen, *Arterial spin labeling: benefits and pitfalls of high magnetic field*. Neuroimaging Clinics of North America, 2006. **16**(2): p. 259-268.
4. Tjandra, T., et al., *Quantitative assessment of the reproducibility of functional activation measured with BOLD and MR perfusion imaging: Implications for clinical trial design*. NeuroImage, 2005. **27**(2): p. 393-401.
5. Figueiredo, P.M., S. Clare, and P. Jezzard, *Quantitative perfusion measurements using pulsed arterial spin labeling: effects of large region-of-interest analysis*. Journal of magnetic resonance imaging: JMRI, 2005. **21**(6): p. 676.
6. Parkes, L.M., et al., *Normal cerebral perfusion measurements using arterial spin labeling: reproducibility, stability, and age and gender effects*. Magnetic Resonance in Medicine, 2004. **51**(4).
7. Petersen, E.T., et al., *Non-invasive measurement of perfusion: a critical review of arterial spin labelling techniques*. British Journal of Radiology, 2006. **79**(944): p. 688.
8. Kandel, E.R., J.H. Schwartz, and T.M. Jessell, *Principles of neural science*. 2000: Appleton & Lange.
9. Crossman, A.R. and D. Neary, *Neuroanatomy: an illustrated colour text*. 2000: Elsevier Health Sciences.
10. Yousry, T.A., et al., *Localization of the motor hand area to a knob on the precentral gyrus. A new landmark*. Brain, 1997. **120**(1): p. 141.
11. Magistretti, P.J. and L. Pellerin, *Cellular mechanisms of brain energy metabolism and their relevance to functional brain imaging*. Philosophical Transactions: Biological Sciences, 1999. **354**(1387): p. 1155-1163.
12. Shulman, R.G., et al., *Energetic basis of brain activity: implications for neuroimaging*. Trends in neurosciences, 2004. **27**(8): p. 489-495.
13. Van Bruggen, N. and T.P.L. Roberts, *Biomedical imaging in experimental neuroscience*. 2003: CRC.
14. Wintermark, M., et al., *Comparative overview of brain perfusion imaging techniques*. 2005, Am Heart Assoc.
15. Taber, K.H., K.J. Black, and R.A. Hurley, *Blood flow imaging of the brain: 50 years experience*. 2005, Am Neuropsych Assoc. p. 441-446.
16. Feng, C.M., et al., *CBF changes during brain activation: fMRI vs. PET*. Neuroimage, 2004. **22**(1): p. 443-446.

17. Wong, E.C., R.B. Buxton, and L.R. Frank, *Implementation of quantitative perfusion imaging techniques for functional brain mapping using pulsed arterial spin labeling*. NMR in Biomedicine, 1997. **10**.
18. Prasad, P.V., *Magnetic resonance imaging: methods and biologic applications*. 2005: Humana Pr Inc.
19. Brown, G.G., et al., *A primer on functional magnetic resonance imaging*. Neuropsychology Review, 2007. **17**(2): p. 107-125.
20. Wansapura, J.P., et al., *NMR relaxation times in the human brain at 3.0 tesla*. Journal of magnetic resonance imaging: JMRI, 1999. **9**(4): p. 531.
21. Liu, T.T. and G.G. Brown, *Measurement of cerebral perfusion with arterial spin labeling: Part 1. Methods*. Journal of the International Neuropsychological Society, 2007. **13**(03): p. 517-525.
22. Hertz-Pannier, L., et al., *IRM fonctionnelle cérébrale: bases physiologiques, techniques et méthodologiques, et applications cliniques*. Journal de radiologie(Paris), 2000. **81**(6): p. 717-730.
23. Le Bihan, D., *Functional MRI of the brain principles, applications and limitations*. Journal of neuroradiology, 1996. **23**(1): p. 1-5.
24. Matthews, P.M. and P. Jezzard, *Functional magnetic resonance imaging*. 2004, Journal of Neurology Neurosurgery and Psychiatry. p. 6-12.
25. FMRI, *FMRI Centre: Introduction to FMRI*, <http://www.fmrib.ox.ac.uk/education/fmri/introduction-to-fmri>. Assessed at: March, 12th of 2009.
26. Vazquez, A.L. and D.C. Noll, *Nonlinear aspects of the BOLD response in functional MRI*. NeuroImage, 1998. **7**(2): p. 108-118.
27. Yang, Y., *Perfusion MR imaging with pulsed arterial spin-labeling: basic principles and applications in functional brain imaging*. Concepts in Magnetic Resonance, 2002. **14**(5).
28. Wolf, R.L. and J.A. Detre, *Clinical neuroimaging using arterial spin-labeled perfusion magnetic resonance imaging*. Neurotherapeutics, 2007. **4**(3): p. 346-359.
29. Detre, J.L., *Perfusion imaging*. Magnetic Resonance in Medicine, 1992. **23**(1): p. 37-45.
30. Williams, D.S., et al., *Magnetic resonance imaging of perfusion using spin inversion of arterial water*. Proceedings of the National Academy of Sciences, 1992. **89**(1): p. 212-216.
31. Sorensen, A.G. and P. Reimer, *Cerebral MR perfusion imaging: principles and current applications*. 2000: Thieme.
32. Edelman, R.R., et al., *Qualitative mapping of cerebral blood flow and functional localization with echo-planar MR imaging and signal targeting with alternating radio frequency*. Radiology, 1994. **192**(2): p. 513.
33. Kim, S.G., *Quantification of relative cerebral blood flow change by flow-sensitive alternating inversion recovery (FAIR) technique: application to functional mapping*. Magnetic Resonance in Medicine, 1995. **34**(3).
34. Wong, E.C., R.B. Buxton, and L.R. Frank, *Quantitative perfusion imaging using arterial spin labeling*. Neuroimaging Clinics of North America, 1999. **9**(2).
35. Østergaard, L., et al., *High resolution measurement of cerebral blood flow using intravascular tracer bolus passages. Part I: Mathematical approach and statistical analysis*. Magnetic resonance in medicine, 1996. **36**(5).
36. Buxton, R.B., et al., *A general kinetic model for quantitative perfusion imaging with arterial spin labeling*. Magnetic Resonance in Medicine, 1998. **40**(3).

37. Wong, E.C., R.B. Buxton, and L.R. Frank, *Quantitative imaging of perfusion using a single subtraction (QUIPSS and QUIPSS II)*. Magnetic Resonance in Medicine, 1998. **39**(5).
38. Luh, W.M., et al., *QUIPSS II with thin-slice T11 periodic saturation: a method for improving accuracy of quantitative perfusion imaging using pulsed arterial spin labeling*. Magnetic Resonance in Medicine, 1999. **41**(6).
39. Wang, J., et al., *Arterial spin labeling perfusion fMRI with very low task frequency*. Magnetic Resonance in Medicine, 2003. **49**(5): p. 796-802.
40. Warmuth, C., M. Gunther, and C. Zimmer, *Quantification of Blood Flow in Brain Tumors: Comparison of Arterial Spin Labeling and Dynamic Susceptibility-weighted Contrast-enhanced MR Imaging 1*. 2003, RSNA. p. 523-532.
41. van Laar, P.J., J. van der Grond, and J. Hendrikse, *Brain perfusion territory imaging: methods and clinical applications of selective arterial spin-labeling MR imaging*. Radiology, 2008. **246**(2): p. 354.
42. Kemeny, S., et al., *Comparison of continuous overt speech fMRI using BOLD and arterial spin labeling This article is a US Government work and, as such, is in the public domain in the United States of America*. Human brain mapping, 2005. **24**(3).
43. Yang, Y., et al., *Multislice imaging of quantitative cerebral perfusion with pulsed arterial spin labeling*. Magnetic Resonance in Medicine, 1998. **39**(5).
44. Herscovitch, P. and M.E. Raichle, *What is the correct value for the brain-blood partition coefficient for water*. J Cereb Blood Flow Metab, 1985. **5**(1): p. 65-69.
45. Deibler, A.R., et al., *Arterial spin-labeling in routine clinical practice, part 1: technique and artifacts*. American Journal of Neuroradiology, 2008. **29**(7): p. 1228.
46. Karger, N., et al., *Quantitation of renal perfusion using arterial spin labeling with FAIR-UFLARE*. Magnetic resonance imaging, 2000. **18**(6): p. 641-647.
47. Mai, V.M. and S.S. Berr, *MR perfusion imaging of pulmonary parenchyma using pulsed arterial spin labeling techniques: FAIRER and FAIR*. Journal of Magnetic Resonance Imaging, 1999. **9**(3).
48. FMRIB, *FMRIB's software analysis (FSL)*, <http://www.fmrib.ox.ac.uk/fsl>. Assessed at: April, 16th of 2009.
49. Smith, S.M., et al., *Advances in functional and structural MR image analysis and implementation as FSL*. Neuroimage, 2004. **23**: p. 208-219.
50. Francis, S.T., R. Bowtell, and P.A. Gowland, *Modeling and optimization of look-locker spin labeling for measuring perfusion and transit time changes in activation studies taking into account arterial blood volume*. Magnetic Resonance in Medicine, 2008. **59**(2).
51. Kleinschmidt, A., M.F. Nitschke, and J. Frahm, *Somatotopy in the human motor cortex hand area. A high-resolution functional MRI study*. European Journal of Neuroscience, 1997. **9**(10): p. 2178-2186.
52. Zhu, X.H., et al., *Simultaneous oxygenation and perfusion imaging study of functional activity in primary visual cortex at different visual stimulation frequency: Quantitative correlation between BOLD and CBF changes*. Magnetic Resonance in Medicine, 1998. **40**(5).
53. Restom, K., et al., *Cerebral blood flow and BOLD responses to a memory encoding task: A comparison between healthy young and elderly adults*. Neuroimage, 2007. **37**(2): p. 430-439.
54. Huppert, T.J., et al., *A temporal comparison of BOLD, ASL, and NIRS hemodynamic responses to motor stimuli in adult humans*. Neuroimage, 2006. **29**(2): p. 368-382.
55. Kastrup, A., et al., *Changes of cerebral blood flow, oxygenation, and oxidative metabolism during graded motor activation*. Neuroimage, 2002. **15**(1): p. 74-82.

56. Liu, T.T. and E.C. Wong, *A signal processing model for arterial spin labeling functional MRI*. Neuroimage, 2005. **24**(1): p. 207-215.
57. Gallichan, D. and P. Jezzard, *Variation in the shape of pulsed arterial spin labeling kinetic curves across the healthy human brain and its implications for CBF quantification*. Magnetic Resonance in Medicine, 2009. **61**(3).
58. Gallichan, D. and P. Jezzard, *Modeling the effects of dispersion and pulsatility of blood flow in pulsed arterial spin labeling*. Magnetic Resonance in Medicine, 2008. **60**(1).
59. Leenders, K.L., et al., *Cerebral blood flow, blood volume and oxygen utilization: normal values and effect of age*. Brain, 1990. **113**(1): p. 27.
60. Schreiber, W.G., et al., *Cerebral blood flow and cerebrovascular reserve capacity: estimation by dynamic magnetic resonance imaging*. Journal of Cerebral Blood Flow & Metabolism, 1998. **18**(10): p. 1143-1156.
61. Henderson, G., B.E. Tomlinson, and P.H. Gibson, *Cell counts in human cerebral cortex in normal adults throughout life using an image analysing computer*. Journal of the neurological sciences, 1980. **46**(1): p. 113.
62. Pakkenberg, B. and H.J.G. Gundersen, *Neocortical neuron number in humans: effect of sex and age*. The Journal of Comparative Neurology, 1997. **384**(2).
63. Sousa, I., J. Sanches, and P. Figueiredo. *Sampling strategy for perfusion quantification using PASL*. in *ESMRMB 2009 Congress*. 2009. Turkey: ESMRMB.
64. Yang, Y., H. Gu, and E.A. Stein, *Simultaneous Acquisition of Blood Volume, Blood Flow and Blood Oxygenation Information During Brain Activation*.

## Appendix A

### Appendix

#### A.1. BOLD-ASL fusion in Neuro3D

The procedure to perform the fusion between the perfusion-weighted images from ASL and the statistical map given by BOLD in Neuro3D is described below.

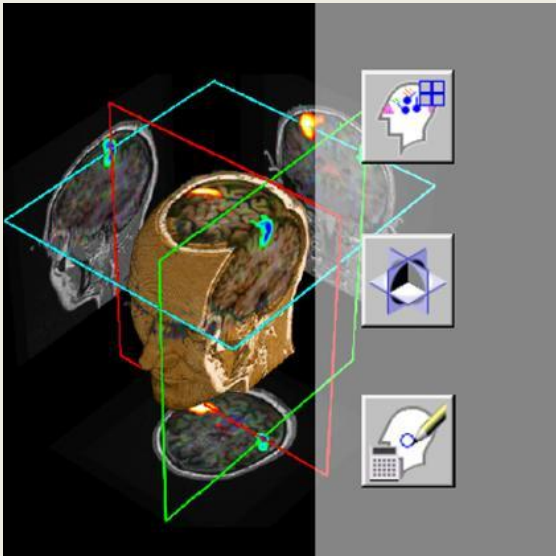
### Image Fusion

---

**ASL + BOLD fMRI**

Operation task cards used:

- Neuro3D
- 3D
- VIEWER



---

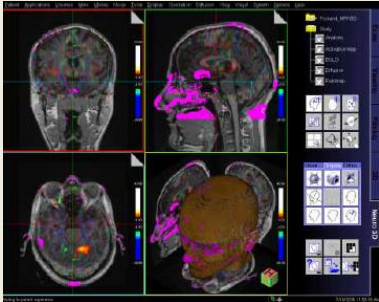
#### Stage 1

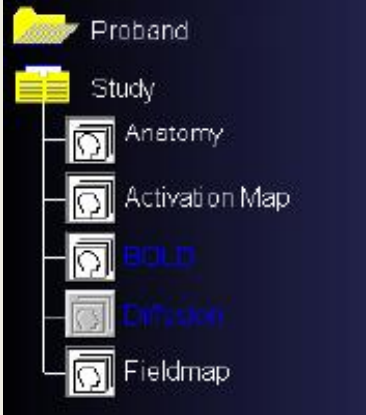
---

**Step 1**

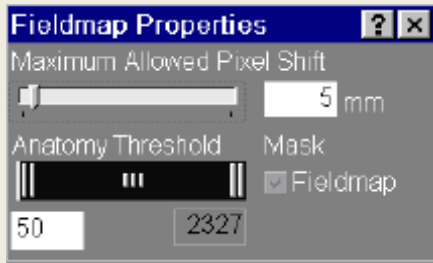
- ✚ Begin with Neuro3D module.
- ✚ Firstly, load MPRAGE series, which corresponds to the anatomic structural image.
- ✚ Load EvaSeries\_GLM, which corresponds to the functional image (activation map from BOLD).

- ✚ The volumes loaded can always be seen in the folder *Study*.
- ✚ In this case, three volumes have been loaded.

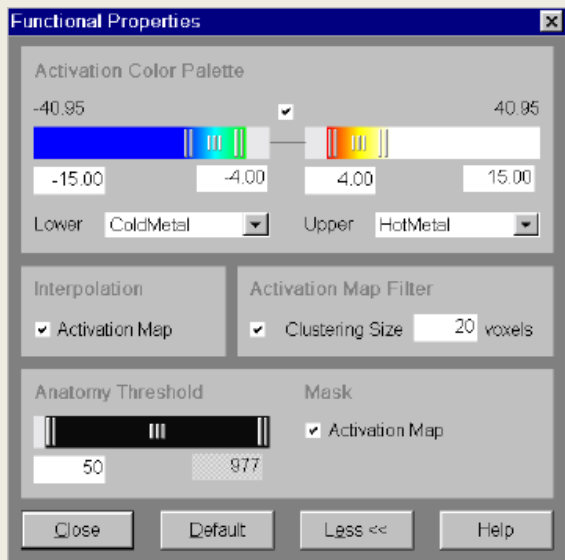




- The field map is loaded automatically with EvaSeries\_GLM.
- For a better optimisation of the relevant images visualisation, the field map should be disabled, or the Anatomy threshold (in Fieldmap Properties) should be adjusted.



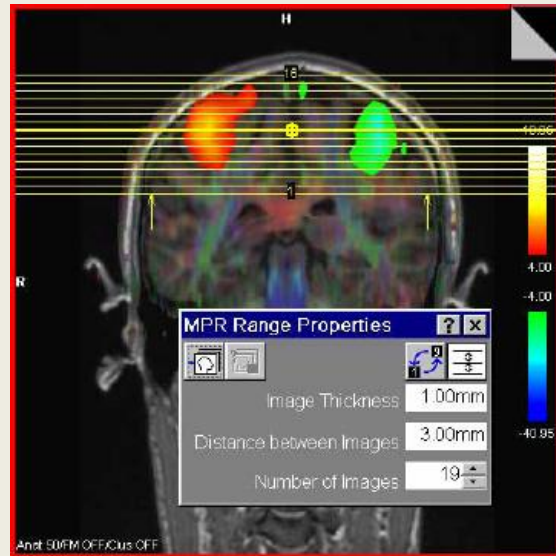
- Clicking in Functional Properties, the following window is displayed.



- A number of parameters can be changed:
- In Activation Color Palette, the colour of both positive and negative BOLD signals can be controlled, as the lower and upper thresholds of the t-value.
- A smoothing can be applied in the images using the Interpolation tool.
- In activation Map Filter the clustering size is chosen. 20 is the default value.
- In Anatomy Threshold the lower limit can be adjusted.

**Step 2**

- Click in MPR Range.
- This tool allow the generation of parallel images in a predefined plane.



- In the properties window of this tool, the number of images, its thickness and the distance between two consecutive images can be chosen.
- Click in the button
- The images are generated and appear in fourth window in the right inferior corner of the monitor.
- Save the series of images by clicking on and giving a name to it.



**Step 3**

- ✚ Preserving the previous definitions of MPR Range (same positions and same parameters), load relCBF which corresponds to the perfusion-weighted image from ASL.
- ✚ The software will interpret this image as an activation map (i. e. as a functional image), so automatically the previous activation map is removed.
- ✚ In Functional Properties a number of parameters can be altered (like Step 1).

- ✚ In Activation Color Palette the colour of both positive and negative relCBF signals can be controlled, as the lower and upper thresholds of the t-value. In this case, the lower limit should be set to none.
- ✚ The other parameters have already been discussed.
- ✚ In MPR Range Properties, generate and save the new series of images.
- 💡 In this study, this step was performed for both relCBF maps corresponding to the condition of resting and to the condition of activation.

**Stage 2**

**Step 4**

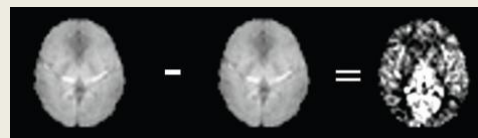
- ✚ In VIEWER module, the series of images achieved can be visualised.
- ✚ In this study, three series were generated:

Original series	EvaSeries_GLM	relCBF	relCBF
Generated series	BOLD (functional)	ASL (rest)	ASL (activation)

- ✚ To convert the images to a conventional grey scale, begin for selecting the series.
- ✚ Click in Save As, and save the series again with other name.
- ✚ Then select the two same series and click in Evaluation → Dynamic Analysis → Arithmetic Mean.
- ✚ After this procedure, a new equal series is generated, but in a grey scale.
- ✚ This procedure was performed for the 3 series.

**Step 5**

- ✚ To perform the image difference between CBF in activation and CBF in resting state begin for selecting the two perfusion ASL maps created.
- ✚ Click in Evaluation → Dynamic Analysis → Subtraction.
- ✚ In the opened window, take into consideration the subtraction order (Act-Rep).
- ✚ Click in Scaling, and set the minimum value to zero.
- ✚ A new series corresponding to the subtraction of the previous series is created.



- ✚ To perform the image fusion, the two relevant series created (the BOLD series and the subtraction image) to the MEDPC.

**Stage 3**

- ✚ In MEDPC load the BOLD series to the 3D module.
- ✚ In the Patient list select the two series and click in Application → 3D → Fused.
- ✚ In Fusing Definition MPR, the properties of the fused images can be defined.
- ✚ In this study the properties chosen were:



- ✚ Create and save a new series of images with MPR Range, similar to step 2.

## A.2. Quantification maps Shell Script routine

The routine called *Quantification\_maps* was performed in shell script *Linux* to make the quantification analysis simpler. It allows the construction of quantitative perfusion maps based on each of the three methods used in this study. The inputs needed for this script is the original time series of alternated control-tag images, the corresponding brain binary mask (that's used to remove non-brain structures) and the grey matter binary mask to calculate M0. It allows also the change of the quantification parameters.

In the box bellow, a small part of this Shell Script routine built to perform the perfusion quantification maps is represented.

```

# Routine Quantification_maps #

#!/bin/sh
# ** Script Organisation
# *** Perfusion maps performing from time series ASL
# **** Perfusion quantification
# ***** Inputs: time-series with alternated control-tag images

# function Usage: how to use this script
Usage(){
  echo ""
  echo "Usage:  Quantification_maps <input_volume_4D> <brain_epi_mask> <GM_mask>"
  echo ""
  exit 1;
}

# function OUT: exit program
OUT(){
  echo ""
  echo ""
  echo Done
  echo ""
  exit 1;
}

# function MENU: displays the list of options
MENU(){
  echo ""
  echo Choose your Mode:
  echo ""
  echo "*****"
  echo "***** MENU *****"
  echo "*****"
  echo "* Mode[1] Mode [2] Mode[3] Exit[4] *"
  echo ""
  echo " [1]: Simple Wang expression without any correction "
  echo ""
  echo " [2]: Wang expression with readout time correction "
  echo ""
  echo " [3]: Buxton expression          "
  echo ""
  echo " [4] Exit "
  echo ""
  echo "*****"
  echo ""
}

```

```

# {{{ validation of input
if [ $# -ne 1 ]; then
    Usage;
elif [ ! -e $1 -o ! -f $1 ]; then
    echo ""
    echo "File $1 does not exist or is not a regular file"
    Usage;
else
    # {{{ get dimensions, i.e, get the values and put them on variables that are used below
    filename=`fslval $1 dim1`;
    nvols=`fslval $1 dim4`;
    nslices=`fslval $1 dim3`;
    # }}}
fi
# }}}

# {{{ function signal difference: considering the 4D data, the first volume is deleted and then it's performed the
# subtraction of Control - Tag signals to obtain the mean signal (delta_M)
fslsplit $1; # split 4D data
rm vol0000.nii.gz;
# performing the subtraction of Control - Tag signals
F=1;
while [ $F -lt $nvols ]; do
    if [ $F -lt 10 ]; then
        fslmaths vol000$F -mul -1 vol000$F -odt float;
    else
        fslmaths vol00$F -mul -1 vol00$F -odt float;
    fi
    F=`echo "$F+2" | bc`;
done
# Creation of new time series
fslmerge -t asl_new vol00*.nii.gz;
# Subtraction and Mean of time series
fslmaths asl_new -Tmean -mul 2 ${filename}_mean -odt float ;
# }}}

# {{{ acquire M0 value
fslmerge -t asl_control vol00*[02468].nii.gz
fslmaths asl_control -Tmean image_control -odt float;
fslmaths image_control.nii.gz -mas brain_epi_mask.nii.gz M_0_image -odt float
M0_image="M_0_image.nii.gz";
fslmaths ${M0_image}.nii.gz -mas GM_mask.nii.gz M0_image_GM -odt float
# }}}

# {{{ remove all files which are useless
rm asl_control.nii.gz;
rm vol00*.nii.gz;
rm asl_new.nii.gz;
rm image_control.nii.gz;
# }}}

# {{{ function Quantification: perform the perfusion quantification map (simple map)
Mode="9";
until [ $Mode = "4" ]; do
    MENU;
    printf "Mode: "
    read Mode;
    if [ $Mode = "3" ]; then
        echo Default values T11 T12 T1a lambda alfa
        lambda=0.9;
        echo lambda = $lambda ml/g
        alfa=0.9;
        echo a = `echo "$alfa*100" | bc` %
        T11=0.7;
        echo T11 = `echo "$T11*1000" | bc` ms
    fi
done

```

```

TI2=1.8;
echo TI2 = `echo "$TI2*1000" | bc` ms
T1a=1.5;
echo T1a = `echo "$T1a*1000" | bc` ms
T1=1.2;
echo T1 = `echo "$T1*1000" | bc` ms
deltat=0.5;
echo deltat = `echo "$deltat*1000" | bc` ms

n=0;
while [ $n = "0" ]; do
    printf "Change parameters? <y/n> "
    read resp
    if [ $resp = "y" -o $resp = "n" ]; then
        n=1;
    fi
done

if [ $resp = "y" ]; then
    printf "lambda= "
    read lambda
    echo $lambda | grep "[^0-9]"
    if [ $lambda=`echo "\n ####" -o "$?" -eq "0" `]; then
        lambda=0.9;
    fi

    printf "alfa= "
    read alfa
    echo ""
    echo $alfa | grep "[^0-9]"
    if [ $alfa=`echo "\n ####" -o "$?" -eq "0" `]; then
        alfa=0.9;
    fi

    printf "T11= "
    read T11
    echo ""
    echo $T11 | grep "[^0-9]"
    if [ $T11=`echo "\n ####" -o "$?" -eq "0" `]; then
        T11=0.7;
    fi

    printf "TI2= "
    read TI2
    echo ""
    echo $TI2 | grep "[^0-9]"
    if [ $TI2=`echo "\n ####" -o "$?" -eq "0" `]; then
        TI2=1.8;
    fi

    printf "T1a= "
    read T1a
    echo ""
    echo $T1a | grep "[^0-9]"
    if [ $T1a=`echo "\n ####" -o "$?" -eq "0" `]; then
        T1a=1.5;
    fi

    printf "T1= "
    read T1
    echo ""
    echo $T1 | grep "[^0-9]"
    if [ $T1=`echo "\n ####" -o "$?" -eq "0" `]; then
        T1=1.2;
    fi
fi

```

```

printf "deltat= "
read deltat
echo ""
echo $deltat | grep "[^0-9]"
if [ $deltat='echo "\n ###"' -o "$?" -eq "0" ]; then
    deltat=0.5;
fi

echo New values
echo lambda = $lambda ml/g
echo a = $alfa "%"
echo T11 = `echo "$T11*1000" | bc` ms
echo T12 = `echo "$T12*1000" | bc` ms
echo T1a = `echo "$T1a*1000" | bc` ms
echo T1 = `echo "$T1*1000" | bc` ms
echo deltat = `echo "$deltat*1000" | bc` ms

fi

printf "Choose file for time correction: "
read file
echo ""
printf "Slice Spacing= "
read slice_spacing
echo ""
fslmaths ${filename}_mean.nii.gz -mas brain_epi_mask.nii.gz ${filename}_mean_masked -odt float
fslsplit ${filename}_mean_masked.nii.gz mean_calc -z
fslsplit M0_image_GM.nii.gz M0_slice -z
k=`echo "(1/$T1a)-(1/$T1)" | bc -l` ;

T12_fixo=$T12 ;
t=0;
time=0;
while [ $t -lt $nslices ] ; do
    T12=`echo "$T12-($time/1000)" | bc -l`
    x=`echo "$t+1" | bc` ;
    time=`grep s_${x} $file | awk '{print $2}'`
    T12=`echo "$T12_fixo+($time/1000)" | bc -l`
    dt=`echo "$deltat*(1.88+($slice_spacing*$t))" | bc -l`
    q=`echo "e($k*$T12)*(e(-1*$k*$dt)-e(-1*$k*(T11+$dt)))/($k*$T11)" | bc -l`
    echo "$q" >> q_values.txt # save q values for a .txt file
    M0_provis=`fslstats M0_slice000${t}.nii.gz -M`
    fslmaths mean_calc000${t}.nii.gz -mul `echo "$lambda*e($T12/$T1a)" | bc -l` -div `echo
        "2*$M0_provis*$alfa*$T11*$q" | bc -l` -mul 6000 CBF_M0slice_${t} -odt float ;

    t=`echo "$t+1" | bc`

done

fslmerge -z mapa3_${filename}_M0slice CBF_M0slice*.nii.gz ;
fslmaths mapa3_${filename}_M0slice.nii.gz -thr 0 mapa3_${filename}_M0slice -odt float
rm CBF_M0slice* ;
rm mean_calc00* ;
rm M0_slice* ;
echo Perfusion Maps created

elif [ $Mode = "2" ]; then
...
elif [ $Mode = "1" ]; then
...
fi
done

rm ${filename}_mean.nii.gz
rm ${filename}_mean_masked.nii.gz

OUT;

```

### A.3. Functional images for all subjects

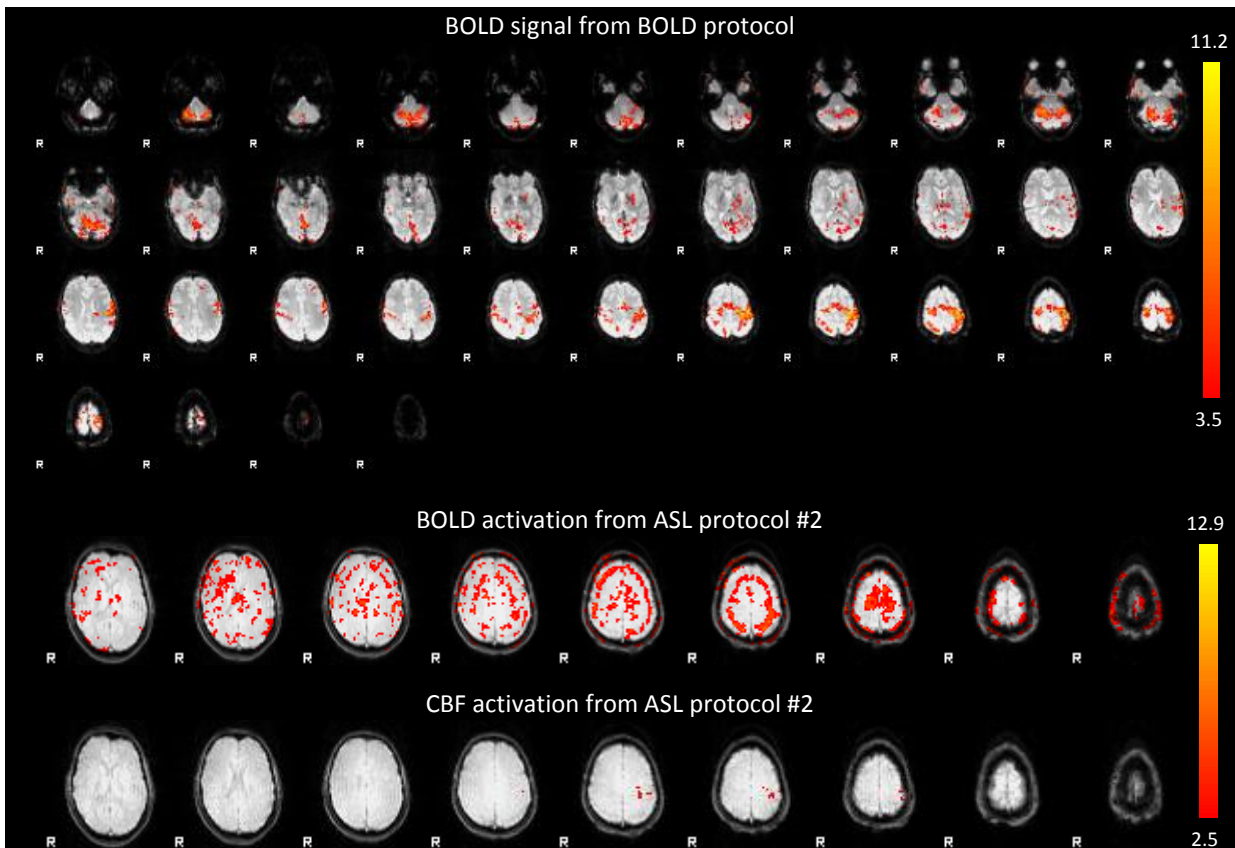


Figure A.1: Functional images from Subject 1.

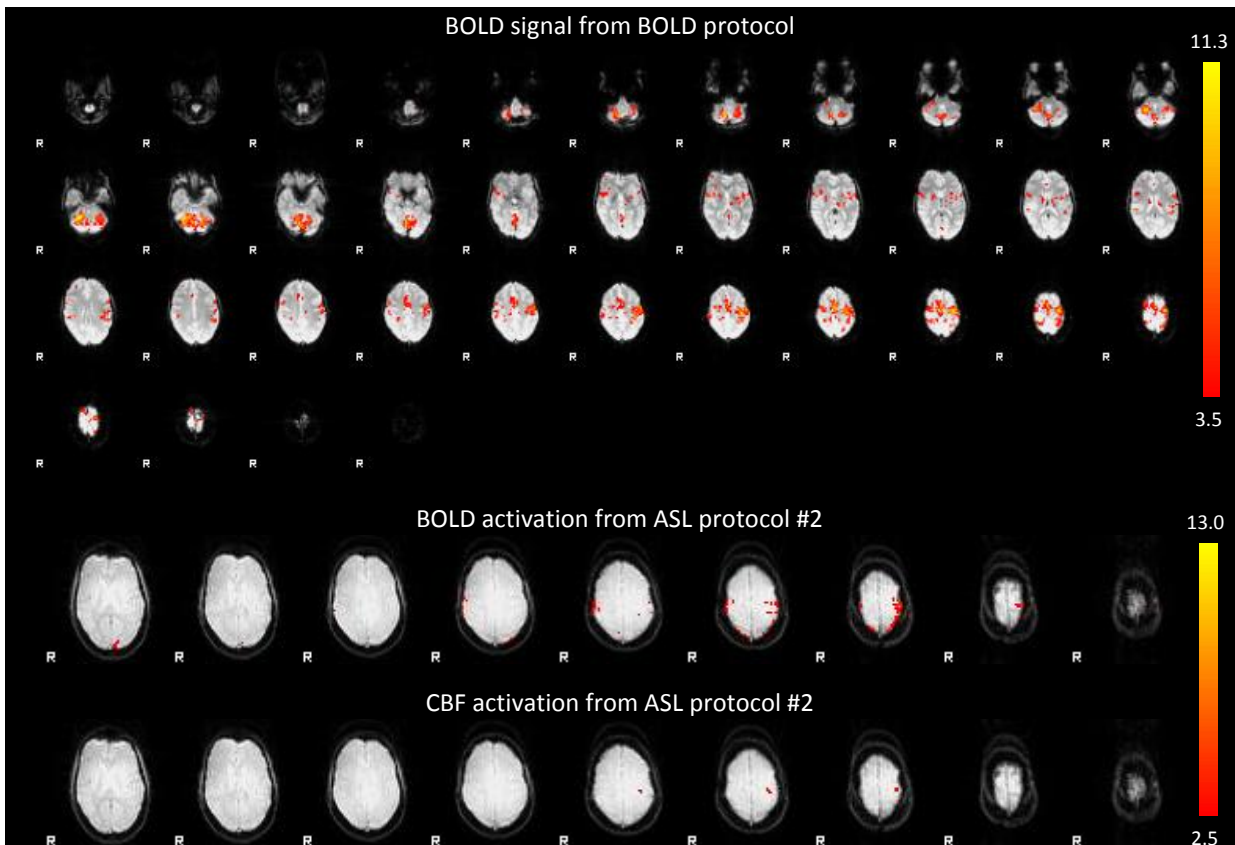


Figure A.2: Functional images from Subject 3.

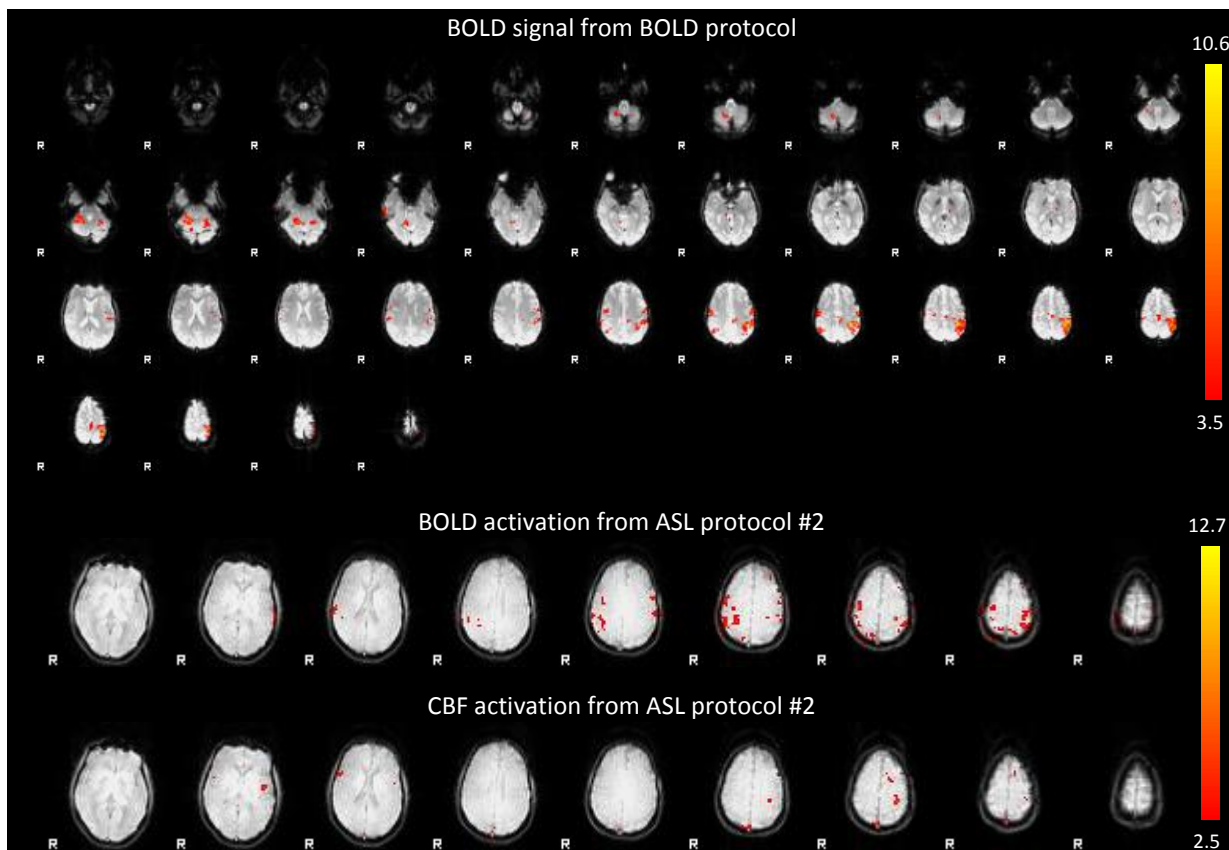


Figure A.3: Functional images from Subject 4.

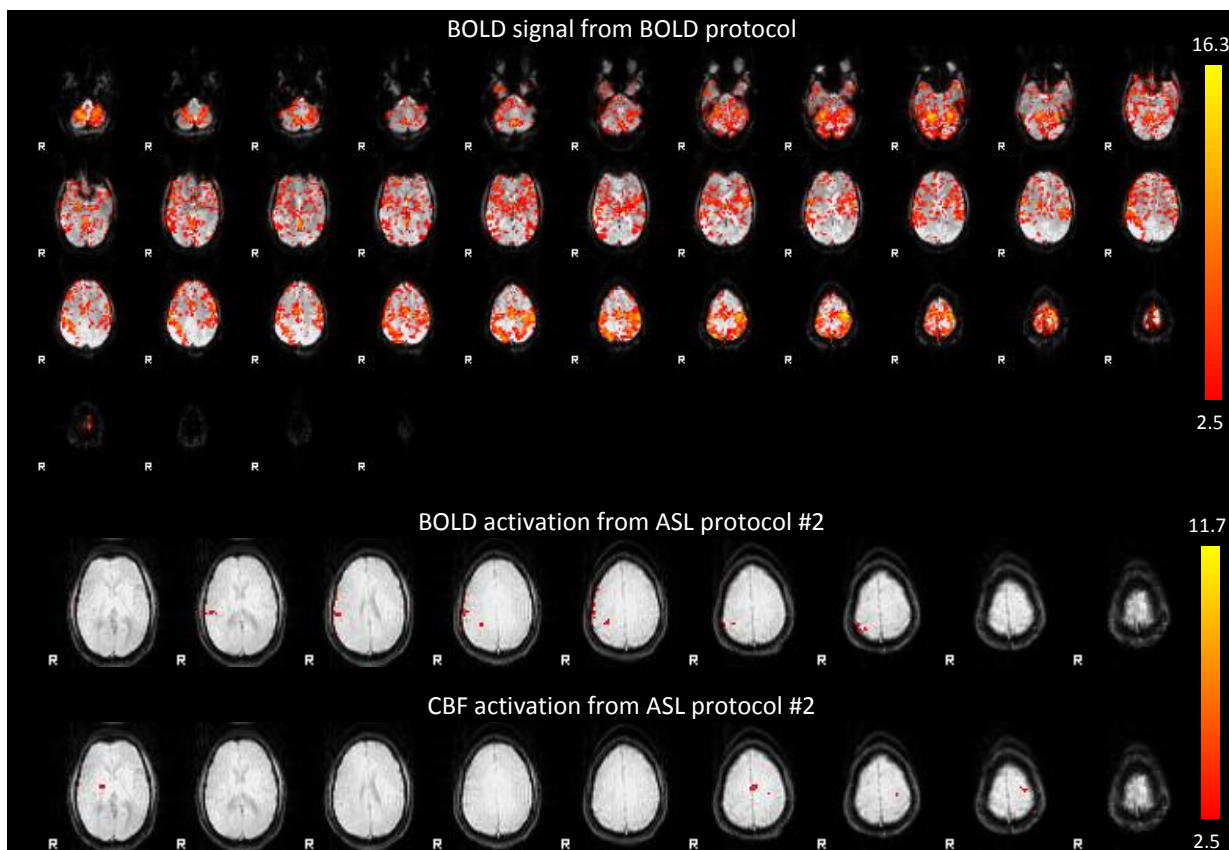


Figure A.4: Functional images from Subject 5.

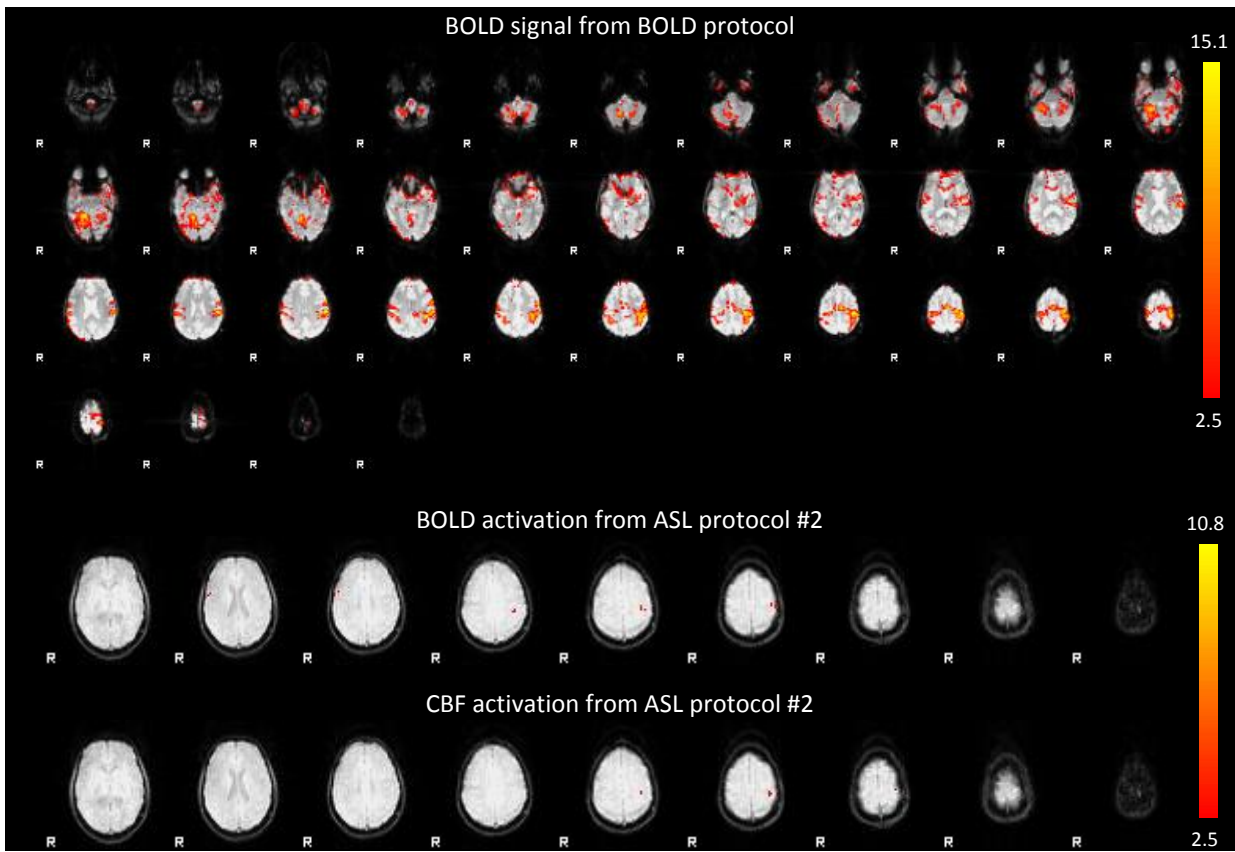


Figure A.5: Functional images from Subject 6.

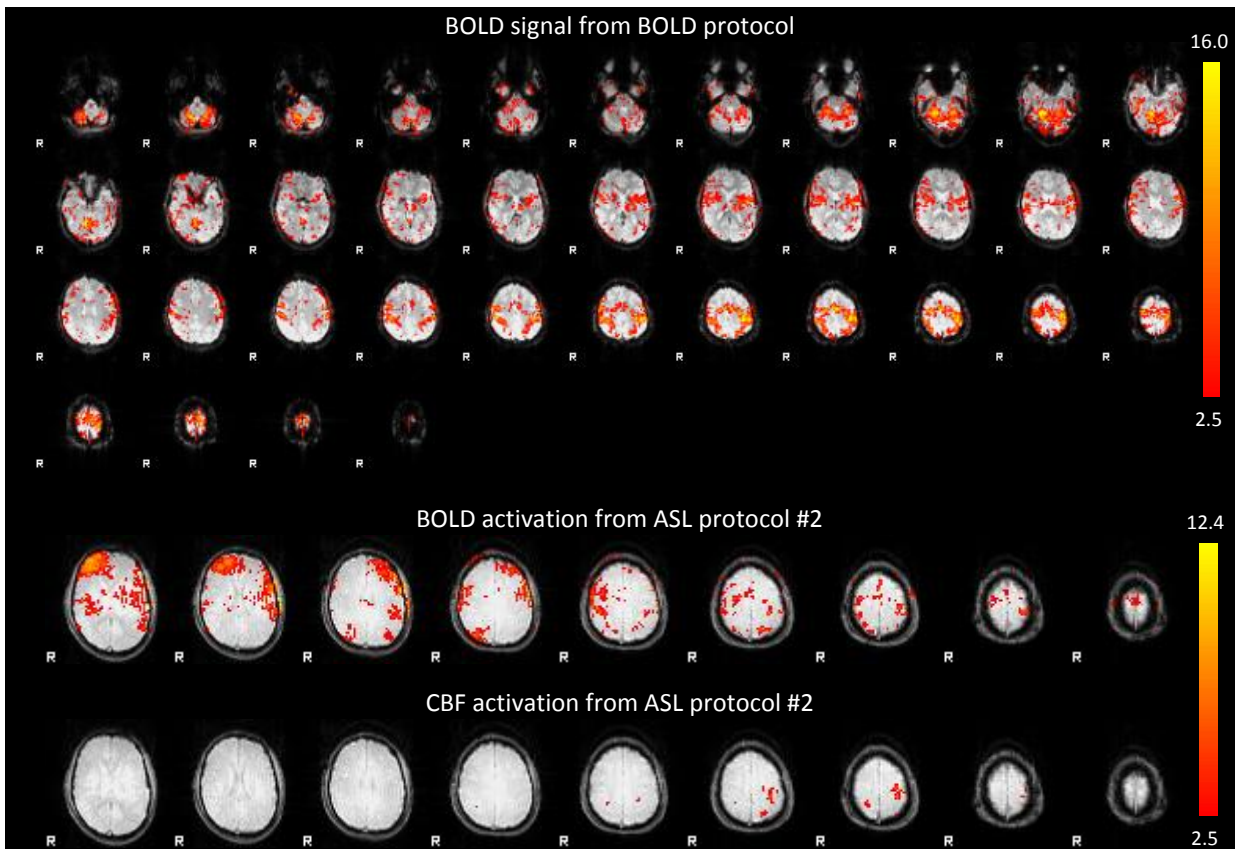


Figure A.6: Functional images from Subject 7.



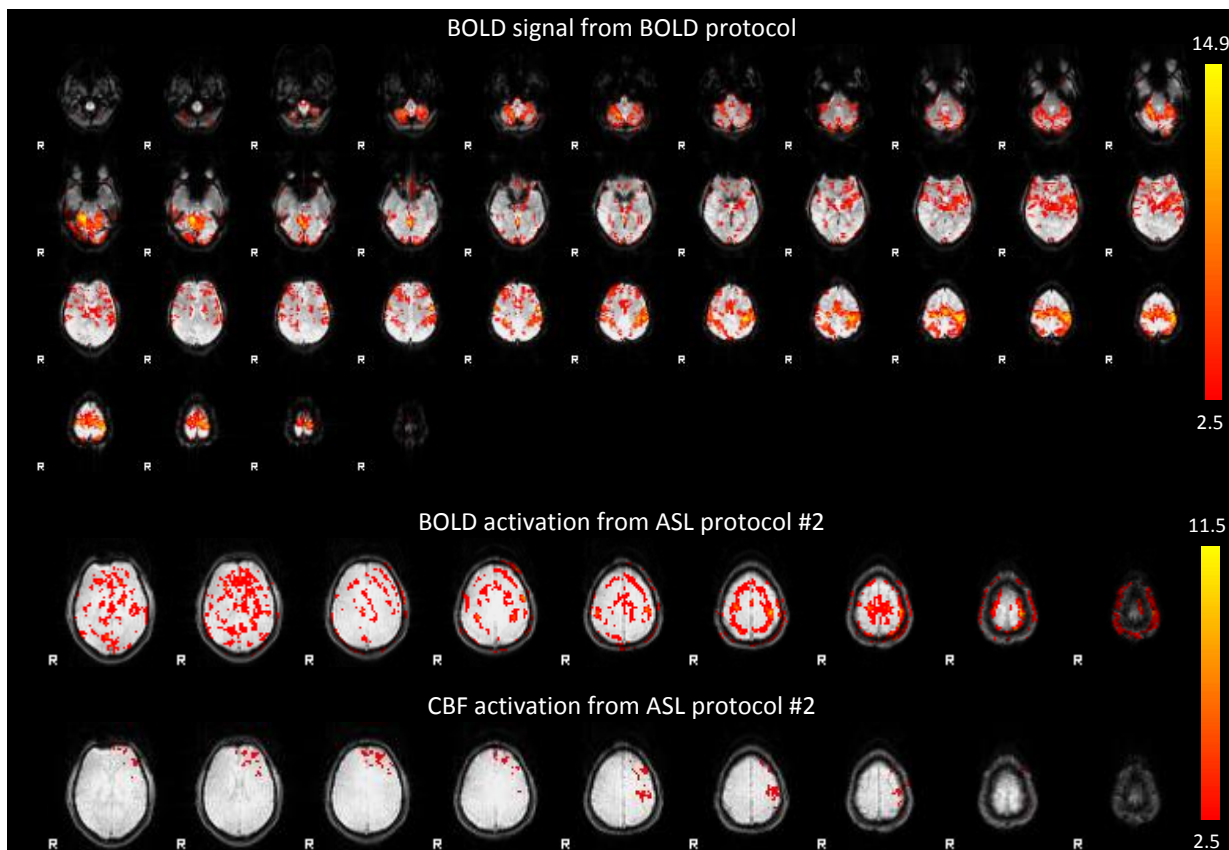


Figure A.7: Functional images from Subject 8.

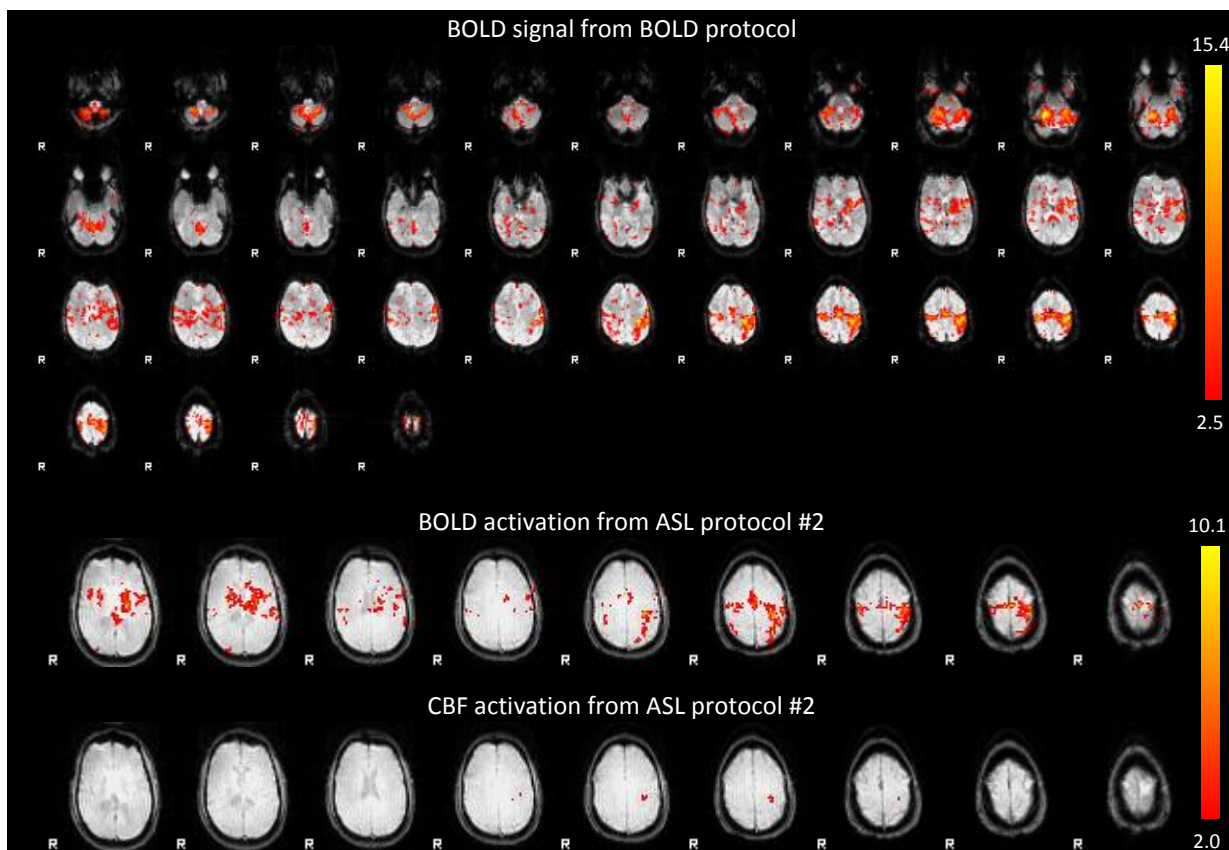


Figure A.8: Functional images from Subject 9.

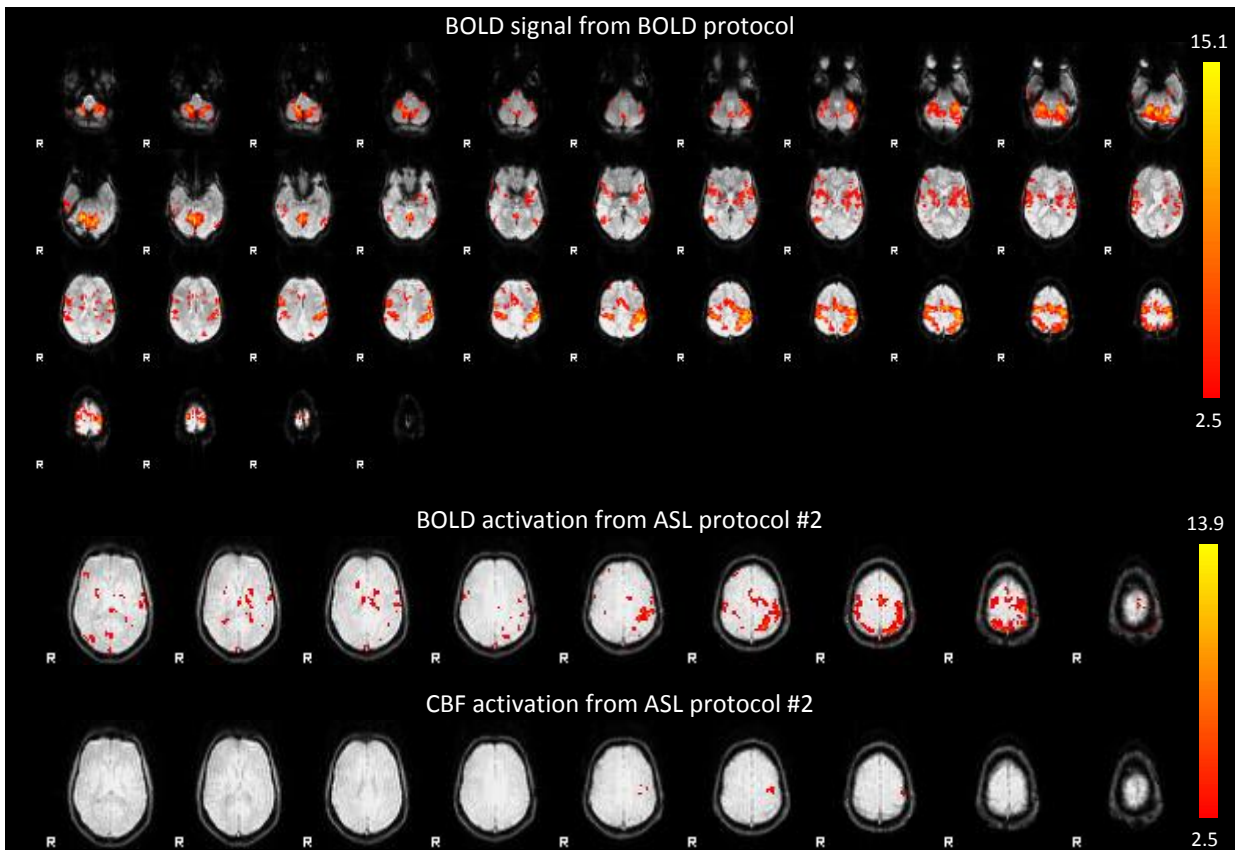


Figure A.9: Functional images from Subject 10.

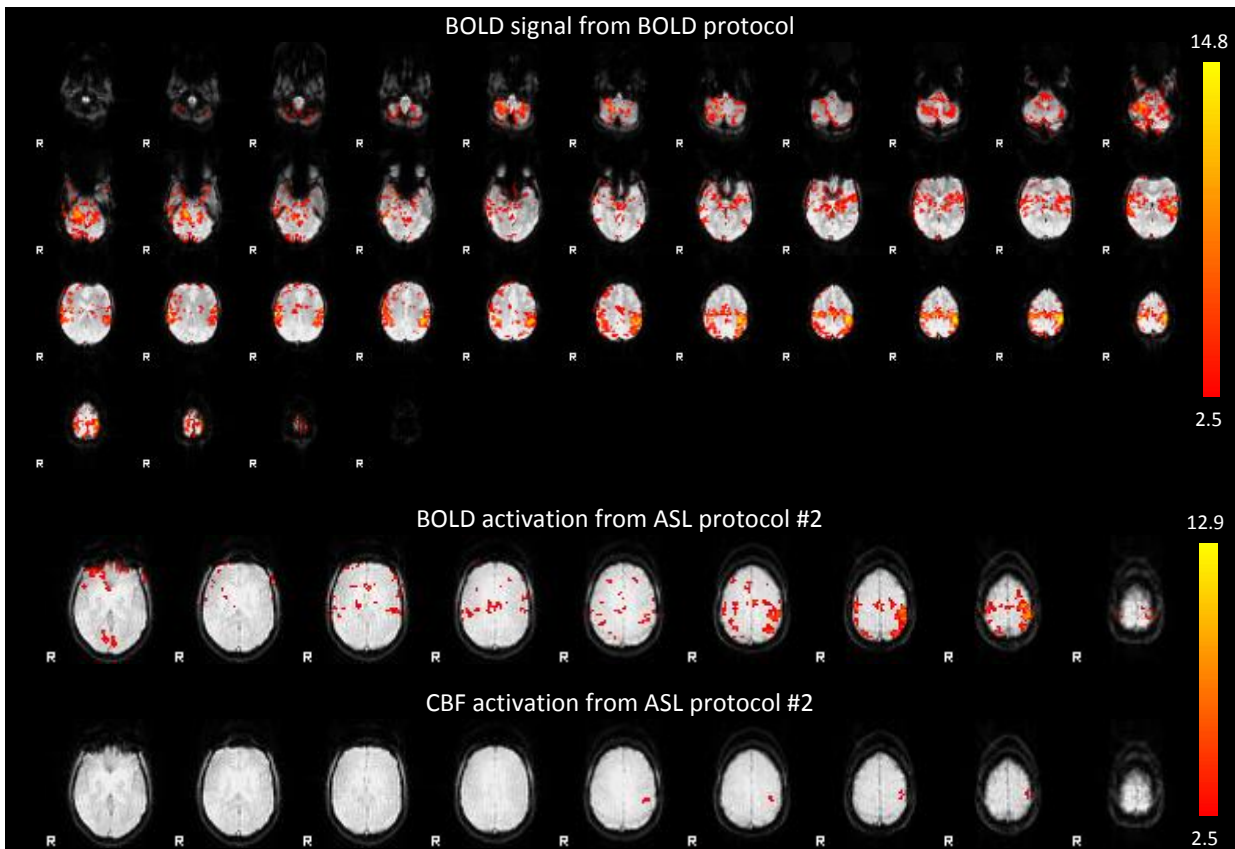


Figure A.10: Functional images from Subject 11.

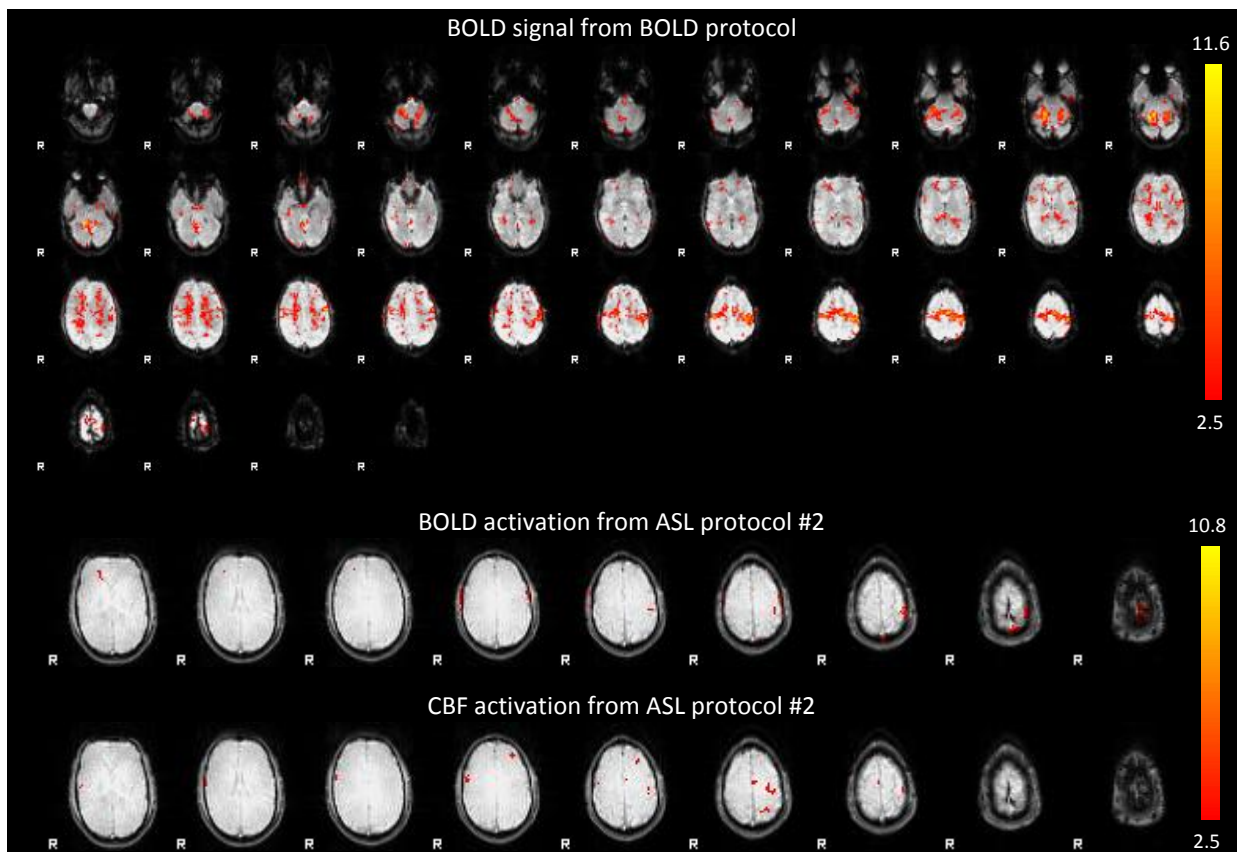


Figure A.11: Functional images from Subject 12.

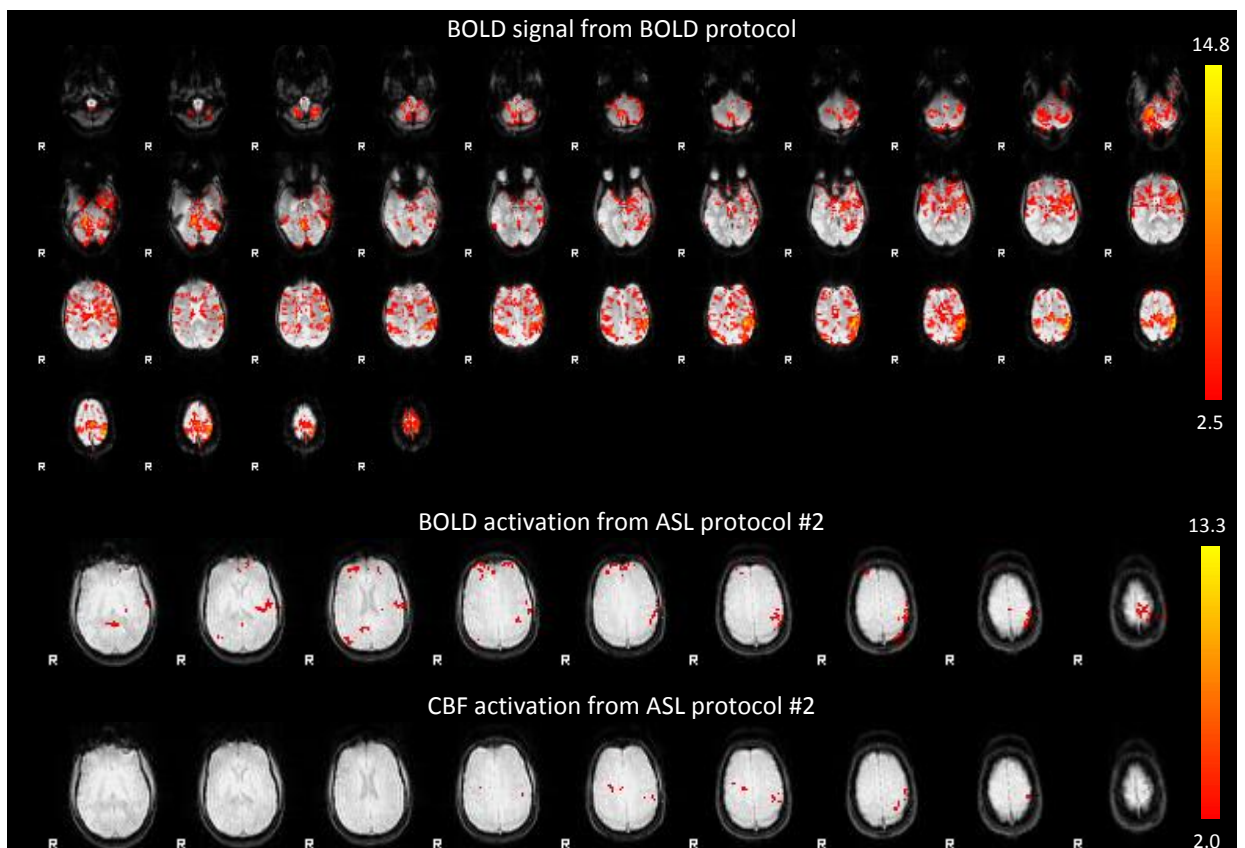


Figure A.12: Functional images from Subject 13.

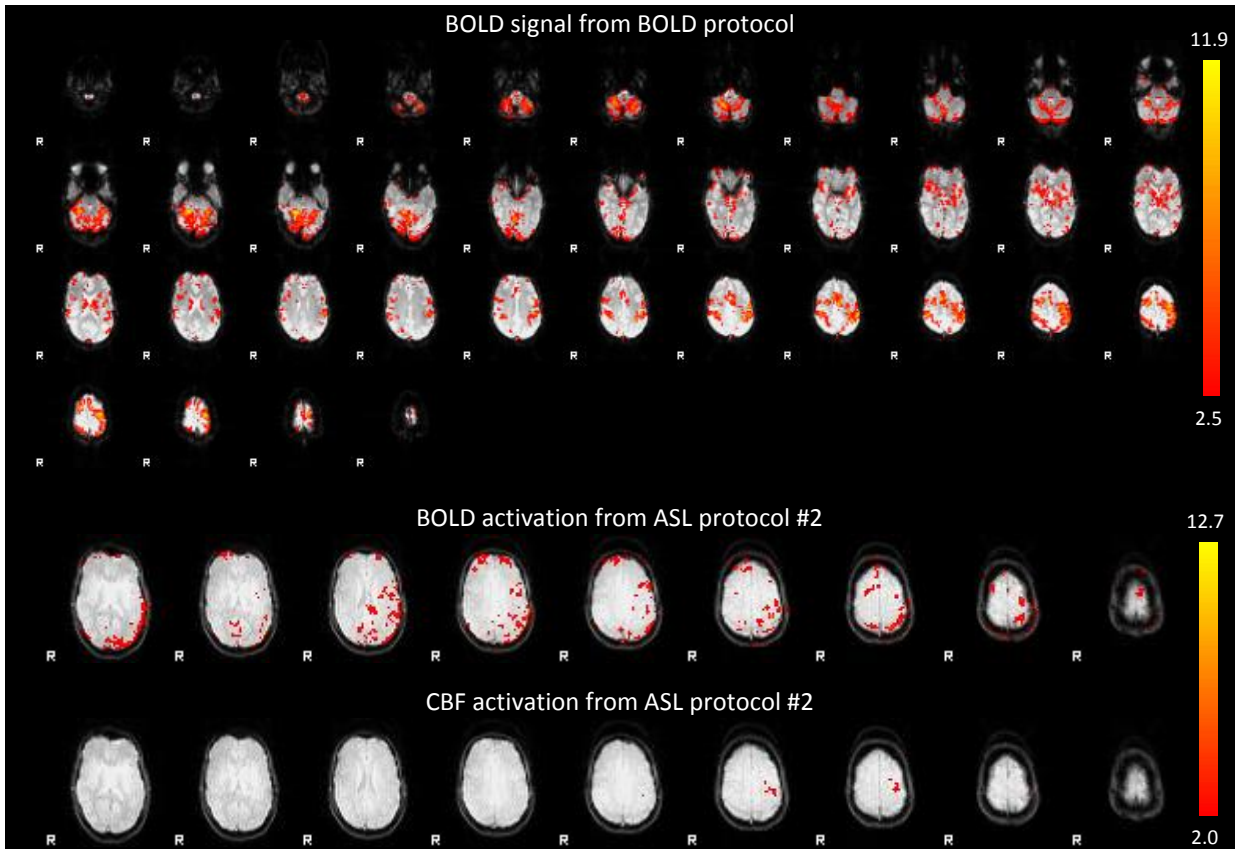


Figure A.13: Functional images from Subject 14.

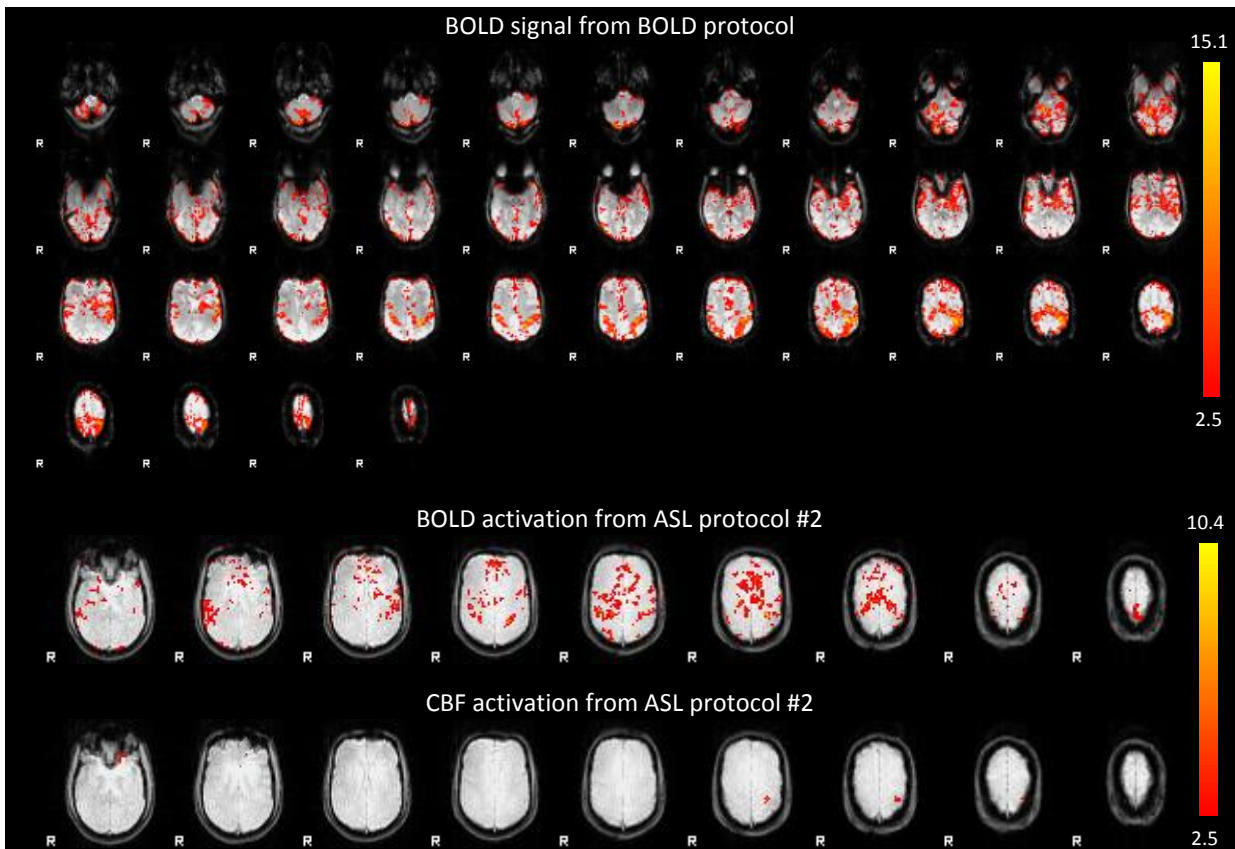


Figure A.14: Functional images from Subject 15.

## A.4. Distance to the hand motor cortex

Table A.1

Group mean Euclidean distance (in mm) from HMC points (M3, M2, M1, CM and CC) to CBF, BOLD<sub>ASL</sub> and BOLD activation COGs for all subjects

Subject	Mean Euclidean distance (mm) between <b>M3</b> and the activation COGs given by			Mean Euclidean distance (mm) between <b>M2</b> and the activation COGs given by			Mean Euclidean distance (mm) between <b>M1</b> and the activation COGs given by			Mean Euclidean distance (mm) between <b>CM</b> and the activation COGs given by			Mean Euclidean distance (mm) between <b>CC</b> and the activation COGs given by		
	CBF	BOLD <sub>ASL</sub>	BOLD	CBF	BOLD <sub>ASL</sub>	BOLD	CBF	BOLD <sub>ASL</sub>	BOLD	CBF	BOLD <sub>ASL</sub>	BOLD	CBF	BOLD <sub>ASL</sub>	BOLD
1	16.5	13.9	26.6	12.1	14.4	22.3	6.52	17.3	17.9	1.2	21.6	19.4	8.3	27.7	22.2
2	24.0	26.6	24.2	19.2	22.5	21.3	12.7	17.0	19.8	10.0	13.9	24.1	9.5	11.4	29.1
3	24.6	14.7	23.5	19.8	14.4	18.7	13.2	15.6	12.7	9.0	15.0	12.1	6.7	19.6	13.9
4	21.8	23.1	33.4	17.0	18.9	28.8	10.3	13.5	23.0	6.8	11.0	21.5	7.4	10.6	19.8
5	23.0	30.2	11.5	18.6	25.5	14.2	13.0	19.1	19.0	11.4	15.4	21.8	11.9	11.3	28.6
6	15.8	24.8	17.5	11.2	22.0	12.9	5.5	20.2	6.7	5.9	23.8	2.2	11.4	28.0	8.1
7	28.0	22.6	18.7	23.4	18.2	14.0	17.5	12.8	7.6	15.7	11.6	3.2	14.4	12.6	7.4
8	21.4	27.3	37.2	16.6	24.2	32.7	11.1	22.3	27.1	11.9	26.1	26.1	15.1	30.6	24.5
9	24.5	4.8	23.5	19.7	2.0	19.0	13.6	7.1	13.3	12.4	11.9	11.1	12.8	19.7	10.8
10	30.1	22.1	28.6	25.4	17.9	24.4	19.4	13.7	18.6	17.6	15.7	12.6	15.9	19.1	6.6
11	28.4	30.5	26.3	23.9	26.5	21.7	18.6	21.2	15.6	18.1	18.1	13.9	18.2	14.9	13.3
12	27.7	31.6	33.2	22.9	26.8	28.5	16.8	20.6	22.5	14.9	18.8	20.5	13.7	17.1	18.1
13	27.4	23.5	24.2	22.8	20.1	20.4	17.2	15.9	16.5	16.4	10.2	17.9	16.3	8.3	20.2
14	17.4	17.3	19.0	13.2	12.6	14.1	7.9	6.2	7.7	5.0	3.1	6.1	8.8	8.9	10.2
15	19.4	12.9	21.7	14.6	8.8	18.6	8.7	6.4	16.9	9.1	11.4	21.2	12.7	18.1	26.3
<b>Mean</b>	23.3	21.7	24.6	18.7	18.3	20.8	12.8	15.3	16.3	11.0	15.2	15.6	12.2	17.2	17.3
<b>Group</b>	± 2.2	± 3.8	± 3.4	± 2.3	± 3.6	± 3.0	± 2.2	± 2.8	± 3.0	± 2.5	± 3.0	± 3.1	± 1.9	± 3.7	± 4.0

Table A.2

Group mean Euclidean distance (in mm) from HMC points (CL, L1, L2, L3, C1 and C2) to CBF, BOLD<sub>ASL</sub> and BOLD activation COGs for all subjects

Subject	Mean Euclidean distance (mm) between <b>CL</b> and the activation COGs given by			Mean Euclidean distance (mm) between <b>L1</b> and the activation COGs given by			Mean Euclidean distance (mm) between <b>L2</b> and the activation COGs given by			Mean Euclidean distance (mm) between <b>L3</b> and the activation COGs given by			Mean Euclidean distance (mm) between <b>C1/C2</b> and the activation COGs given by		
	CBF	BOLD <sub>ASL</sub>	BOLD	CBF	BOLD <sub>ASL</sub>	BOLD	CBF	BOLD <sub>ASL</sub>	BOLD	CBF	BOLD <sub>ASL</sub>	BOLD	CBF	BOLD <sub>ASL</sub>	BOLD
1	13.6	28.3	19.0	17.0	27.4	16.2	22.1	33.0	20.7	27.7	39.6	25.2	7.2/7.6	25.4/22.2	19.4/16.3
2	5.6	6.8	26.4	6.5	7.7	22.7	11.9	10.9	28.0	17.9	17.0	33.3	6.4/3.9	9.5/8.5	26.0/21.8
3	5.0	26.7	11.4	8.7	30.6	10.5	13.0	35.4	15.8	18.3	40.9	21.1	4.2/4.6	20.2/21.2	11.1/8.4
4	8.0	7.7	12.1	10.7	8.6	6.5	15.7	13.3	7.4	21.2	19.6	11.7	4.7/3.8	8.1/5.9	17.4/15.2
5	7.8	3.2	34.6	6.8	4.4	37.2	12.5	6.1	42.8	19.1	11.6	48.8	8.8/5.3	9.6/9.6	28.2/27.8
6	12.5	23.9	12.5	13.6	19.2	15.7	19.5	24.2	20.9	25.8	29.9	26.4	8.6/5.2	24.6/20.0	6.5/6.6
7	7.3	8.7	11.1	1.6	7.2	14.3	7.8	13.0	19.3	14.2	19.6	24.9	11.6/9.0	9.5/5.7	5.5/5.4
8	12.8	27.6	16.7	11.3	23.9	11.0	17.1	28.7	10.4	22.9	33.4	12.6	12.0/8.4	27.6/23.7	22.1/19.8
9	8.0	23.4	6.7	5.7	24.7	6.6	11.7	30.6	12.0	17.8	37.0	18.5	9.7/6.3	18.0/16.1	7.8/4.9
10	8.4	15.1	12.4	2.7	11.3	18.3	6.8	17.2	20.2	12.7	23.4	23.3	13.4/11.1	15.7/11.2	9.3/13.6
11	11.5	9.0	7.0	5.5	8.5	3.3	10.3	9.3	9.5	16.2	14.7	15.8	15.2/11.8	13.3/12.5	10.3/7.4
12	6.9	10.6	10.1	2.7	7.2	4.8	8.4	9.4	5.1	14.5	13.4	10.2	10.9/8.5	14.8/13.1	15.9/14.0
13	9.8	16.6	15.3	4.3	22.2	10.8	9.8	25.3	16.0	16.0	29.5	22.3	13.3/10.0	10.8/14.6	17.0/12.6
14	11.3	12.6	12.0	13.8	15.3	13.8	19.0	20.6	19.2	25.2	26.2	24.8	6.6/5.1	7.0/6.4	7.9/6.3
15	11.0	18.2	23.6	10.3	17.4	19.9	16.5	23.7	25.6	22.8	30.1	31.3	9.4/5.1	15.2/11.2	23.1/18.7
<b>Mean</b>	9.3	15.9	15.4	8.1	15.7	14.1	13.5	20.0	18.2	19.5	25.7	23.3	9.5±1.9/	15.3±3.4/	15.2±3.8/
<b>Group</b>	± 1.4	± 4.3	± 3.9	± 2.4	± 4.4	± 4.3	± 2.2	± 4.8	± 4.7	± 2.3	± 4.9	± 5.0	7.1±1.1	13.5±3.1	13.3±3.5

## **Appendix B**

### **Publications: Oral communications**

#### **Published work:**

M. PIMENTEL, P. VILELA, I. SOUSA, P. FIGUEIREDO, Avaliação da activação cerebral na função motora em ressonância magnética pelas técnicas *Blood Oxygen Level Dependent* e de *Arterial Spin Labeling*, *Acta Médica Portuguesa* 2009; 22 (2):139.

P. VILELA, M. PIMENTEL, I. SOUSA, P. FIGUEIREDO, Arterial Spin Labeling for functional MRI using motor task, *Neuroradiology* (2009); 51 (Suppl 1):S25-S97.

#### **Accepted work:**

Work entitled "Ressonância Magnética funcional: avaliação da área motora por variação do fluxo sanguíneo cerebral pela técnica ASL", submitted for the National Neurology Congress 2009.

Authors: P. Vilela, M. PIMENTEL, I. Sousa, P. Figueiredo

# AVALIAÇÃO DA ACTIVAÇÃO CEREBRAL NA FUNÇÃO MOTORA

## Em Ressonância Magnética pelas técnicas de *Blood Oxygen Level Dependent* e de *Arterial Spin Labeling*

### EVALUATION OF THE MOTOR BRAIN ACTIVATION BY MAGNETIC RESONANCE IMAGING USING BLOOD OXYGEN LEVEL DEPENDENT AND ARTERIAL SPIN-LABELING TECHNIQUES

Marco PIMENTEL, Pedro VILELA, Inês SOUSA, Patrícia FIGUEIREDO  
M.P.: Faculdade de Ciências e Tecnologia. Universidade Nova de Lisboa. Lisboa  
P.V.: Departamento de Imagiologia. Neurorradiologia. Hospital da Luz. Lisboa  
I.S., P.F.: Instituto Superior Técnico. Universidade Técnica de Lisboa. Lisboa

**Introdução:** A técnica BOLD (blood oxygen level dependent) é a mais usada e universalmente aceite nos estudos de ressonância magnética funcional. A técnica ASL (arterial spin labeling) é uma técnica não invasiva, de estudo da perfusão cerebral, que usa as moléculas de água como *tracers* endógeno de perfusão permitindo avaliar o fluxo sanguíneo cerebral (CBF).

**Objectivos:** Avaliação comparativa da activação cerebral na função motora pelas técnicas BOLD e ASL. São apresentados os resultados iniciais desta análise comparativa.

**Metodologia:** Num equipamento 3 Tesla (Siemens, Verio) foram avaliados 15 voluntários por RM funcional, em tarefas de motoras da mão direita, usando as sequências BOLD (EPI) e ASL em repouso e em activação. O pós-processamento foi efectuado no software Neuro3D (Siemens). Foram analisadas a capacidade da técnica ASL em detectar alterações de fluxo entre o estado de repouso e da tarefa motora e a correlação topográfica entre as áreas de activação por ASL e BOLD.

**Resultados:** Os resultados iniciais deste estudo comparativo demonstraram ser possível detectar as áreas de activação com a técnica ASL, e que estas áreas estavam em concordância topográfica com as obtidas pelo método BOLD.

**Conclusão:** As conclusões iniciais sugerem que a técnica ASL pode ser usada no contexto da RM funcional; existindo algumas especificidades relativamente aos protocolos de aquisição e de pós-processamento que são discutidas.



# ARTERIAL SPIN LABELLING FOR FUNCTIONAL MRI USING MOTOR TASK

P. VILELA<sup>1</sup>, M. PIMENTEL<sup>2</sup>, I. SOUSA<sup>3</sup>, P. FIGUEIREDO<sup>3</sup>

<sup>1</sup>HOSPITAL DA LUZ, LISBON, PORTUGAL,

<sup>2</sup>FACULDADE DE CIÊNCIAS E TECNOLOGIA UNL, LISBON, PORTUGAL,

<sup>3</sup>INSTITUTO SUPERIOR TÉCNICO UTL, LISBON, PORTUGAL

**Background and Purpose:** The new clinically available arterial spin labelling (ASL) sequences present some advantages relatively to the blood oxygenation level dependent (BOLD) method for functional brain studies, namely the fact of being potentially quantitative and more reproducible. The aim of our study was to compare two functional clinical protocols, using BOLD and ASL, in terms of the activation detected in a pre-determined region of interest (ROI).

**Materials and Methods:** Both ASL and BOLD imaging were performed on a Siemens Verio 3.0 T scanner. Eight healthy adult volunteers performed a motor finger tapping task. The BOLD protocol used a block design consisting of 4 cycles alternating 30 seconds of task with 30 seconds of rest. The ASL protocol consisted on the acquisition of one image during rest and another during the task. Post-processing was performed using *Siemens Syngo MR* and an anatomical ROI was identified by a neuro-radiologist. For the BOLD protocol, the General Linear Model (GLM) was used to produce t-statistics maps of activation. For the ASL protocol, the rest and activation perfusion images were subtracted to produce an activation map. The scales of the BOLD and ASL activation maps were both normalized to 1 and evaluated in the pre-defined ROI.

**Results:** The mean (and standard error) activation observed for the BOLD and ASL protocols in the ROI was, respectively: 0.956 (0.035) and 0.943 (0.044). No significant differences were observed between the between the activation information provided by each protocol.

**Conclusion:** Our data suggest that the functional imaging protocol using ASL produces comparable results to a conventional BOLD protocol.

